GRAIN REFINEMENT OF CAST NIOBIUM VIA EQUAL CHANNEL ANGULAR EXTRUSION/ANNEALING

A Thesis

by

DON O. BRYANT

Submitted to the Office of Graduate Studies of
Texas A&M University
in partial fulfillment of the requirements for the degree of

MASTER OF SCIENCE

December 2005

Major Subject: Mechanical Engineering

GRAIN REFINEMENT OF CAST NIOBIUM VIA EQUAL CHANNEL ANGULAR EXTRUSION/ANNEALING

A Thesis

by

DON O. BRYANT

Submitted to the Office of Graduate Studies of
Texas A&M University
in partial fulfillment of the requirements for the degree of

MASTER OF SCIENCE

Approved by:

Chair of Committee,	Karl T. Hartwig, Jr.
Committee Members,	Richard B. Griffin
	Donald G. Naugle
Head of Department,	Dennis L. O'Neal

December 2005

Major Subject: Mechanical Engineering

ABSTRACT

Grain Refinement of Cast Niobium via Equal Channel Angular Extrusion/Annealing.

(December 2005)

Don O. Bryant, B.S., The University of Texas at San Antonio

Chair of Advisory Committee: Dr. Karl T. Hartwig, Jr.

This research investigated the effectiveness of equal channel angular extrusion (ECAE) and annealing to improve the grain morphology and mechanical properties of electron-beam remelted pure niobium. Extrusions were performed at room temperature with a 90^{o} die. Routes 1A, 2C, 4E and 8E were investigated with duplicate billets undergoing routes 1A, 2C and 4E to determine reproducibility.

Niobium proved to be very workable during the ECAE process. Hardness increased most dramatically after the first pass and leveled off thereafter.

Recrystallization temperatures for the Reference Metals material ranged from a low of 800^{o} C for routes 2C, 4E and 8E to a high of 1000^{o} C for route 1A. For the Wah Chang material, the recrystallization temperatures ranged from a low of 800^{o} C for the 4E ECAE processed material to a high of 950^{o} C for the as-received material.

The initial grain size and orientation have been hypothesized to be influential on recrystallized grain morphology for ECAE/annealing processed niobium. Smaller initial grains produce a smaller and more homogeneous recrystallized grain microstructure. The average grain diameters for the recrystallized 4E ECAE processed Wah Chang material are 13 ± 6.3 μm for the 1000^{o} C annealed state (no banding) and are 21 ± 9.5 μm for the 1100^{o} C annealed state (no banding). Reference Metals material that underwent route 4E and annealed at 1000^{o} C resulted in an average grain diameter of 28 μm for billet 2 (banding) and an average grain diameter of 32 μm for billet 19 (slight banding). Reference Metals material that underwent route 8E (no banding) annealed at 1000^{o} C resulted in an average grain diameter of 36 μm. Reference Metals material that underwent route 4E samples annealed at 1100^{o} C resulted in an average grain diameter of 26 μm for billet 2 (banding) and an average grain diameter of 43 μm for billet 19 (slight banding). Route 8E (significant banding) annealed at 1100^{o} C resulted in an average grain diameter of 29 μm.

Strain failure decreases from the as-cast material to the worked/recrystallized material while the 0.2% yield stress and ultimate tensile strength increase from the as-cast material to the worked/recrystallized material.

Long sub-grains are created in the as-worked material after one and two passes and become more broken up after four passes. Sub-grain boundary angles increase with increasing strain.

To produce a fine and homogeneous microstructure from large grained niobium, intermediate annealing should be employed.

DEDICATION

This thesis is dedicated to my parents, committee chairman and committee members.

ACKNOWLEDGEMENTS

I would like to thank the U.S. Department of Energy, the State of Texas and personnel at the Microscopy and Imaging Center at Texas A&M University.

TABLE OF CONTENTS

CHAPTER Page

CHAPTER Page

LIST OF FIGURES

FIGURE Page

FIGURE Page

FIGURE Page

FIGURE Page

FIGURE Page

FIGURE Page

LIST OF TABLES

TABLE Page

CHAPTER I

INTRODUCTION

A. Motivation

Type II superconductors typically come in the form of composite wires consisting of extremely fine superconducting filaments embedded in a copper matrix. Most are used in high field magnetic applications and are wound into magnets of various shapes and sizes to produce various field strengths. Some of the more common applications for type II superconducting magnets include magnetic resonance imaging (MRI), particle acceleration and fusion research. Essential to all of these applications is the production of large and uniform magnetic fields. Magnetic strength and uniformity can be improved by making the windings as uniform and compact as possible. Ideally, the superconducting cable should consist of continuous, thin and symmetric filaments arranged in a symmetric pattern. Each filament should have axial symmetry and not have contact with other filaments. In reality, various defects exist in practical composite superconductors and are what motivates this research. The specific goals of this research are to refine and homogenize the microstructure of pure niobium thereby increasing the isotropic characteristics of pure niobium to flow uniformly during the manufacturing of type II superconducting wires.

Past experiences have shown that the cause of the previously mentioned defects can originate in the superconducting wires during the manufacturing stage. Niobium is a common metal used in type II superconductors. It is a relatively soft metal but has a high melting point. Because it is soft, niobium is susceptible to breakage and to deform in a nonuniform manner. This susceptibility can be increased when niobium is adjacent to other metals during the superconducting wire manufacturing process. This is because of differences in mechanical characteristics including ductility, elastic modulus, plastic modulus etc. between the filament and matrix phases. This is of considerable importance during the manufacturing stage of niobium based superconductors because numerous drawings are required to produce the extremely fine filaments. Niobium rods undergo area reduction by large tensile strains until the filaments are drawn down to strands with diameters in the micron range. This is where strengthening and uniform deformation is essential. Once the Nb reaches the desired filament diameter, the wire is given a heat treatment which converts the Nb to Nb_3Sn via diffusion of Sn.

From the operational side, type II superconductors operate at extremely low temperatures, $T_{operating} < 20^{o}$ K and often operate at extremely high magnetic fields, B > 10 T. Under such conditions, the filaments are subjected to large stresses due to electromagnetic forces and thermal stresses. Furthermore, differences in

---

This thesis follows the style and format of Materials Science and Engineering A.

thermal expansion coefficients among the various metals produce stresses at metallic interfaces.

From considering the manufacturing and operational aspects of type II superconductors one can conclude that it is desirable to improve the mechanical characteristics of pure niobium by improving the isotropic deformation characteristics and by increasing its ductility. This can be done by reducing and homogenizing the microstructure of pure niobium. A common method of reducing the microstructure in metals is with thermo-mechanical processes such as Equal Channel Angular Extrusion/Annealing. Thermo-mechanical processes are processes that breakup crystals and then reforms the crystals to produce new and more numerous crystals. Equal Channel Angular Extrusion (ECAE) is a mechanical process that forces a piece of metal through a die thereby putting the work piece through severe shear plastic deformation. This research seeks to find the most effective ECAE/Annealing process which results in minimizing the grain size and producing a more homogenized microstructure in pure bulk niobium.

B. Materials and Methods

One of the essential metals used in type II superconductors is niobium. Bulk niobium typically comes in ingots greater than 23.5 cm diameter and is highly textured. Grains can be as long as 15 cm and are irregularly shaped polyhedrons. In contrast, type II superconducting cables contain niobium filaments with diameters and grain diameters in the micron range. It is therefore desirable to refine the ingot grains by thermo-mechanical processing prior to the manufacturing stage. Typical refining methods include plastic deformation processing techniques such as hot rolling, cold rolling, forging and drawing, all followed by annealing. Unfortunately, such techniques tend to alter the shape of the material and produce nonuniform microstructures. Another type of grain refinement method is the introduction of solute elements which may produce more grain nucleation sites. The drawback of this method is that impurities can disrupt the superconducting state. Because the previously mentioned grain refinement processes have undesirable results, this research utilizes equal channel angular extrusion (ECAE)/annealing to manipulate the microstructure of large grained niobium in an attempt to refine and homogenize the polycrystal morphology.

The research presented here investigates the strength and microstructure evolution by performing mechanical tests, optical microscopy and transmission electron microscopy. Tests included: hardness tests (Brinell, Rockwell and Vickers), tensile tests, optical microscopy (OM) and transmission electron microscopy (TEM). All of the previously mentioned tests were investigated with the impact of strain, route, annealing temperature, initial grain size and reproducibility in mind. Microstructural features such as grains and sub-grains were measured for size and shape keeping morphology in mind. Hardness tests were used to investigate the strain hardening and recrystallization characteristics. Tensile tests involved determining such variables such as 0.2% yield stress [MPa], ultimate tensile strength [MPa], % elongation [$\delta L/L_o$] and toughness [MJoule/m^3].

C. Strengthening by Grain Refinement

Because polycrystalline metals consist of a conglomeration of single crystals, deformation must be considered at the single crystal level. Plastic deformation of a single crystal occurs by shear deformation. Because shearing processes for crystals tend to occur on preferred planes, single crystals deform both elastically and plastically in an anisotropic manner. There are general rules that attempt to identify these "favorable" planes by referring to slip directions and slip planes but exceptions do exist. To further complicate matters, the shear stress required to cause shear deformation is reduced by defects called dislocations. Still further, dislocations are born and interact with each other during plastic deformation. Dislocations are areas in a crystal where planes of atoms are absent, thereby producing internal stresses along the dislocation. The length of these dislocations can span hundreds of thousands of atoms and have irregular paths. During plastic deformation, dislocations move in complicated directions and cross one another's paths. This interaction can result in an increase in the density of the dislocations and produce what are called jog defects. Although the interaction of jogs and dislocations is complicated, in general, jogs hinder the movement of dislocations. By hindering the dislocations in a crystal, the material is strengthened. Macroscopically, this can be proven by a hardness test because hardness is an increasing function of strain. This increase in hardness is called strain hardening.

Furthermore and more important to this research, grain boundaries serve as obstacles to dislocation movement. Grain boundaries can be visualized as surfaces between grains where there is a discontinuity in crystal orientation. By decreasing the size of a grain, dislocations are unable to travel as far before interacting with other dislocations, thereby increasing material flow stress in a polycrystal. This relationship between yield stress, σ_y , and grain size d, is exemplified by the Hall-Petch equation, which is:

$$\sigma_y = \sigma_o + k_y d^{-\frac{1}{2}} \qquad (1)$$

σ_0 and k_y are material constants.

D. Strengthening by Equiaxed Grains

Because superconducting filaments are extremely thin, it is important that the filaments have small grains with a uniform microstructure. Grain size, microstructural homogeneity and texture determine whether or not a polycrystalline metal should be considered either isotropic or anisotropic. If the grains are large relative to the work piece, then it cannot be considered isotropic. This is because individual crystals are anisotropic. This is an important consideration in the manufacturing stage of superconducting wires because grain

diameters are on the order of the filament diameters. This can cause irregular plastic deformation which can result in a defect called sausaging. Sausaging is non uniform deformation which results in thin areas thereby creating a weak point in the filament. Therefore, it is advantageous to produce a more uniform and fine grain structure in niobium prior to the manufacturing process.

E. Equal Channel Angular Extrusion

Equal Channel Angular Extrusion (ECAE) is an extrusion process that forces a billet or work piece through a die that has both a constant cross sectional area and geometric shape. Extrusion temperatures can also vary. For this study, the channel has a square cross-section and the die angle is 90^o with all extrusions performed at room temperature. Shear strain occurs at the intersecting transverse planes of the entering and exiting channels. Ideally, this strain is uniform across the intersecting plane. Each pass through the die produces an idealized strain of 1.15. Therefore, the overall strain can be represented by $\gamma = 1.15N$ where N is the number of passes. It should be noted that this formula does not consider path dependence and path dependence is important when dealing with anisotropic materials. One advantage of ECAE is that it is possible to control microstructural changes to some extent. This is done by repeating the passes through the die and making various rotations of the billet. Typical microscopic changes include elongating of grains, fragmenting grains, creating vacancies, dislocations and twins. This research will utilize four routes: 1A, 2C, 4E and 8E. Route 1A is one pass through the die. Route 2C is one pass through the die followed by a 180^o rotation of the billet then followed by another pass through the die. Route 4E can be described as route C followed by a 90^o rotation and route C again. Route 8E is the following route: C/90^o, rotation/C/90^o, rotation/C/90^o, rotation/C/90^o. The significant difference between the various routes is the introduction of different shear planes and shear directions.

F. Annealing

Annealing is the process of heating a cold worked metal with the purpose of decreasing the internal stress and changing grain shape. This results in altering mechanical properties such as hardness, yield stress, ultimate strength, and ductility by reducing the internal stresses and allowing development of new grains. At the microscopic level, annealing can be divided into three major stages: recovery, recrystallization and grain growth.

The recovery stage is associated with annihilation of point defects and changes in the arrangement/distribution and local density of dislocations. The dense concentration of dislocations in cold worked metals move at elevated temperatures and interact with each other. Typically, vacancies are annihilated and dislocations become reorganized to form sub-boundaries but do not necessarily decrease

substantially in numbers. This stage can result in the worked material becoming slightly harder.

The recrystallization process is the stage of annealing where the most notable changes in mechanical properties occur. Recrystallization is the process where stress free grains are produced. The origins of these stress free grains are called nucleation sites which are formed in high density energy dislocation regions or in grain boundary regions. Significant to this research is the rate of recrystallization. This rate is dependent primarily on three factors: the amount of cold work, the annealing temperature and purity of the metal.

Grain growth is the final stage of annealing and is associated with stress free grains that either grow or are consumed. Larger grains tend to devour smaller grains. Atoms are able to cross grain boundaries via diffusion during this process. Visible observations show that the grain boundaries associated with this stage become straight as the crystal arrangement seeks to minimize its total energy by minimizing the grain boundary area.

CHAPTER II

LITERATURE REVIEW

A. Niobium Properties and Applications

Niobium is a shiny-white, soft refractory metal that is used in a wide variety of products. It is used in both pure and compound form. It looks similar to steel, but when polished resembles platinum. Some of the more amiable characteristics include a high melting point, corrosion resistance, excellent formability, a low thermal neutron capture cross section and it is a good superconductor when alloyed with titanium (Ti) or tin (Sn). The least amiable aspect of this metal is its tendency to gall during deformation or when being cut.

The majority of niobium is used in the steel industry, which is responsible for 90% of its use. Of the 90%, high-strength low-allow (HSLA) steel accounts for approximately 75% of its use, while the remaining 15% is used in stainless steels and heat resistant steels[1]. In the HSLA industry, niobium is added to steels to improve the yield strength and other mechanical properties. Niobium can increase the strength of steels by acting as a grain refiner (by increasing the number of nucleation sites) and by precipitation hardening. These steels are used where strength and corrosion resistance properties are essential such as in large diameter oil and gas pipelines, drilling platforms and in various other structural components. In the stainless steel and heat resistant steel industries, niobium is added to reduce corrosion at high temperatures. These applications include exhaust systems for automobiles, petroleum-processing plants, heat exchangers in corrosive environments and acid pressure vessels.

In the superalloy industry, ferroniobium and high purity niobium pentoxide are used in aircraft turbines and other engine parts. As much as 6% niobium is added to these superalloys in order to improve the heat resistance, corrosion resistance and wear resistance. These superalloys require vacuum grade ferroniobium, nickel-niobium and pure niobium. Vacuum grade has a higher purity than high purity grade and is made from high purity niobium oxide powder as opposed to ore concentrate.

In the passive electronic industry, niobium based capacitors are a growing replacement to tantalum based capacitors. Capacitors are widely used in computers, mobile phones and many other electronic devices. Some of the companies offering niobium capacitors are Vishay, NEC, Epcos and AVX

B. Niobium Based Type II Superconductors

The application of type II superconductors is such that the specifics of materials used, strengths of magnetic field produced, size of magnets used, tolerances, cooling methods, magnetic field activation times, critical current, critical field and many other variables are extremely broad. Of the many low temperature

superconductors, Nb_3Sn and NbTi are the most widely used and researched. This section is intended to point out the latest in technological problems and breakthroughs by looking at applications and manufacturing methods.

Niobium is a transition/refractory metal that is frequently used as a type II superconductor in the form of Nb_3Sn, NbTi and more recently, Nb_3Al. Type II superconductors are produced in multifilament form. For example, commercially available NbTi composite superconducting wires are 0.5 to 2 mm in diameter with up to 5000 filaments per wire resulting in filaments on the order of microns in diameter. Such small diameters along with high filament densities are what makes the manufacturing process so challenging and is what motivates this research. To better understand the difficulties of type II superconductors, one must first look into the different manufacturing methods. Although specific manufacturing techniques are well kept secrets, these methods involve numerous steps which include extrusion, drawing and heat treatment. Typical manufacturing processes include Internal Tin, Jelly Roll, and Copper Bronze diffusion. For example, Internal Tin is a Type II superconductor manufacturing process that draws numerous niobium rods with tin cores. The niobium/tin sub elements are then jacketed in copper and further reduced by drawing. The product is heat treated to form stochiometric Nb_3Sn at the niobium/tin intersections by interfacial reaction resulting in niobium/tin filaments that have diameters on the order of the Nb grain size. If the grains of the niobium are large or irregular, strains may not have axial symmetry, thereby causing some of the filaments to come in contact with each other or to break. Furthermore, coalescence and breakage increases the hysteresis loss during AC operation. To further complicate matters, Nb_3Sn superconductors must be preshaped prior to heat treatment due to the brittle nature of Nb_3Sn. From this manufacturing point of view, one can conclude that the ideal manufacturing process should result in continuous, thin and symmetric filaments. Furthermore, filaments should be evenly spaced without coming in contact with each other after the heat treatment. In order to reach these manufacturing goals, uniform plastic deformation is essential. As a superconductor deviates from these ideal manufacturing process objectives, degradation of superconducting characteristics such as critical current can occur.

Another consideration is the formation of undesirable Cu-Ti-Nb intermetallics in Nb-Ti filaments. One method of reducing these intermetallics is by wrapping a diffusion barrier of Nb or Ta around the filament. However, this barrier can undergo nonuniform deformation during the wire reduction process, resulting in thin areas. One study has shown that a reduction of the niobium grain size can reduce the variation of the Nb barrier thickness[2]. Another study has shown that the tensile strength of Nb_3Sn decreases with increasing grain size[3]. This is of concern because type II superconductors operate at very low temperatures, $T < 20^oK$ and at high magnetic fields, > 10 T. Under such conditions, degradation of superconductor characteristics can occur due to strain caused by electromagnetic forces and by differences in thermal expansion coefficients of the various metals. Studies have shown that mechanical strain of Nb_3Sn superconductors caused by both

electromechanical forces and thermal contraction during cool-down can also have an adverse affect on the critical current[4].

Therefore, one can conclude that the microstructure of niobium is of considerable importance in improving the critical current of niobium based type II superconductors. It is believed that defects such as cracks, fractures and nonuniform deformation can be reduced in niobium based type II superconductors by both decreasing the grain size and by producing a more uniform microstructure. Previous investigations have shown that thermomechanical processes such as ECAE followed by annealing results in a reduction of grain size in various metals[5,6,7,8].

Reducing the grain size of type II superconductors also improves the superconducting characteristics at the atomic level. Associated with type II superconductors is the fact that the magnetic field is able to penetrate into the superconducting material. If the field stays between two critical values, denoted H_{c1} and $H_{c2,}$ then the material will be in the superconducting state called the mix state. In this state, magnetic vortices are produced and it is essential to "pin" these magnetic vortices so as to maintain the superconductivity. One method of pinning these vortices is with sufficient quantities of microstructural defects such as grain boundaries or dislocations[9]. Decreasing the grain size will increase the number of grain boundaries, therefore it is desirable to reduce grain size. Furthermore, studies have shown that a reduction of grain size increases the maximum pinning force in pure niobium[10]. Another study has shown that for bronze processed Nb_3Sn, a reduction in grain size distribution results in a sharper normalized critical current[11].

1. Bronze Method

The bronze method is the most common manufacturing process used to produce Nb_3Sn superconductors. This method consists of numerous drawings and heat treatments. The first step involves placing niobium rods in a bronze (CuSn) matrix and drawing this composite to produce NbCuSn wires. The composite wires are then each jacketed in a tantalum diffusion layer and stacked in a bundle. This bundle is then stacked in a Cu billet for further drawing. This results in multifilament coaxial filaments. Each coaxial filament consists of three sections, a niobium core that is surrounded by an annulus of CuSn and each CuSn annulus surrounded by a tantalum annulus. A final heat treatment produces Nb_3Sn by diffusing the niobium into the bronze annulus. The tantalum annulus serves to keep the Sn from diffusing into the copper matrix which would increase the residual resistivity of the copper. Note also that Sn has a considerably lower melting point and flow stress than the other metallic components.

2. Nb_3Sn

Nb_3Sn superconductors are in the most advanced state of development for high field applications when compared to other low temperature superconductors and are available in long cables from numerous manufacturers. In superconducting accelerator magnets, Nb_3Sn wires exhibit large magnetic fields due to high critical current densities and large filament diameters. Nb_3Sn superconductors are capable of producing fields in excess of 20 T at 4.2^o K[12]. The major reason why Nb_3Sn superconductors are the most widely used is that they are able to produce a magnetic field twice that of NbTi for the same size of wire. The major drawback of Nb_3Sn superconductors is that they are brittle because they belong to the A15 crystallographic family. This brittle nature makes them highly strain sensitive. This brittle nature requires that the coils be formed prior to heat treatment, which forms stoichometric Nb_3Sn. Furthermore, tight bending of the conductor at the ends of the coil can cause significant degradation of the critical current. Degradation of the critical current density occurs at high magnetic fields, hence limiting the use of Nb_3Sn superconductors in large-scale applications. Serious degradation of the critical current occurs in Nb_3Sn at strains of a few tenths of a percent. This is where finer filaments help to decrease this mechanical strain.

3. NbTi

NbTi superconductors are used when field requirements are not as high as those which Nb_3Sn based superconductors can produce. The critical field, B_{c2}, is 10.5 T at 4.2^o K and it is 13.5 T at 1.9^o K[12]. The major advantage of NbTi superconductors is that they are highly ductile. NbTi superconductors can withstand tensile strains up to two or three percent without significant degradation of the critical current density. The major drawback is that they require large amounts of cold work and numerous heat treatments in order to produce large critical current densities. Cold work and heat treatments produce precipitation of α-Ti particles which are necessary to pin the magnetic flux. This pinning is necessary to produce high critical currents, J_c[13]. These αTi particles also pin dislocations and vacancies which harden the material. Conversely, the heat treatments soften the copper which can cause sausaging of the filaments.

4. Nb_3Al

Nb_3Al superconductors are a more recent niobium based superconductor and are of interest because they can produce high magnetic fields, B_{c2} = 30 T at 4.2^o K, high critical current densities and have a dramatically better strain tolerance. The major disadvantage of Nb_3Al superconductors is that the aluminum dimensions should be less than 100 nm in the finished wire. Such small dimensions are difficult to achieve. The jelly roll process is the most common and reliable manufacturing method along with heat treatment diffusion at 750^o

C. The Japan Atomic energy Research Institute (JAERI) has developed a 46 kA, 13 T cable with a thermal strain < 0.4% so the critical current degradation is less than 10% at 13 T[14].

5. Ultra High Strength "Continuous" Cu/Nb Conductors

In the ever increasing goal of producing large magnetic fields, type II superconductors are subject to extremely high stresses. To prolong the usefulness of such superconductors, it is essential that the materials stay in the elastic range during operation. This is challenging because a 100 T magnetic field is capable of producing stresses at the 2.2 GPa level. Note that this is well above several important mechanical properties of both niobium and tantalum. For instance, the annealed strength for niobium is 105 MPa and for tantalum it is 170 MPa which is approximately 10 to 20 times less than the stresses produced by a 100 T field. Under these conditions, the material will far exceed the elastic limit. From this one can conclude that the elastic limit of individual metals cannot be achieved with bulk materials and another approach, such as the use of nanocomposites, is required[15].

High strength superconductors have been produced with ultimate tensile strengths of 1.9 GPa at 77 K at the Laboratoire National des Champs Magnetiques Pulses (L.N.C.M.P.) in Toulouse France[15]. The new generation of continuous Cu/Nb composites are 28% Cu by volume with a cross section of 5 mm^2 containing 52.2×10^6 Nb nanofilaments. Each nanofilament has a diameter of 140 nm. Further improvement of mechanical properties can be achieved by increasing the number of nanowhiskers and by using other bcc reinforcing metals with higher shear moduli[15].

6. Production of 11 km Long Nb_3Al Strand by Jelly Roll

Fusion research is a field that requires large scale magnets that produce large magnetic fields. What separates fusion magnets from other superconducting magnets is the requirement of large magnets as opposed to smaller ones that are required in medical equipment. As a result, longer strands are required which is of interest from the manufacturing point of view. Furthermore, the overall displacement of the strain is larger because the filaments are longer. Therefore, the goal of the manufacturing industry is to produce less strain sensitive superconductors. This has been achieved by the joint effort of the Japan Atomic Energy Research Institute (JAERI) and Hitachi Cable, Ltd[16]. They have developed a method for making Nb_3Al strands as a substitute for Nb_3Sn strands. The advantage of Nb_3Al is that it is less strain sensitive than Nb_3Sn[17].

7. Cryogen-Free 23 T Hybrid Magnet

Gravity-free processing is a subset of materials processing that attempts to produce materials under conditions of zero gravity or by producing forces that counter gravity. One method of counter gravity processing utilizes high magnetic fields. This method is applicable to diamagnetic materials. Ideally, the system should produce large fields and for long magnetic activation times in order to accommodate for a broad range of techniques to produce a broad range of materials. Associated with the long magnetic activation time is the requirement of a large amount of helium which is needed to cool the superconductors. Therefore, the production of a cryogen-free magnet would be of considerable interest to the field of gravity-free materials processing. At the U.S. High Field Magnetic Laboratory for super conducting Materials, such a magnet is being produced[18].

This new magnet is a hybrid magnet comprised of three sections. The outer section is a super conducting magnet made of NbTi. The middle section is a superconducting magnet made of highly strengthened CuNb/Nb_3Sn multifilament wires. Both superconducting magnets are cooled by Gifford-McMahon crycoolers. The inner magnet is a water-cooled resistive magnet. When the magnets are combined, they are capable of producing a 23 T magnetic field in a room temperature 52 mm bore. In theory, the NbTi coil is capable of producing a field of 4.59 T at 198 amps and the CuNb/Nb_3Sn coil is capable of producing a field of 3.41 T at 145 amps. Although this adds to 8.0 T, the superconducting magnets will run at 7.5 T when combined with the resistive magnet because of safety considerations. The resistive magnet is capable of producing a 15.5 T field. This accounts for the total field of 23 T. The need for a resistive magnet can be demonstrated with the magnetic force on a diamagnetic material.

$$F = \frac{\chi}{\mu_o} B \frac{dB}{dz} \qquad (2)$$

Note that the force is proportional to the magnetic field and the field gradient. The field gradient is produced by the resistive magnet.

C. Niobium Based Variable Capacitors

The majority of superconducting circuits used in industry is based on niobium and operate at high frequencies, typically in the GHz range. Tuning, such as impedance matching, is of considerable concern for high frequency circuits because the range of applications is broadened. One method of tuning impedance is with variable capacitors. Recently, micron size variable niobium capacitors have been produced[19]. These

capacitors are in the form of thin film air bridges. If the bridge is modeled after a simple plate capacitor, the capacitance is the following:

$$C = \frac{\varepsilon_o}{d} A \qquad (3)$$

where ε_o is the permittivity of free space, A is the area of one plate and d is the distance between the plates. From this formula, one can see that the capacitance can be varied by changing the distance between the bridge and the ground electrode. This is done by applying a voltage across the bridge and the ground electrode. One particular advantage of this type of capacitor is that it can be fabricated to other parts of the superconducting circuit because both the capacitor and the circuitry are made of niobium or niobium based materials. Furthermore, these capacitors have been produced on the micron scale. The thickness of the bridges ranges from 200 to 700 nm with widths of 50 to 300μm. The air gap between the bridge and the ground electrode is 5μm at zero volts. Due to the fabrication process, stresses warp the bridge to give it a saddle shape with the height at the center of the bridge slightly lower than at the ends. This stress has been measured at 10-30 MPa. It is believed that capacitance values of 15-100 fF can be achieved with 50-300 μm wide and 100 μm long air bridge capacitors[19]. The authors involved in this research believe that further developments in the fabrication of niobium air bridge capacitors will include stress reduction.

D. Niobium Based Electrolyte Capacitors

Paramount in the computer and mobile telecommunications industry are the ongoing goals of miniaturization and increasing reliability. Included in these goals is research to improve the characteristics of solid electrolyte capacitors. Currently, electrolyte tantalum capacitors are widely used in the previously mentioned industries, but a new capacitor that substitutes niobium for tantalum has been produced[20]. The substitution of niobium for tantalum is promising because it has several more favorable qualities one of which is it has a lower raw material price. This has the potential of affecting the market for tantalum because the capacitor industry is the largest consumer of tantalum, approximately 60%[21]. Furthermore, the dielectric Nb_2O_5 has a higher relative permittivity, K_e, than that of Ta_2O_5. The importance of a higher relative permittivity can be demonstrated by considering the capacitance of an ideal parallel plate capacitor with a linear isotropic homogeneous dielectric. The capacitance, C, is:

$$C = \frac{\varepsilon A}{d} = \frac{\mathrm{K}_e \varepsilon_O A}{d} \qquad (4)$$

where, K_e is the relative permittivity of the dielectric, ε_o is the permittivity of a vacuum, A is the area of one plate and *d* is the distance between plates. The capacitance is an increasing function of the relative permittivity.

The niobium components of this new type of capacitor consist of a niobium anode and a niobium pentoxide dielectric, Nb_2O_5. The first step in processing involves pressing and sintering fine, porous capacitor grade niobium to form the anode. The niobium pentoxide layer is then formed by a two stage anodic oxidation process of the niobium anode. This process produces a nanoscale amorphous pentoxide layer.

E. Body Center Cubic Characteristics

Plastic deformation in single crystals occurs along preferred crystal planes and directions. Although there are three common laws that govern slip, exceptions do exist. The laws are: slip directions tend to be along the close pack planes, slip planes are the close packed planes and for a given set of slip planes and directions, the crystal operates in that system such that the resolved shear is the largest. In bcc crystals such as niobium, the close pack direction is the <111> direction, but the planes may be {112}, {110} or {122}. Preferred slip planes are also highly temperature dependent for bcc crystals.

$$\{112\} \text{ for } T<T_{melt}/4 \quad (5)$$

$$\{110\} \text{ for } T_{melt}<T<T_{melt}/2 \quad (6)$$

$$\{122\} \text{ for } T>T_{melt}/2 \quad (7)$$

F. Plastic Deformation Theories

Plastic deformation of metals can be considered isotropic or anisotropic. Most metals in polycrystalline form are considered plastically isotropic. However, polycrystals are a conglomeration of single crystals which are anisotropic. Therefore, in order to consider whether a polycrystalline material can be considered isotropic, it is necessary to consider the size of individual grains relative to the bulk material. For example, as grain size approaches material size, the accuracy of isotropy reduces because individual grains behave anisotropically. Likewise, as a work piece becomes smaller relative to its grain size, accuracy of the isotropy assumption diminishes. Furthermore, grain homogeneity should be considered. Homogeneity can refer to grain orientation, grain size morphology and microstructures such as dislocation cells. For example, if a material has a narrow grain size distribution with random orientation, accuracy of isotropy is improved. This is of increasing importance in the field of microelectronics because of the ever increasing goal of industry to reduce the size of niobium components such as superconducting filaments and variable capacitors. The goals of this research are to improve the plastic deformation processes of pure niobium by reducing the grain size

and by producing a more homogenized microstructure. The improvements include increased strength and uniform plastic deformation. The method of reaching this goal is the thermo mechanical process of Equal Channel Angular Extrusion/Annealing.

The theory of plastic deformation can be analyzed from three major perspectives, the macro scale, the micro scale and the thermodynamic view. Each perspective attempts to explain observations by numerous theories. The macroscale views the deformation as a continuum mechanics process and the material is called the body.

1. Plasticity Theory from Macro Scale View

The macroscale perspective contains mathematical theories in plasticity and is formulated at the macroscopic level considering experimental observations such as stress and strain. Experiments on the macroscopic scale can involve observations of stress/strain relationships, upper yield point, work hardening, hydrostatic pressure effects, the Bauschinger effect, rate effects and temperature effects. Because of the complexities of macroscopic plasticity theory, idealizations with stress/strain relationships have been developed by various individuals. Some of these relationships are:

$$\sigma = \sigma_y + H\varepsilon^n \qquad \text{(Ludwick 1909)} \qquad (8)$$

$$\sigma = H\varepsilon^v \qquad \text{(Holloman 1944)} \qquad (9)$$

$$\sigma = \sigma_\psi + (\sigma_\sigma - \sigma_\psi)[1 - e^{(n\varepsilon)}] \qquad \text{(Voce 1948)} \qquad (10)$$

$$\sigma = H(\varepsilon_\sigma + \varepsilon)^v \qquad \text{(Swift 1947)} \qquad (11)$$

$$\sigma = \sigma_\psi \tanh(E\varepsilon/\sigma_y) \qquad \text{(Prager 1938)} \qquad (12)$$

$$\varepsilon = \sigma/E + H(\sigma/E)^v \qquad \text{(Ramberg and Osgood 1943)} \qquad (13)$$

E, σ_y, σ_s, ε_s, H and n are material constants which must be determined experimentally[22].

Saint-Venant in 1870 made the first attempt to relate stress to strain in plastic deformation and this relationship was later generalized by Levy in 1870 and 1871. Later called the Levy-Mises theory of plasticity, it considered the elastic strain to be negligible and the increment of strain $d\boldsymbol{\varepsilon}$ to be coaxial with stress $\boldsymbol{\sigma}$, where $d\boldsymbol{\varepsilon}$ and $\boldsymbol{\sigma}$ are third order tensors. In order to consider the yield point, the concept of yield surfaces arose. Yield surfaces are surfaces in six dimensional stress space that define the separation of elastic

and plastic deformation. There are various representations of yield surfaces and can be divided into two main categories, for metals (considered pressure independent) and for pressure sensitive materials. For metals, the Maxwell-Huber-von Mises and the Tresca criterion are common models. These models can be utilized to approximate work hardening. Two of the more common approximations are isotropic hardening and kinematic hardening. Isotropic hardening materials allow the yield surface to change shape without translation while kinematic models are assumed to have yield surfaces with constant shapes that can translate. The kinematic model allows for the Bauschinger effect while the isotropic model does not.

2. Plasticity Theory from Micro Scale View

Plasticity from the microscale view considers the deformation as a discrete process which involves the displacements of atoms. The microscale perspective contains what are called physical theories in plasticity and are formulated at the microscopic level considering atomic movement and crystal deformation. In 1900, Rosenhain and Ewing observed parallel steps, called slip bands, on the surface of metals that had undergone plastic deformation on the microscopic scale. This suggests that the slip bands were the result of shear strain and are called shear bands. Furthermore, Rosenhain and Ewing observed that the direction of the shear bands changed shape and direction at grain boundaries. This hinted that plastic deformation of individual crystals should be investigated, which is what inspired Anrade, in 1910, to develop a technique for growing large single crystals[22]. Further research proved that plastic deformation on the microscopic scale is inhomogeneous and that shear occurs along directions associated with crystallographic planes. This implies preferential slip. Although there is a clear link between slip directions and crystallographic planes, this did not explain the strength of the slip. Observations showed that actual strength was considerably less in magnitude than what was predicted. This discrepancy was explained with dislocation theory which was introduced independently in 1934 by, Orowan, Polanyi and Taylor[22].

The underlying basis for dislocation theory can be visualized at the atomic level by crystal defects called dislocations. Dislocations can be divided into 3 major categories which are, edge dislocations, screw dislocations and mixed dislocations. What sets dislocations apart from other defects is that they have a measurable length as opposed to a point defect such as an interstitial. For example, an edge dislocation is the continuous absence of atoms in a crystal structure resulting in a stress field along the dislocation and penetrating into the surrounding area. These long range defects significantly increase a materials strength and effect preferential slip. Due to the complexity of dislocation movement, an increase in dislocations can either increase the strength of a material. For example, if there is an increase in the number of dislocations in a material due to an increase in strain, the material may become work hardened due to the interaction of dislocations with each other. This is due to the fact that dislocations become entangled and hinder each other's movement.

3. Plasticity Theory from Thermodynamic View

Thermo-mechanical processes may be described by various combinations of plastic deformation and heat treatments. Because plastic deformation is associated with the dissipation of heat, it is an irreversible process thereby making it path dependent. Likewise, heat treating may be associated with crystal formation and crystal growth. It too is an irreversible process. Therefore, a thermomechanical process is an irreversible or path dependent process. When work is done on a system in the form of plastic deformation, the internal energy of the system is increased due to strain energy. This strain energy is located at the microscopic level in the form of a distorted crystal. It is the utilization of this strain energy that makes it possible to alter the electrical and mechanical properties of metals by altering the microstructure. Furthermore, by annealing a cold worked metal, sufficient energy can be imparted to the atoms such that they will minimize their strain energy by forming a more ordered arrangement (i.e. recovery, polyganization and recrystallization).

Plastic deformation may be divided into two major areas which are, hot working and cold working. Cold working is the process of plastic deformation which takes place below the material's recrystallization temperature. It is associated with imparting a larger amount of strain energy into the system than hot working. Therefore, this research will utilize cold work via ECAE.

G. Equal Channel Angular Extrusion

Equal Channel Angular Extrusion is a technique by which a material undergoes simple shear by changing the direction of the material through a die channel that is angled. This technique has been used in the area of metallurgy since it was first developed in the late 1970's by V. M. Segal, V. I. Reznikov and A. E. Kopylov. The die has equal inlet and outlet dimensions so the shape of the material is virtually unchanged. Typical dies have a square or round inlet and a square or round outlet with a die angle of 90^{o}. The size of the channel die can vary but is limited by the materials ductility, die angle and pressing capabilities. Figure 1 is a diagram of an ECAE die with a square inlet, square outlet and a 90^{o} angle. Note the difference in the engraved parallel marks before and after the shear zone. Several empirical formulas are presented.

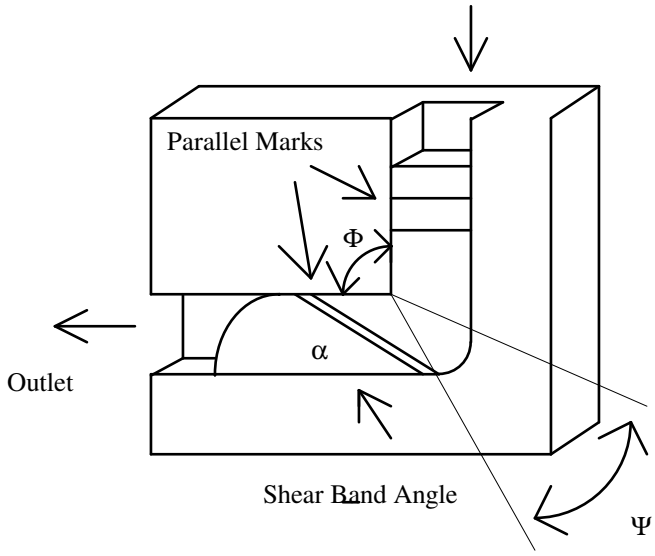

Figure 1. Cross Sectional View of ECAE Die and Work Piece.

1. Segal's Strain Model

Segal derived an equation for the total strain where $\Psi = 0$ and N represents the number of passes[23].

$$\varepsilon_n = \frac{2N}{\sqrt{3}}\cot(\frac{\Phi}{2}) \qquad (14)$$

Note that this equation does not consider path dependence and for $\Phi = 90$, the strain becomes 1.15N.

2. Iwahashi's Strain Model

Iwahashi derived an equation for the total strain where $\Psi \neq 0$ and N represents the number of passes[24].

$$\varepsilon_n = \frac{2N}{\sqrt{3}}\left[\cot(\frac{\Phi}{2}+\frac{\Psi}{2})+\frac{\Psi}{2}\cos ec(\frac{\Phi}{2}+\frac{\Psi}{2})\right] \qquad (15)$$

3. Goforth's Strain Model

$$\varepsilon_n = \frac{N}{\sqrt{3}}\left[2\cot(\frac{\Phi+\Psi}{2})+\Psi\right] \qquad (16)$$

This equation is based on calculations by Cui[25].

H. Grain Refinement of Tantalum via ECAE/Annealing

Because tantalum and niobium have the same crystal structure (bcc), similar chemical properties and similar physical properties, it is believed that promising results of grain refinement of tantalum via ECAE/Annealing is substantial evidence that promising results will result with niobium. Table 1 shows some of the more relevant properties of both elements[26].

Table 1. Properties of Niobium and Tantalum.

Property	**Niobium**	**Tantalum**
Metal Classification	Refractory	Refractory
Crystal Structure	bcc	bcc
Annealed % Reduction Area at Fracture	80	80
Annealed % Elongation at Fracture	30	30
Tension Elastic Modulus [Gpa]	103	186
Cold Worked Ultimate Tensile Strength [Mpa]	585	650
Cold Worked % Elongation	5	5
Annealed Ultimate Strength [Mpa]	195	285
Annealed Yield Strength [Mpa]	105	170
Poisson's Ratio	0.38	0.35
Strain Hardening Exponent	0.24	0.24
Recrystallization Temperature [^{o}C]	800 - 1100 ^{o}C	900-1200 ^{o}C
Annealed Vickers Hardness	60	90
Cold worked Vickers Hardness	150	210
Melting Point [^{o} C]	2468	2996

Essential to this work is the workability of niobium under cold ECAE conditions. This is because the proposal has involved putting niobium under high shear strains of 1.16, 2.23, 4.64 and 9.28. Although not all

refractory metals have good cold working properties, both niobium and tantalum have excellent cold working properties[26].

Previous results of grain size reduction of tantalum via ECAE/Annealing have shown that tantalum is very workable under ECAE with a die angle of 90°[21]. ECAE was performed with tantalum to strains of 1.16 (1 pass), 2.32 (2 passes) and 4.64 (4 passes) without difficulty. Upwards of four passes were achieved easily with no significant increase in press load and without intermediate annealing. Vickers microhardness showed an increase in hardness after two passes from 85 HV_{300} to 220 HV_{300}[21]. Both routes 2C and E resulted in grain refinement of tantalum with the E route producing the finest and most homogeneous grain texture. Furthermore, ECAE may produce a more homogeneous microstructure than conventional processing methods such as rolling, swaging, forging and wire drawing. Recrystallization temperatures were shown to decrease with increasing strain[21].

I. Previous Work on Cold-Rolled Niobium Bicrystal

Although previous work on ECAE of large grained niobium was not found, literature was found on the recrystallization behavior of cold rolling on course-grained niobium. Their research cold-rolled a bicrystal cut from the center of a course-grained multiple electron-beam ingot in 2002[27]. The material used in the research was similar to the material used in our research. Both samples were electron-beam ingots with large columnar grains in the axial direction of the ingot. The bicrystal was then cold-rolled at three different reduction levels, 33 %, 50 % and 70 %. Vickers hardness tests (100g) were performed to determine the work hardening behavior of two grains. The microstructure was investigated prior to the rolling, after the rolling process and after vacuum annealing of the rolled material. The annealing took place for 1 hr at 800° C and 900° C.

The deformation of the cold-rolled bicrystal showed that inhomogeneous deformation occurred in both crystals. This was evident by the deformation banding morphology. Banding occurred in both crystals and tended to be arranged in colonies. The widths of the bands ranged from 10-100 μm. Misorientations between individual bands was quantified by Electron Backscatter Diffraction and found misorientation of bands ranged from 8° up to 55°. The work hardening behavior of both crystals was different. The average Vickers hardness of grain B was larger than that of grain A prior to rolling and after 33 %, 50 % and 70 % reductions.

J. Previous Work of the Effects of Grain Size on Dislocation Density and Flow Stress of Niobium

The effect of grain size on dislocation density and flow stress of niobium was investigated in 1967 by H. Conrad, S. Feuerstein and L. Rice[28]. Their research investigated 125 μm thick niobium foils under tension

at room temperature. The original grain sizes ranged from 32 μm to 435 μm and were achieved by cold rolling/annealing. Constants for the following equations were investigated.

$$\sigma = \sigma_f + \alpha G b \rho^{\frac{1}{2}} \qquad (17)$$

where σ_f is a friction stress due to obstacles other than dislocations, α is a constant ranging from 0.2 to 1.0, G is the shear modulus, b is the Burgers vector and ρ is the dislocation density. Table 2 shows the constant values for the Hall-Petch equation. Their research yielded the constant, α, to be 0.88. Equation 18 is the Hall-Petch equation.

$$\sigma = \sigma_i + K d^{-\frac{1}{2}} \qquad (18)$$

Table 2. Constant Values for Pure Niobium Hall-Petch Equation.

Yield	σ_i [kg/mm2]	K [Kg/mm $^{3/2}$]
Upper Yield	6.5	1.6
Lower Yield ($\varepsilon_p \approx 0.01$)	5.7	1.25

In summary, their research led to the following conclusions.

1. The dislocation density is a linear function of strain up to the point that a cellular network is developed.
2. The dislocation density is proportional to the reciprocal of the grain size for a given strain.
3. The tensile flow stress is a function of the square root of the dislocation density and σ_f is independent of grain size for grain diameters less than the foil thickness.
4. Cellular networks develop for strains of 10%.
5. Cell sizes for a given strain are proportional to the square root of the grain size.
6. Flow stress is a linear function of the reciprocal of the cell size.

CHAPTER III

MATERIALS AND EXPERIMENT PROCEDURES

A. Overview/Test Matrix

The materials that were investigated include pure niobium from two sources: References Metals Corporation located in Bridgeville, Pennsylvania and Wah Chang located in Albany, Oregon. The Reference Metals sample came in the form of a 235 mm diameter by 305 mm long electron-beam melted ingot section. The nominal purity of the ingot is 99.7% and the grain structure is oligocrystal with grains on the order of 30mm across by 300 mm long. The grains are oriented along the casting direction. The Wah Chang sample (Grade 1) came in the form of a worked 24 mm diameter by 610 mm long rod. The Wah Chang rod showes no visible grains but deformation bands are visible along the longitudinal direction. A total of 11 billets were cut from the RM ingot and two sections were cut from the Wah Chang rod. Seven of the RM billets were subjected to Equal Channel Angular Extrusion via routes 1A, 2C, 4E and 8E. Two billets underwent route 1A, two billets underwent route 2C, two billets underwent route 4E and one billet underwent route 8E. This duplication of routes was used to determine reproducibility. One of the Wah Chang sections was subjected to Equal Channel Angular Extrusion via route 4E. Processed billets were cut into specimens for 60 minute isochronal heat treatment under vacuum. Specimens were tested for impurities including interstitials, hardness, microstructure morphology and tensile properties. Brinell, Rockwell and Vickers hardness measurements were taken between extrusions to determine hardness as a function of strain. Vickers microhardness measurements were taken after heat treatments to determine hardness as a function of annealing temperature and strain. Optical microscopy was performed on as-worked and annealed samples to investigate deformation banding and grain size as a function of strain. Transmission electron microscopy (TEM) was performed to determine subgrain morphology as a function of strain. Tensile tests were performed to determine stress/strain relationships as a function route (strain) and recrystallized grain size. The major steps of this experiment are presented chronological order. Table 3 shows the test matrix for this project.

Table 3. Test Matrix for Berkeley Lab Sponsored Niobium Grain Refinement Project.

Billet ID	ECAE Route	Brinell Hardness	Rockwell Hardness	Vickers Hardness	Heat Treat	Optical Micr.	Impurity Analysis	TEM
9	0	√	√	-	-	-	-	-
10	0	√	√	-	-	-	-	-
11	0	√	√	-	-	-	√	√
12	0	√	√	-	-	-	-	-
3	1A	√	√	√	√	√	-	√
18	1A	√	√	√	√	√	-	
24	2C	√	√	√	√	√	-	√
17	2C	√	√	√	√	√	-	
2	4E	√	√	√	√	√	-	
19	4E	√	√	√	√	√	-	√
4	8E	√	√	√	√	√	-	
WC*	0	√	√	√	√	√	√	
W2*	4E	√	√	√	√	√	-	

* Wah Chang material

B. Chemical Characterization

Ten gram samples were cut from both niobium sources and sent to SHIVA Technologies in Syracuse, New York for impurities analyses. Analysis was performed by Glow Discharge Mass Spectrometry (GDMS) which is used for trace element analysis on inorganic materials such as metals. The GDMS instrument used for chemical characterization was a VG9000. This instrument can be divided into three major areas, Glow Discharge Ion Source, Mass Analyzer and the Detection System. In the Glow Discharge Ion Source, ultra high purity argon (6N) is used as the discharge gas at a pressure of one Torr. The Mass Analyzer extracts the ions at 8 kV which are separated in the double focusing high-resolution mass analyzer which is of the Nier-Johnson geometry. This set-up is capable of detecting masses between one and 260 amu at concentrations in the parts-per-trillion range by weight level. The Detection System is comprised of two detectors, a Faraday Cup and a photomultiplier. The Faraday Cup is used to detect signals greater than 10 to 13 pico amps and the photo multiplier is used for signals below the Faraday Cup Range. Table 4 shows the major impurities found for both niobium sources with the highest levels in bold lettering.

Table 4. Major Impurities [ppm wt.] of Wah Chang and RMC Pure Nb.

Impurity Symbol	Wah Chang	References Metals
B	0.42	0.12
Al	0.16	0.13
Si	6.00	0.90
P	4.90	2.60
Ti	4.30	0.03
V	0.008	0.02
Cr	0.001	0.001
Fe	0.48	0.008
Ni	0.03	0.001
Cu	18.00	0.02
Y	0.002	0.001
Zr	0.67	0.12
Hf	0.08	0.01
Ta	130.00	1200
W	5.70	0.54
Mo	0.85	0.85

C. Interstitial Characterization

Two sets of samples were cut from each niobium source and sent to Ames Laboratory at Iowa State University in Ames, Iowa for interstitial analyses. Each set had samples for three separate interstitial analyses; Carbon, Oxygen and Nitrogen. The first set from each source consisted of three specimens at the following weights, 0.5 gram, 0.1 gram and 0.1 gram for Carbon, Oxygen and Nitrogen analyses respectively. The second set comprised of approximately 50 gram samples from each source, to be cut into specimens by Ames Lab staff. Table 5 shows the interstitial analyses for both niobium sources. A Leco TC-436 analyzer was used to analyze for oxygen and nitrogen and a Leco CS-444 Determinator was used to analyze for carbon.

Table 5. Interstitial Analyses [ppm wt.] of Wah Chang and RMC Pure Nb.

Sample ID	Oxygen Concentration [ppm by weight]	Nitrogen Concentration [ppm by weight]	Carbon Concentration [ppm by Weight]
Wah Chang 2505-1A	290	78	
Wah Chang 2505-1B	170	59	
Wah Chang 2505-1C			163
RM 2505-2A	280	80	
RM 2505-2B	220	70	
RM 2505-2C			121

D. As-Received RM Nb Ingot and Wah Chang Nb Rod

Prior to cutting the as-received samples, it was necessary to map and label the various sections of the Reference Metals ingot and the Wah Chang rod. This will allow for further investigations of any mechanical and optical anomalies. This also allows for initial grain size measurements and texture. Both niobium sources were measured with a ruler and major section were marked with a Sharpie pen. The marked sections were cut lengthwise using a self-lubricating band saw. There were no problems of gumming and the cuts went smoothly. Individual billets were stamped at the ends with an identification number (ID). Figures 2 and 3 show sketches of the RM ingot with the ID number locations indicated on the transverse plane.

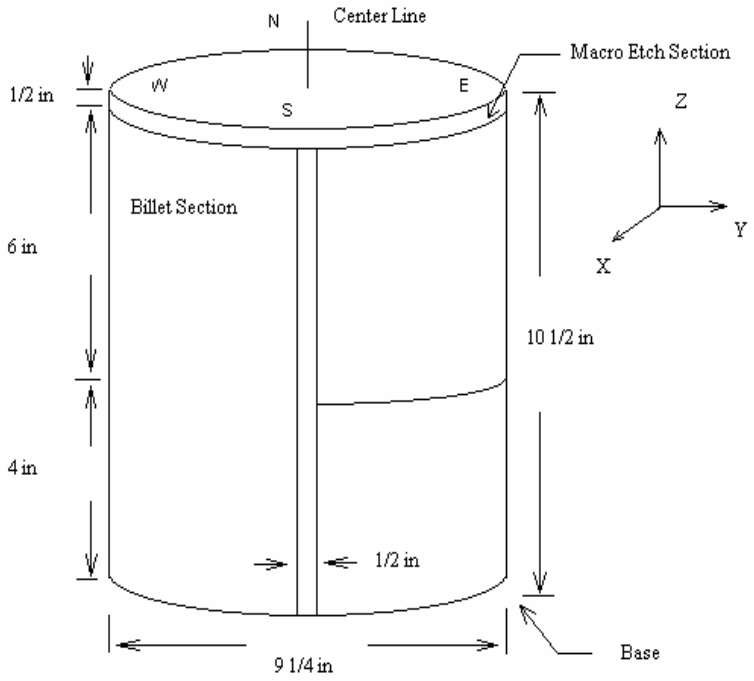

Figure 2. Side View of Reference Metals Company Pure Nb Ingot from Which Billets Were Extracted.

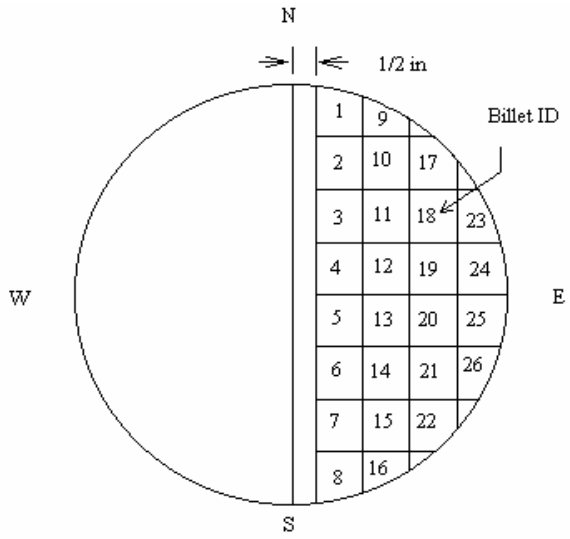

Figure 3. Top View of Reference Metals Company Billet Section Showing Extracted ECAE Billet ID Numbers.

E. Extrusion

Seven billets from the Reference Metals ingot and one billet from the Wah Chang rod were selected for ECAE. The ECAE paths chosen for this investigation were 1A, 2C and 4E and 8E. See table 3 for the billet/path test matrix. All extrusions were performed with an MTS model 810 Custom System hydraulic press at room temperature and at a punch speed of 2.5 mm/sec. All extrusions were performed with a 1 in square die and a die angle of 90^{o}. All billets were wrapped in brass shims to ease the extrusion process by reducing friction at the billet/die interface. Milling of the billets surface was required after each pass to eliminate flash which accumulates at billet edges. The Wah Chang rod became stuck in the die after the first pass requiring it to be sectioned for extraction from the die. This was in part due to the difference in shapes of the rod and die. The rod undergoes expansion in the radial direction to fill the square die cross-section. This expansion produces large friction between the rod surface and the die walls.

F. Post Extrusion Dissection/Billet

Because the billet had to be dissected into specimens for Vickers hardness, optical microscopy, TEM and tensile testing, it was first necessary to sketch the various specimens into each billet. Billets were labeled with an engraver and cut using a self lubricating Buehler diamond saw. See Figures 4, 5 and 6 for diagrams of a typical RMC billet and the Wah Chang billet with specimen locations marked. Specimens were then placed into specially marked 2" by 3" marked plastic envelopes prior to mounting in epoxy.

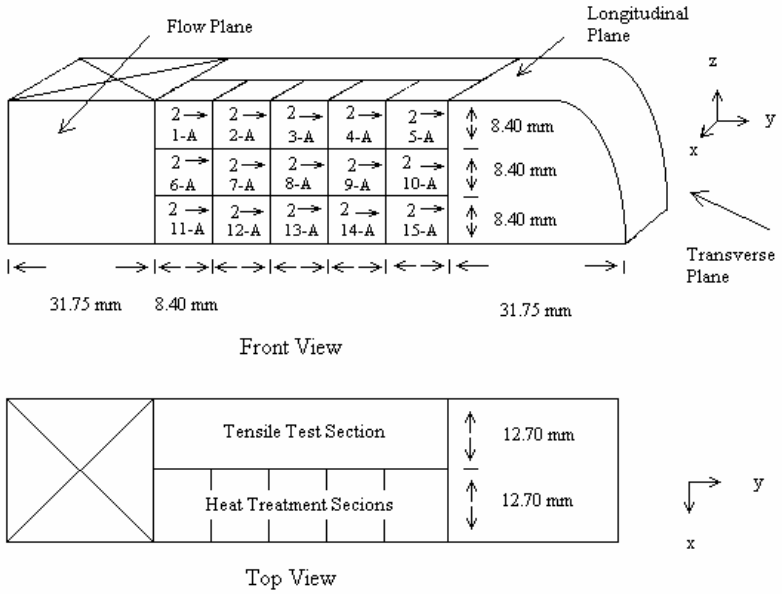

Figure 4. Typical Inscribed Reference Metals Billet at Post Extrusion and Prior to Dissection.

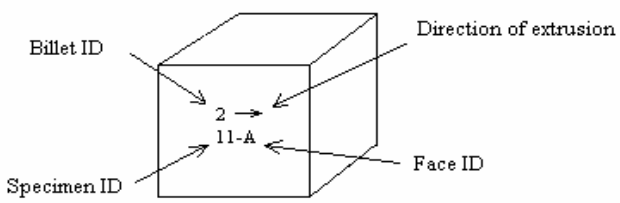

Figure 5. Definitions of Labels on Specimens.

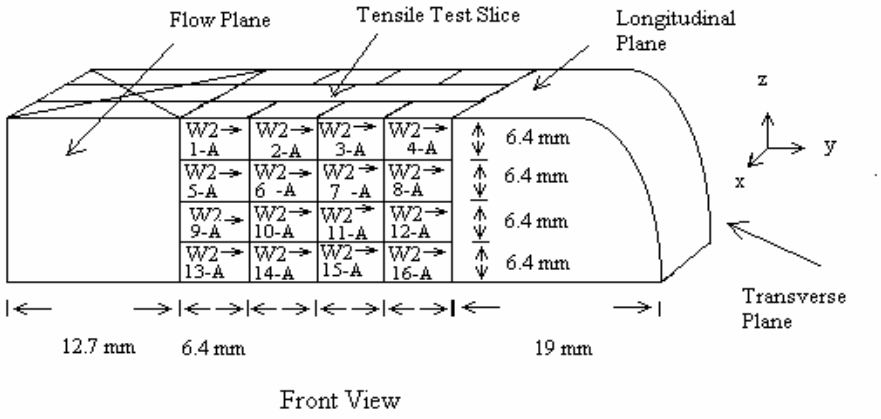

Figure 6. Inscribed Wah Chang Billet at Post Extrusion and Prior to Dissection.

G. Annealing

To reduce oxidation, all specimens were annealed under high vacuum and at constant temperature. With the exception of two billets, heat treatments lasted 60 minutes. See Table 6 for the specimen ID/annealing matrix.

Table 6. Nb ID/Annealing Matrix.

Troom	300°C	500°C	700°C	800°C	900°C	1000°C	1100°C	1200°C
3-1	3-2	3-3	3-4	3-5	3-6	3-7	3-8	3-9
18-1	18-2	18-3	18-4	18-5	18-6	18-7	18-8	18-9
24-1	24-2	24-3	24-4	24-5	24-6	24-7	24-8	24-9
17-1	17-2	17-3	17-4	17-5	17-6	17-7	17-8	17-9
2-1*	2-2*	2-3*	2-4*	2-5*	2-6*	2-7*	2-8*	2-9*
19-1	19-2	19-3	19-4	19-5	19-6	19-7	19-8	19-9
4-1	4-2	4-3	4-4	4-5	4-6	4-7	4-8	4-9
wc1*	wc2*	wc3*	wc4*	wc5*	wc6*	wc7*	wc8*	wc9*
w3D	w6D	w7D	w10D	w11D	w6E	w7E	w10E	w11E

* Specimens Annealed for 90 minutes.

H. Mounting, Grinding, Polishing and Etching of Annealed Specimens

Each annealed specimen was cut in half along the flow plane and mounted in epoxy with the unlabeled, cleanly cut surface pointing downward for grinding. The interior flow plane was chosen for hardness and optical microscopy because the outer surfaces might have some oxidation. Furthermore, outer surfaces might contain non uniform strain. Wet grinding was performed using the following grit sequence, 800, 900, 1000 and 1200. Frequent inspection was performed using an optical microscope at magnifications of 10 and 80 to insure smooth and symmetric grinding. Wet polishing was performed with a cotton cloth using 0.05 micron alumina powder, Al_2O_3. After wet polishing, specimens were etched in an acid solution of hydrofluoric acid, nitric acid and lactic acid. Table 7 shows the grain boundary etching solution[21]. Etching involved swabbing the specimens for 10 seconds using a cotton swab followed by dipping for 10 seconds. After etching, the specimens were rinsed in tap water for approximately one minute followed by rinsing with de-ionized water. Because typical acids used in metallic etching of niobium are strong, a thorough investigation was performed to determine the hazards and handling of all chemicals used for this project. Reagents used include: nitric acid, hydrofluoric acid and lactic acid. Note that hydrofluoric acid is corrosive to glass so only plastic containers were used. Consultation was first conducted with appropriate personnel at the facilities where the chemicals were used and with the appropriate personnel at the Environmental Health & Safety Department (EHSD) at TAMU. A Project Safety Analysis (PSA) was then submitted to the appropriate personnel at the Office of Engineering Safety (EH&S) and Department of Mechanical

Engineering. Acid etching was performed under approved fume hoods using protective clothing including gloves and goggles.

Table 7. Grain Acid Etching Solution for Pure Nb.

Parts by Volume	Acid
2	Hydrofluoric Acid (HF 49%)
1	Nitric Acid (HNO_3 70%)
2	Lactic Acid ($HC_3H_5O_3$ 85%)

I. Hardness Tests

The definition of hardness in the case of metals is the resistance to plastic deformation. In the field of metallurgy, hardness can be considered the resistance to indention. Because plastic deformation is a path dependent process, many methods of determining hardness are available. Some of the more common variables that distinguish the various methods are indenter shape, hardness calculation, load and time of load. All methods employ a load on an indenter which then penetrates the material. The following equation relates the load to the yield stress,

$$\text{Mean Load} = CY \tag{19}$$

C is defined as the constraint factor. Brinell, Vickers and Knoop are relatively blunt so C is usually taken as three and is primarily dependent on the shape of the indenter. Y is the uniaxial flow (true yield) stress in kPa or psi.

This research utilized three hardness testing methods at various steps in the ECAE/Annealing process. Brinell, Rockwell and Vickers tests were performed after each pass during the ECAE process to relate hardness to strain or pass number. This relationship is useful in that it shows work hardening characteristics. The following equation is an approximation that relates Rockwell b hardness to strain.

$$R_b = K_b \times \gamma^n \tag{20}$$

Where K_b is a constant, γ is the strain and n is the Rockwell hardness coefficient. This function has a positive slope yet decreasing curvature. Vickers microhardness tests were performed after various annealing treatments to relate hardness as a function of the isochronal annealing temperature. This relationship is useful

in that it shows the extent of crystallization which can be used to predict at what temperature the material starts to form new strain free grains (recrystallize).

1. Brinell Hardness

The Brinell hardness test applies a constant load for a specified time with a 5 mm or 10 mm round hardened steel or tungsten carbide ball. The hardness number is the applied load divided by the surface area of the indention. The formula for Brinell hardness is the following.

$$HB = \frac{2P}{\pi D\left(D - \sqrt{D^2 - d^2}\right)} \qquad (21)$$

Where P is the applied load in kg, D is the ball diameter in mm and d is the diameter of the indention in mm. For this research, the applied load was 500 kg (indenter was 100mm diameter) and the load was applied for a period of 10 sec.

2. Rockwell Hardness

Rockwell hardness testing applies two loads per test while measuring the difference in penetration depth and can utilize various indenter shapes and sizes. The indenter penetrates the material from the first load which is called the minor load. The indenter then penetrates further into the material because of the larger load, called the major load. The Rockwell number represents this difference in depth. Note that the first penetration involves both elastic and plastic deformation while the second penetration involves only plastic deformation. There exist standard methods that use certain loads with certain indenters. For instance, this research employed the Rockwell b test standard which utilizes a minor load of 10 kgf and a major load of 100 kgf with a spherical shaped indenter with a diameter of 1/16 in. When a ball indenter is used, the depth of penetration can be calculated with the following equation.

$$\text{Depth} = d = (130 - R_b)\times 0.002 \text{ [mm]} \qquad (22)$$

where R_b is the Rockwell b number. The depth is in units of millimeters. From this, one can calculate the volume of displaced material if the elastic strain is neglected and the indention is assumed spherical,

$$Volume = \pi R^3 \left(\frac{\cos^3(\theta)}{3} - \cos(\theta) - \frac{2}{3}\right) \quad (23)$$

where $$\cos(\theta) = \frac{R-d}{R} \quad (24)$$

R is the radius of the indenter (1/16 in) and *d* is the depth.

3. Vickers Microhardness

The Vickers microhardness test applies a single load for a designated period of time and can utilize various sized pyramidal shaped indenters made of diamond. The test relates hardness to surface area of the indention. For this research, the load was set at 300 gf and the load time was set at 13 sec. The indenter used was a pyramid shaped diamond with an angle, θ, of 136° between opposite sides. The depth of the indentation is approximately 1/7 the diagonal length. The area of the base is 0.927 times the surface of the faces. The Vickers hardness is defined as the load divided by the surface area of the indention. The Vickers hardness is calculated from the following formula,

$$HV = \frac{2L\sin\left(\frac{\theta}{2}\right)}{D^2} \quad (25)$$

where L is the applied load in kgf, and D is the length of the diagonal indention in mm. For this research, the load, L, the indenter, θ, and the applied load time were kept constant resulting in the following formula,

$$HV = \frac{0.556}{D^2}\left[\frac{kgf}{mm^2}\right] \quad (26)$$

The relation between the hardness and the yield pressure, P, is the following.

$$HV = 0.927P \quad (27)$$

The diagonals of the indention are measured and if the mean value is d and the indention is square, then the yield pressure is the following.

$$P = \frac{2W}{d^2} \tag{28}$$

From this, the diagonals ranged from approximately 60 μm for hardness values of 160 to 96 μm for a hardness value of 60. Because the depth, d, is approximately 1/7 the diagonal, it can be calculated from the following formula,

$$d = \frac{1}{7}\sqrt{\frac{0.556}{HV}}[mm] \tag{29}$$

For a given load, the Brinell and Vickers numbers are nearly equal[29].

J. Optical Microscopy

Optical microscopy was used to visually examine microstructures on the flow plane using a Nikon Epiphot metallograph equipped with a Polaroid DMC digital camera and polarizing filters. As-worked specimens were investigated to reveal deformation banding and original grain boundaries. Recrystallized specimens were examined for grain morphology and uniformity. Grain cross section areas were computed utilizing the software Image Processing Tool Kit (IPTK). IPTK is a set of Adobe Photoshop-compatible plug-ins for image processing. Because grain etching did not always result in clear grain boundaries, it was necessary to place tracing paper over each photo and trace out the grain boundaries, scale bar and photo ID. This trace was then scanned and analyzed with IPTK. The following is the sequence of commands used to calculate the grain cross-sectional areas (μm^2):

1. Scan trace and open trace in Photoshop.
2. Select Image-Mode-Grayscale.
3. Select Image-Adjustments-Threshold. Set Threshold at 150.
4. Select Filter-IP*Measure Global-Calibrate Magnification. Left click mouse at beginning of scale bar then left click mouse at end of scale bar. Enter proper length of scale bar.
5. Select Filter-IP*Morphology-Skeletonize-Thicken Skeleton.
6. Select Image-Adjustments-Invert.
7. Select Filter-IP*EDM-EDM Morphology. Select 1.
8. Select Filter-IP*Measure Features-Label Features. Select Area.

Once the grain areas (and diameters) were calculated, they were entered into a worksheet and divided into a set of 1 μm intervals for grain size distribution plots.

To verify proper grain size calculation, random grains were calculated by hand. Calculations of individual grain areas are based on a modified version of ASTM E 930-99 Referee Procedure. This procedure overlaid a grid of points over the grain. The grid used in this method consisted of 2 mm by 2 mm squares, $d^2 = 4$ mm^2 that are evenly spaced. If the grid spacing is sufficiently small, then reapplying the grid at different angles is unnecessary. The following equation was used (ASTM 930-99) to calculate the grain cross sectional area.

$$A = \frac{P(\theta)}{M^2} d^2 \qquad (30)$$

$P(\theta) \equiv$ number of grid intersections or points falling within grain plus 1/2 the number of points falling on the grain boundary where,

$d^2 \equiv$ area of individual grid squares, and

$M^2 \equiv$ magnification of photo.

Note that the magnification of the photo is the microscopic magnification with respect to the picture. Because the magnification constant is not always correct a conversion factor must be used. This conversion factor transforms the units of the individual grid areas to the magnified units and is achieved by relating the bar length on the photo with its actual measurement. This factor is the actual length of the scale bar divided by the scale bar length all squared. Note that by using a correction factor the magnification, M is set to 1.

K. Transmission Electron Microscopy

From the microscopic view, the increase in strain energy due to plastic deformation can be associated with lattice defects such as dislocations, twins and vacancies. Of the previously mentioned defects, dislocations are responsible for the majority of the strain energy and therefore, are of major consideration in a thermo-mechanical process.

When a work hardened material undergoes plastic deformation, there are three paramount phenomena taking place at the microscopic level; mode of deformation (slip direction, slip planes etc.), dislocation density buildup and dislocation arrangement. For this investigation, dislocation density and arrangement were of particular interest. At low strains, the arrangements of dislocations are expected to be homogeneous.

As the strain increases, the density of dislocations also increases upwards to 10^{11} to $10^{12}/cm^2$ [30]. The last phenomenon to consider is the fact that dislocations hinder each others movement when they come in contact with other dislocations (in their strain fields). This results in dislocations becoming entangled, producing heterogeneous arrangements called cell structures. In bcc crystals, these cell structures tend to decrease in size with an increase in strain[31]. Cell structures also tend to decrease in size with an increase in annealing temperature. In bcc and fcc metals with high stacking fault energies, the cell structures tend to form sharp boundaries[30]. Deformation temperature and extent of deformation also play a role in boundary wall sharpness.

Because dislocations are on a sub micron level, observation must be performed utilizing Transmission Electron Microscopy (TEM). This method bombards high energy electrons (200kV) onto a specimen. The electrons pass through the specimen, are diffracted by the atom planes and produce image and diffraction patterns. Image patterns show imperfections such as dislocations and diffraction patterns give crystal structure and orientation. This procedure was preformed on various samples to determine micro imperfections as a function of ECAE route and number of passes.

This research utilized the Jeol 2010 Transmission Electron microscope located at the Microscopy and Imagining Center at Texas A&M University. Prior to usage, TEM operational training was required and was successfully completed in the month of May, 2003. Biology 689 (TEM II) was audited during the summer of 2003.

1. Sample Preparation

Transmission electron microscopy sample preparation can be divided into two major steps with numerous intermediate steps. The two major steps are mechanical thinning and ion milling. Pit and scratch free sides after the mechanical thinning are essential to prevent premature holes during the ion milling process. Specimens were cut with a Buehler Isomet Precision Saw (Model 1000). Dimpling was performed with a South Bay Tech Dimpler using a polishing wheel and 0.05 μm alumina slurry until the thickness was approximately 20 μm. The sample was then ion milled at 77^o K using a Fischione model 1010 with voltage/current settings at 3 kV/5ma, 15^o beam angle and 360^o rotation. The following is an outline for TEM sample preparation steps for niobium:

1. Mechanical Thinning
    A. Cut 0.7 mm thick samples using Buehler Isomet 1000 Precision Saw.
    B. Mount sample on aluminum disc using Crystal Bond.

C. Grind sample on one side in the following sequence with Comet 3 Variable Speed Grinder-Polisher set at speed 80 rpm.
   1. 600 grit.
   2. 800 grit.
   3. 1000 grit.
   4. 1200 grit.

D. Polish with 0.05 μm alumina/water with Comet 3 Variable Speed Grinder-Polisher.

E. Turn specimen over and grind in the following sequence.
   1. 600 grit to 0.1 mm.
   2. 800 grit to 0.08 mm.
   3. 1000 grit to 0.06 mm.
   4. 1200 grit to 0.05 mm.

F. Polish with 0.05 μm alumina/water.

G. Cut 3mm disc using punch.

H. Dimple sample with 0.05 μm alumina/water to a thickness to $\approx$ 20 μm.

2. Ion mill sample with the laser set to the highest sensitivity of 10.

2. TEM Operation

1. Ensure SIP Power Supply is working by checking if the RED LIGHT is ON and that the pressure is less than 5×10^{-5} Pa. If it is off, turn the POWER OFF then back ON.
2. Check the following green LED's: V1, V2, V4, V5B, V8, V13, V17 and V21. V8 and V21 may be off if the specimen holder is off.
3. Fill out the instrument sheet.
4. Fill the trap with liquid nitrogen using plastic funnel.
5. Insert Specimen Holder.
6. Press TEXT key and input specimen information (24-3/300C). Press F NO key and type initials while leaving film number consecutive.
7. Ensure green LED of "ACCEL VOLTAGE" is lit.
8. Type HTS 10 then use "ACCEL VOLTAGE" toggle switch to decrease voltage to 100 kV.
9. Turn on HT WOBBLER on right console.
10. Lift cap of "HT" button and press once.
11. Set the following voltage steps to raise the voltage.
    A. HTS 5 from 100 kV to 150 kV.

B. HTS 2 from 150 kV to 190 kV.

C. HTS 0.5 from 190 kV to 200 kV.

12. Turn off “HT WOBBLER”.
13. Ensure “FILAMENT” LED is on. Slowly increase the filament current until it stops. Press “FILAMENT ON/OFF” button. Wait for green LED to stop flashing.
14. Select “TEM” and “BRIGHT TITL” buttons on left console. Set SPOT size 2 and □ = 2 on page 4. Use “OBJ FOCUS” knob on right panel to change objective lens current to 5.97 for 200kV (in mag 1) or 3.43 for 100 kV.
15. Find image hole (spot size 1 at 50×)
16. Focus the beam at 25 kV by using the “Z CONT” switches. Focus until the image stops moving. Press “X” button under WOBBLER to see if image moves.
17. Cross-over and adjust beam to center. Choose Spot Size 1. Chose Condenser C2 aperture located just above operator on scope column (large dot). Do at LOW and HIGH Mag. Center the beam using the 2 knobs on the condenser. Expand and converge the beam while adjusting the knobs. Also, center SHIFT X/Y.
18. Press the “COND STIGMATOR” button in drawer and correct for astigmatism using the “DEF X” and “DEF Y” dials. Check for roundness of beam.
19. Chose 100kX. We want a round beam so cross-over. Condense the beam until you get crossover then slightly decrease the current using the filament dial to obtain a filament image. Select “GUN DEFLECTOR” using the “DEF X” AND “DEF Y” dials to obtain a symmetric image with the highest brightness. Re-saturate the filament using the filament dial.
    NOTE: ShiftX/T to center beam.
20. Condense the beam and choose spot size # 1. Center the beam using the “SHIFT X” and “SHIFT Y” dials of the “GUN DEFLECTOR” and select “GUN SELECTOR” in the drawer. Then choose spot size 5 using the “SHIFT X” and “SHIFT Y” located on the console. Repeat this process several times then reset the spot size to # 2.
21. Move object to screen center and press “HT WOBBLER”. Adjust the “DEF X” and “DEF Y”, on console, dials until the image is almost stationary. Turn off the “HT WOBBLER”.
22. Turn on the POWER to the GATAN TV Control Unit and monitor.
23. Insert the Diffraction Aperture: Go to the diffraction mode by selecting the “DIFF” button. Select an aperture size from 1 to 4 “ “ and center the aperture using the OBJ Aperture Controller. Return back to “MAG 1” image mode then retract the diffraction aperture(rotate left).
24. Change the magnification to 400 k and focus the image using the “Z CONT” switches. Then adjust the beam brightness until the AUTO exposure time is longer than 2 seconds. Press the “SCREEN” button and lift the fluorescent screen. Focus the image on the monitor. Then press

the “OBJ STIGMATOR” and adjust the “DEF X” and “DEF Y” dials. Continue to adjust these dials and the focus dials until the image is in focus. NOTE - don not use a strong beam intensity. Ensure that the AUTO exposure time is longer than 2 seconds. You ma use the IMAGE SHIFT (DEF X and Y) to move the image. Adjust BRIGHT to get an image. Under focus to see a good edge.

25. Use “ Z CONT “ to focus.
26. Taking Diffraction photo.
    A. Insert Aperture
    B. Press “ DIFF “ button “
    C. Focus
    D. No AUTO for Diffraction photos.
    E. Press “ Photo “ twice.
27. Taking Regular photo.
    A. Mag 1.
    B. Withdraw aperture.
    C. Focus with “ Z FOCUS “
    D. Press “ Photo “ twice.

To use 200k memory:

1. UFC ret.
2. 0 ret.
3. 1 (200 k) ret.
4. Y ret.
5. esc.

L. Tensile Tests

Niobium is a bcc transition metal with a low ductile to brittle transition temperature (DBTT) , -150° to -250°F (-101° to -157°C). Because tensile testing was performed at room temperature, ductile fracture was expected. Ductile fracture involves substantial plastic deformation prior to fracture. This plastic deformation is followed by crack nucleation and crack propagation. Because Nb is a bcc crystal, dislocation movement occurs in numerous slip systems. As the number of dislocations increases with strain the number of dislocation pileups also increases. These pileups are unable to accommodate strain incompatibilities resulting in crack nucleations. Further strain induces crack propagation. In transition metals, it has been shown that a reduction in grain size increases both yield stress and fracture stress. The following equation is the Hall-Petch relationship:

$$\sigma_y = \sigma_o + k_y d^{-\frac{1}{2}} \qquad (31)$$

For a given grain size (d), the constants σ_0 and k_y, can be determined through tensile testing of samples.

Tensile test specimens were cut by Electron Discharge Machining (EDM) by Palma Tool & Die Co., Inc. which is located at the following address:

Palma Tool & Die Co., Inc.
716-681-4464
40 Ward Road
Lancaster, New York, 14086-9779

Blocks were packaged with schematics and sectioning instructions. ID's were scribed onto the blocks prior to mailing. Figures 7 and 8 are actual schematics for block 4.

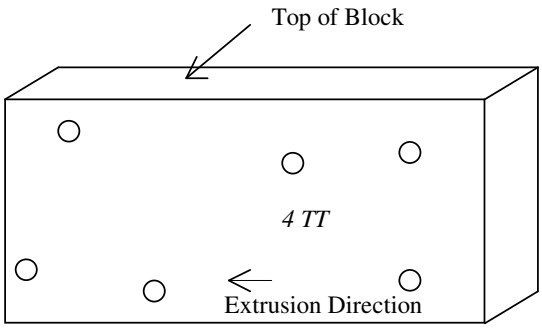

a) Front View of Block 4 Showing Brinnel Indentions

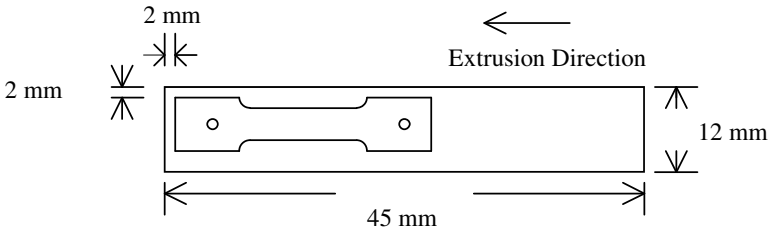

b) Top View of Block 4 Showing Outline of Dog-Bone Specimen

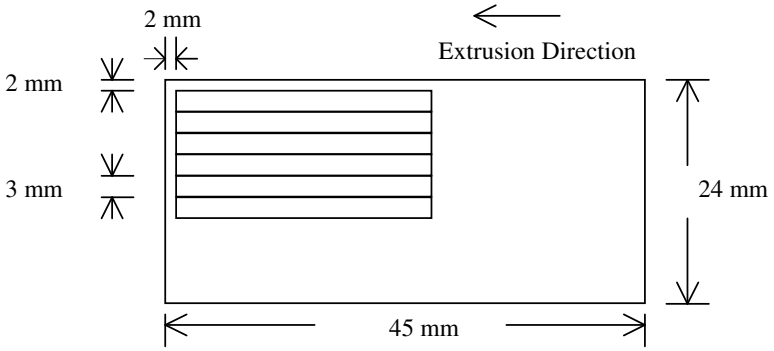

c) Front View of Block 4 Showing Outline of Dog-Bone Specimens

Figure 5.0 Dog-Bone Specimen Locations in Block 4

TOLERANCES	BLOCK 4	
XX.: ± 0.01	Niobium	OCT. 3, 2003

Figure 7. Typical Tensile Test Specifications and Drawings.

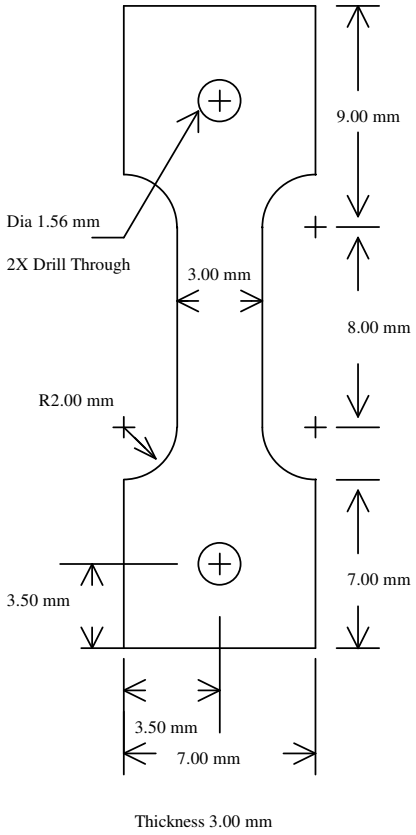

Top View of Dog-Bone Coupon

TOLERANCES	Dog-Bone Diagram	
XX.: ± 0.01 mm	Niobium	OCT. 3, 2003

Figure 8. Drawing of Tensile Test Specimens.

CHAPTER IV

EXPERIMENTAL RESULTS

A. Introduction

The goal of this research was to determine the effectiveness of ECAE/Annealing to produce a fine grained/homogenized microstructure in pure niobium from Reference Metals (RM) and Wah Chang. A total of 7 RM billets (1"×1"×6" brick shape) were subjected to ECAE via routes 1A (billets 3 and 18), 2C (billets 17 and 24), 4E (billets 3 and 19) and route 8E (billet 4). One billet from the Wah Chang (1" diameter by 6" long cylindrical rod) source was subjected to ECAE route 4E (billet W2). A total of seven tests were performed to investigate the microstructure evolution and mechanical properties of the as-received, as-worked and worked/annealing samples. The tests included Brinell hardness, Rockwell b hardness, Vickers hardness, optical microscopy (OM), transmission electron microscopy (TEM) and tensile tests (TT). Independent variables were processing route, strain level and annealing temperature. Dependent variables were hardness (Brinell, Rockwell and Vickers), deformation banding (OM), grain size (OM), grain size distribution (OM), spatial grain size (OM), strain failure (TT), 0.2 % yield stress (TT), ultimate tensile strength (TT), toughness (TT), sub-grain size (TEM), sub-grain morphology (TEM) and dislocation density (TEM).

B. Brinell, Rockwell and Vickers Hardness Results of Reference Metals Company Material

All billets subjected to ECAE were tested for work hardening characteristics after each extrusion pass by Rockwell B, Brinell (500kg for 10 sec) and Vickers (300 gf for 13 sec) hardness measurements. Hardness for each billet was averaged (5 for Rockwell, 10 for Vickers and 3 for Brinell) after each pass. The average hardness values as a function of passes are plotted as a function of number of passes in Figure 9. Observations of hardness measurements show that similarities exist between all three tests. The Brinell and Rockwell tests show a dramatic increase in hardness with the first pass, moderate softening after the third pass, maximum hardness after the sixth pass and modest softening after the seventh pass. The Vickers test shows moderate softening after the second pass. The Brinell hardness tests show that the as-received material has a hardness of 59 and reaches a maximum of 136 after six passes. The Rockwell b measurements show that the as-received material has a hardness of 10 and reaches a maximum after six passes of 86. Vickers hardness measurements show a maximum hardness after eight passes. The standard deviations of the Vickers hardness decreased with strain while the standard deviations of both the Rockwell and Brinell were more erratic.

The relationships found between the Rockwell, Brinell and Vickers hardness can be approximated by the following formulas.

$$Brinell \approx Rockwell + 50 \qquad (32)$$

$$Brinell \approx Vickers + 70 \qquad (33)$$

The major differences between the hardness tests were the standard deviations. The standard deviations for the Brinell tests were larger than those of the Rockwell. This is in part due to the fact that Brinell tests measurements are larger. It should also be noted that the indention caused by the Brinell test resulted in square shaped indentions with rounded corners. This shape was most pronounced in the as-cast material with the shape becoming more round with strain level. As a result of such an unusual shape, the average diameter was taken and used in the Brinell hardness measurements. Figure 10 shows a schematic of a typical Brinell indention. Typical values for d_1 and d_2 are 3.0 mm and 3.3 mm respectively for the as-cast material. The average of d_1 and d_2 was used for the Brinell hardness calculations.

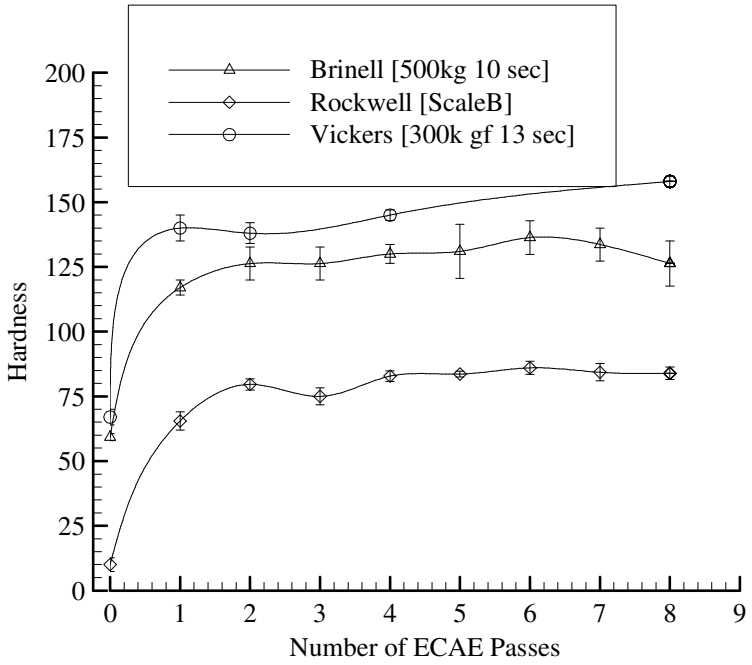

Figure 9. Work Hardening Tests on Reference Metals Company Material That Underwent ECAE.

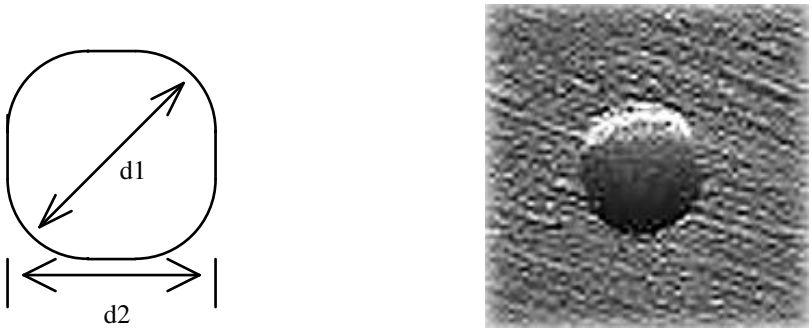

a) b)

Figure 10. a) Schematic of Typical Brinell Indention. b) Photo of Brinell Indention in As-Cast RMC Material.

C. Vickers Hardness as a Function of Annealing Temperature

Vickers hardness tests (300 g 13 sec) were performed on both the Reference Metals Company (RMC) and Wah Chang materials for various annealing temperatures. Hardness measurements were also performed on the as-received RMC and Wah Chang material. These tests proved useful in determining the recrystallization behavior as a function of ECAE route. Nine specimens approximately 0.8mm×0.8mm×0.8mm were cut from each billet and subjected to vacuum annealing. One specimen per billet was left as-worked while the other 8 specimens were annealed at 300^{o}C, 500^{o}C, 700^{o}C, 800^{o}C, 900^{o}C, 1000^{o}C, 1100^{o}C, 1200^{o}C for 1 hour under vacuum conditions. Specimens were then mounted in epoxy, with the flow plane exposed and polished prior to testing. A minimum of 5 hardness tests were performed on each specimen and averaged. Duplicate billets were averaged. Vickers hardness ($H_{V)}$ was observed as a function of annealing temperature (T_A) while keeping the route constant, $H_V = H_V(T_A)_{Route}$. Hardness graphs for the Reference Metals Company material are shown in Figure 11 and Figure 12. Hardness graphs for the Wah Chang material are shown in Figure 13.

1. Reference Metals Sample

The Vickers results show similarities and differences among the different ECAE routes for the Reference Metals Company material. Hardness values for all routes show a gradual increase followed by a sharp decrease and leveling off. Maximum hardness for all routes was reached at approximately 300^{o} C. This maximum hardness ranged from a low of 151 for route 1A to a high of 163 for route 8E indicating that the maximum hardness is an increasing function of strain. Note that the maximum hardness for routes 4E and 8E

are similar indicating hardness saturates at about 4 passes. The hardness then decreases rapidly until it levels off at approximately 70 for all routes. The difference lies in the leveling off temperature (recrystallization temperature). This recrystallization temperature ranges from a high of 1000° C for route 1A to a low of about 800° C for routes 2C, 4E and 8E indicating that the recrystallization temperature decreases with increasing strain.

Figure 11 shows the averaged-duplicate Vickers hardness results for the Reference Metals samples along with the standard deviation for each measurement. Because there were two billets that underwent route 1A, two billets that underwent route 2C and two billets that underwent route 4E, duplicate routes were averaged. Duplicate billets showed little difference for routes 2C, and 4E indicating that reproducibility improved with increasing strain. Route 1A did show significant differences. Differences lie in the maximum hardness values and the leveling-off nature of the two billets that underwent route 1A as shown in Figure 12.

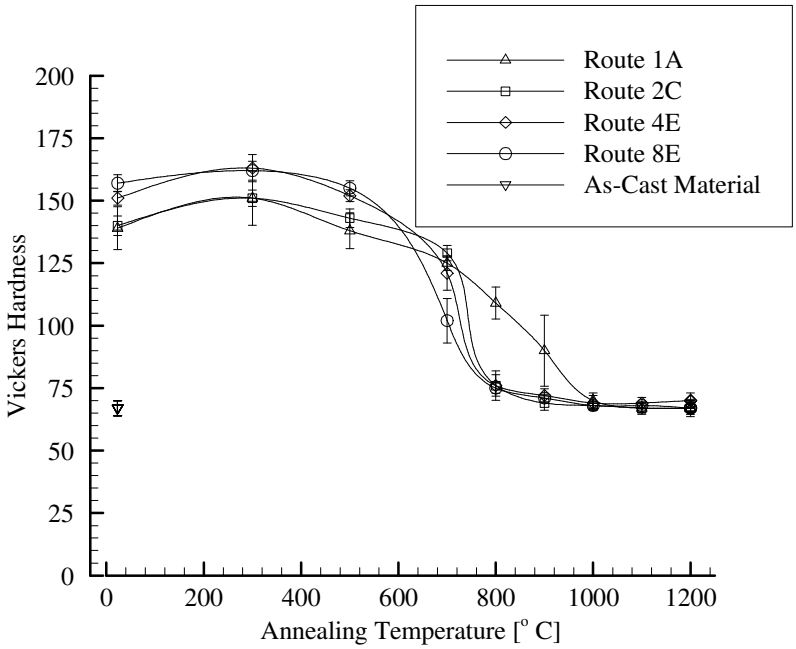

Figure 11. Vickers Hardness as a Function of Annealing Temperature for Reference Metals Company ECAE Processed Niobium.

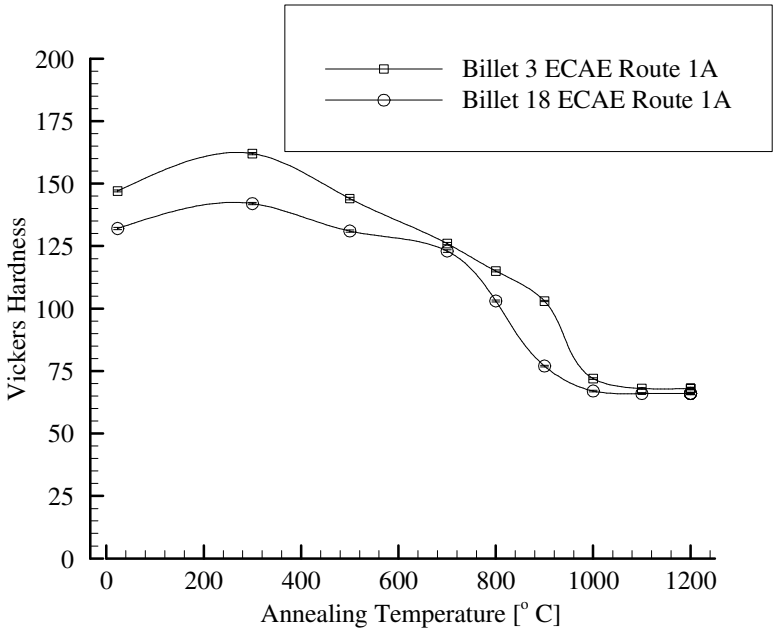

Figure 12. Vickers Hardness as a Function of Annealing Temperature for Reference Metals Company ECAE Processed Niobium Route 1A.

2. Wah Chang Sample

These Vickers results show significant differences between the as-received and the ECAE/4E processed Wah Chang material. The hardness of the as-received material increases to maximum of 143.5 and the hardness of the ECAE processed material increases to a maximum of 157.3. This maximum is reached at an annealing temperature of 500° C for the as-received materials and at 300° C for the ECAE processed material. Both decrease after reaching the maximum and level off to approximately 70. The as-received material levels off at 900° C and the ECAE processed material levels off at 800° C. Figure 13 shows the Vickers hardness results for both as-received and the ECAE /4E processed Wah Chang material along with the standard deviations for each specimen. Note that the as-received material with no annealing has a significantly higher value than that of the RMC as-received material. This indicates that the as-received Wah Chang material was previously worked.

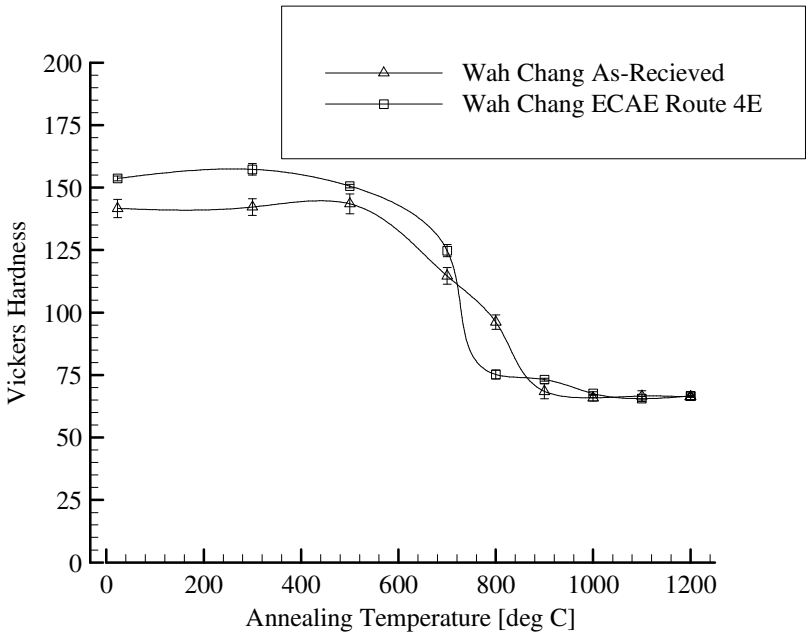

Figure 13. Vickers Hardness as a Function of Annealing Temperature for Wah Chang Niobium.

D. Deformation Banding Observations in As-Worked Materials

When a billet undergoes ECAE, it undergoes shear strain which can be represented by engraving a grid into the billet prior to extrusion and observing the distorted grid after the extrusion. Figure 14 shows a typical pattern consisting of two parallel lines engraved into the side of a billet before extrusion. This pattern suggests the development of simple shear after 1 pass via ECAE. The parallel lines tilt approximately 26^{o} and become closer together after the shear zone. This suggests that deformation banding can occur depending on crystal orientation. In order to investigate this phenomenon, the as-worked samples were acid etched and observed for deformation banding by optical microscopy.

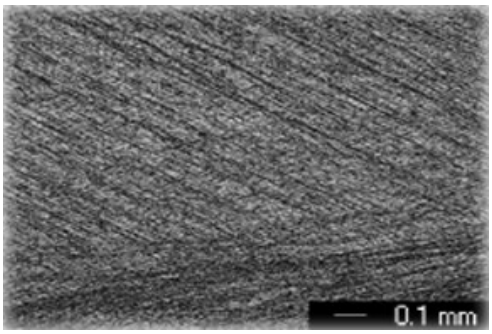

Figure 14. Simple Shear Caused by 1 Pass ECAE.

1. Reference Metals

A total of 16 micrographs (4×4matrix) magnified at 5x each were taken for each as-worked specimen (after acid etching) to produce a panoramic view for each specimen as shown in Figures 15, 16, 17, 18, 19, 20 and 21. Deformation banding is evident in all samples and the morphology varies within individual samples, between duplicate routes and for different routes. Some of the bands are straight while others are curved. One pass results in the straightest bands while curved bands appear in two or more passes. Banding also appears more complex, dense and fine with increasing strain. The difference in band morphology between duplicate billets appears to diminish with increasing strain. Banding in both 4E samples appears more complex than that of lower strained samples. There also appears to be a close resemblance between samples that underwent 4E and 8E processing.

Figures 15 and 16 show micrographs of samples that were subjected to ECAE route 1A (billet 3 and billet 18). Sample 3-1 shows significantly more banding than that of sample 18-1. The angle of the bands on both samples is larger at the upper edge. Note from Figure 4 that this edge (sample ID 1) is adjacent to the edge of the die wall. Although both billets were shimmed with brass, the deformation banding indicates that there are effects caused by the die edge. Sample 3-1 shows more activated slip systems than that of sample 18-1. Both show a decrease in deformation bands further from the upper edge.

Figures 17 and 18 show micrographs of samples that were subjected to ECAE route 2C (billet 17 and billet 24). Bands in sample 17-1 are angled while band in sample 24-1 are more plate like in the horizontal direction. Deformation bands for both samples are horizontal near the upper edge indicating the billets are sticking near the die wall.

Figures 19, 20 and 21 show micrographs of samples from billets that were subjected to ECAE routes 4E (billets 19 and 2) and 8E (billet 4). Deformation banding in samples 19-1 (4E) and 4-1 (8E) are similar. Note that samples 2-1 (4E) and 19-1 (4E) show differences in banding morphology. Although duplication of deformation banding improves with increasing strain, differences still occur.

Top of Sample

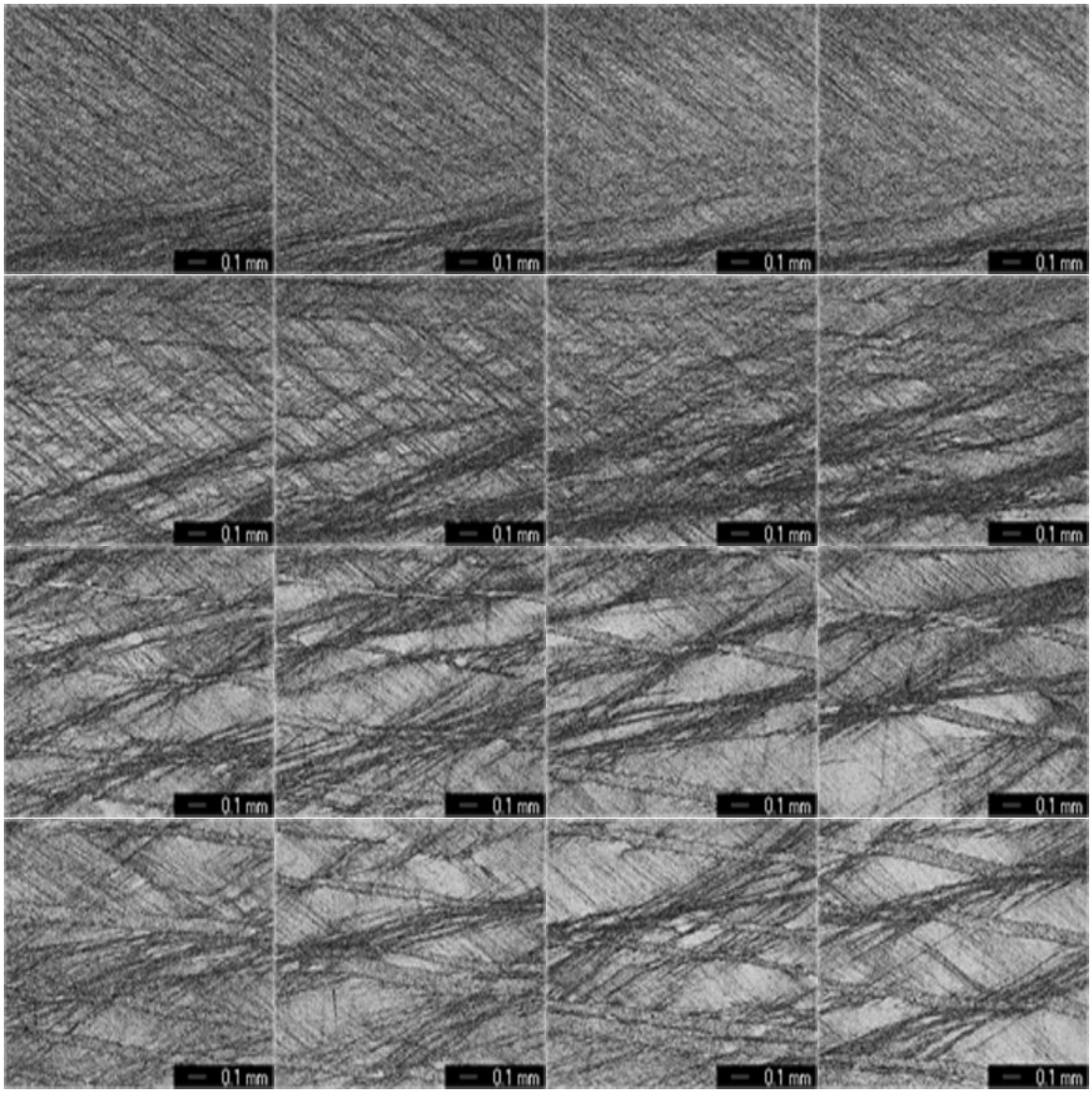

Figure 15. Panoramic View of Sample 3-1; ECAE 1A/No Annealing.

Top of Sample

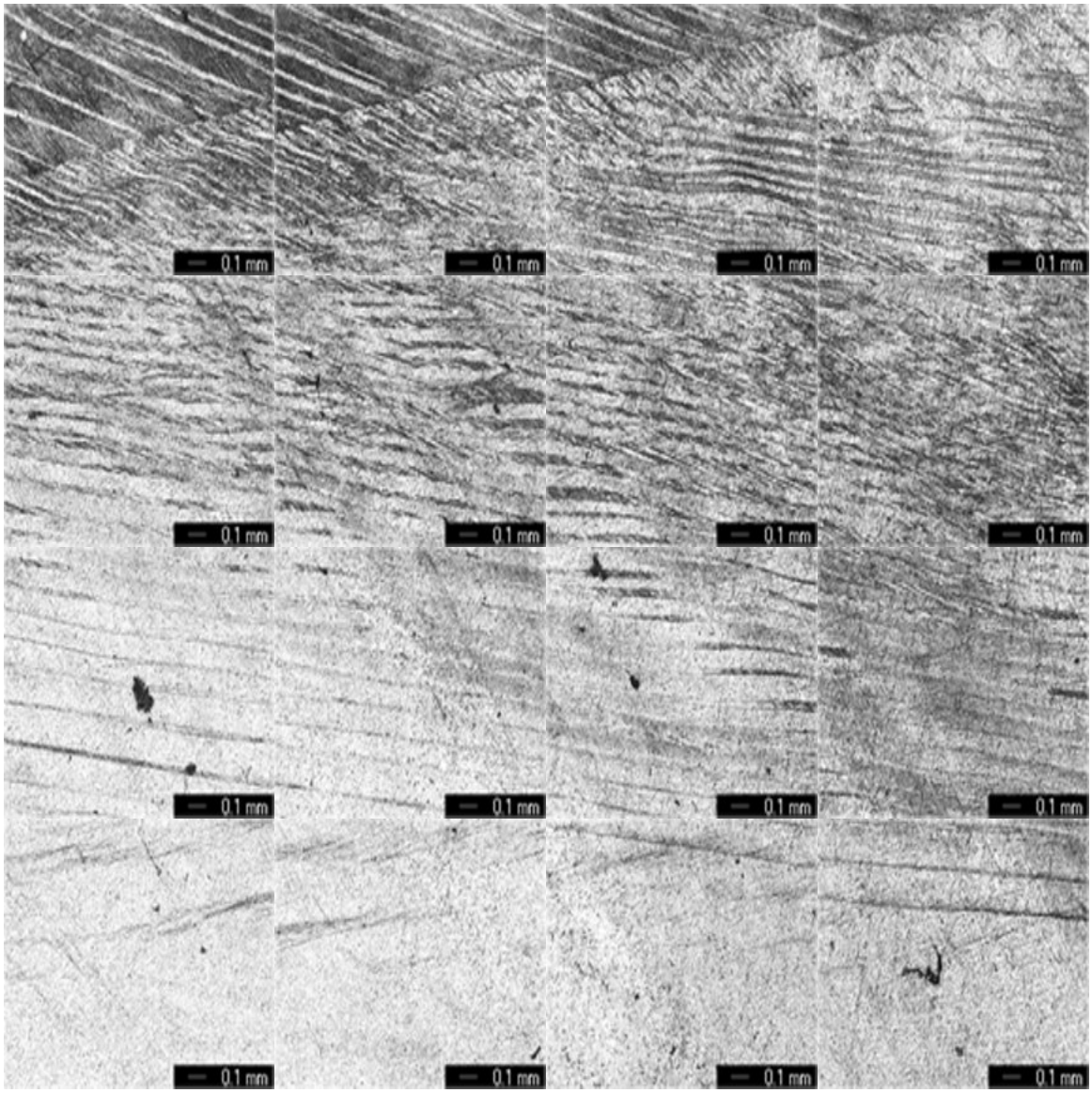

Figure 16. Panoramic View of Sample 18-1; ECAE 1A/No Annealing.

Top of Sample

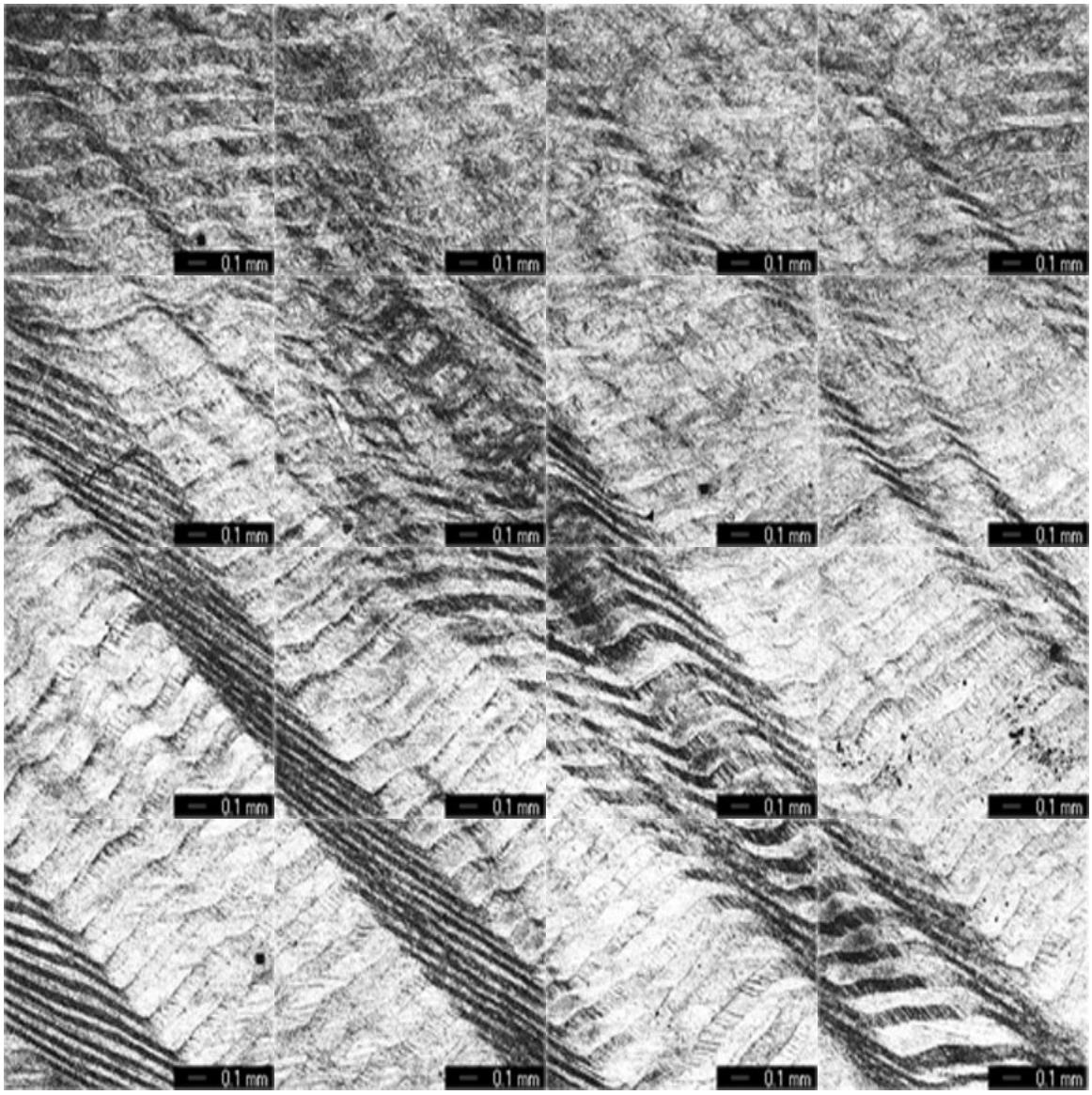

Figure 17. Panoramic View of Sample 17-1; ECAE 2C/No Annealing.

Top of Sample

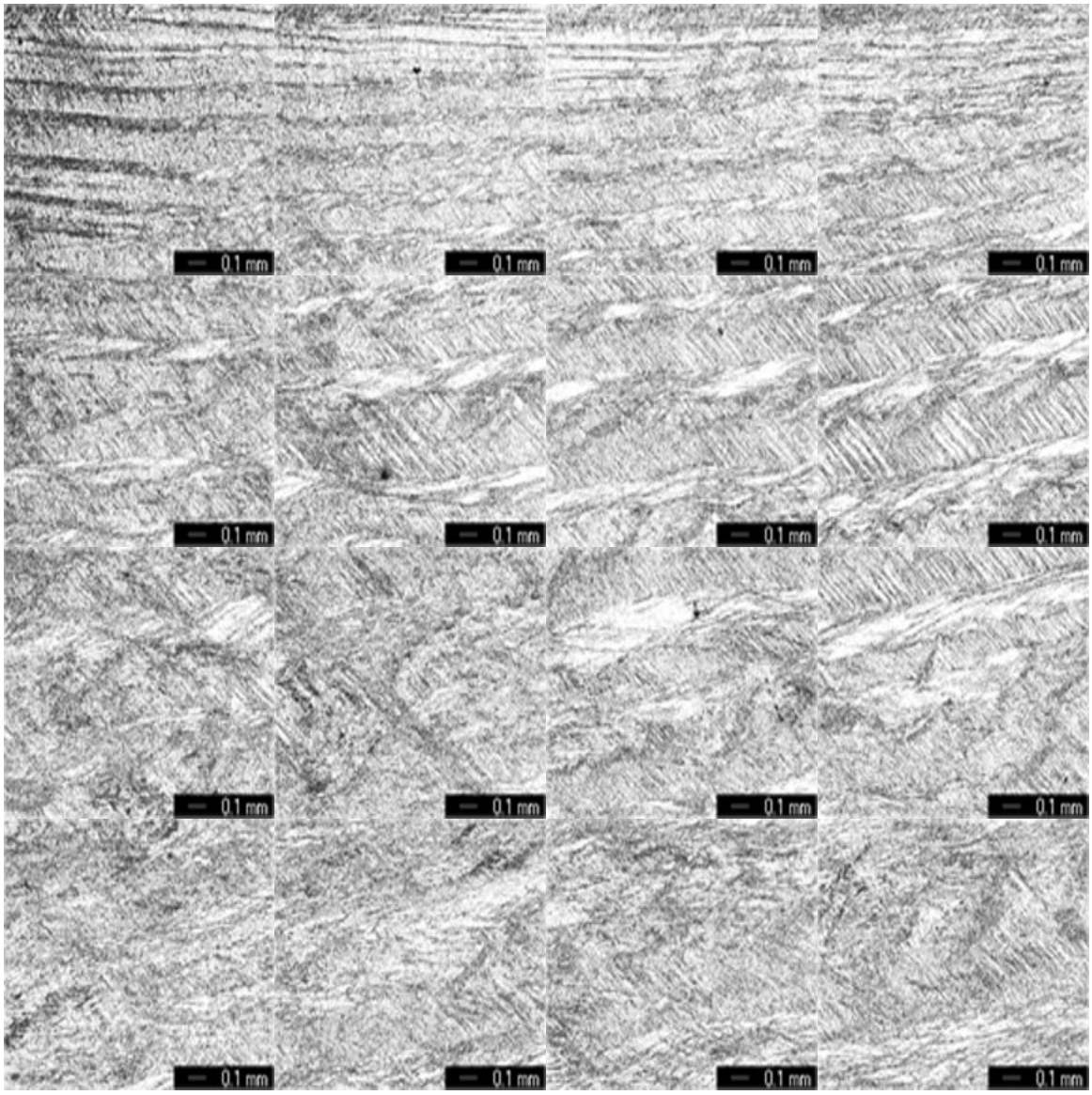

Figure 18. Panoramic View of Sample 24-1; ECAE 2C/No Annealing.

Top of Sample

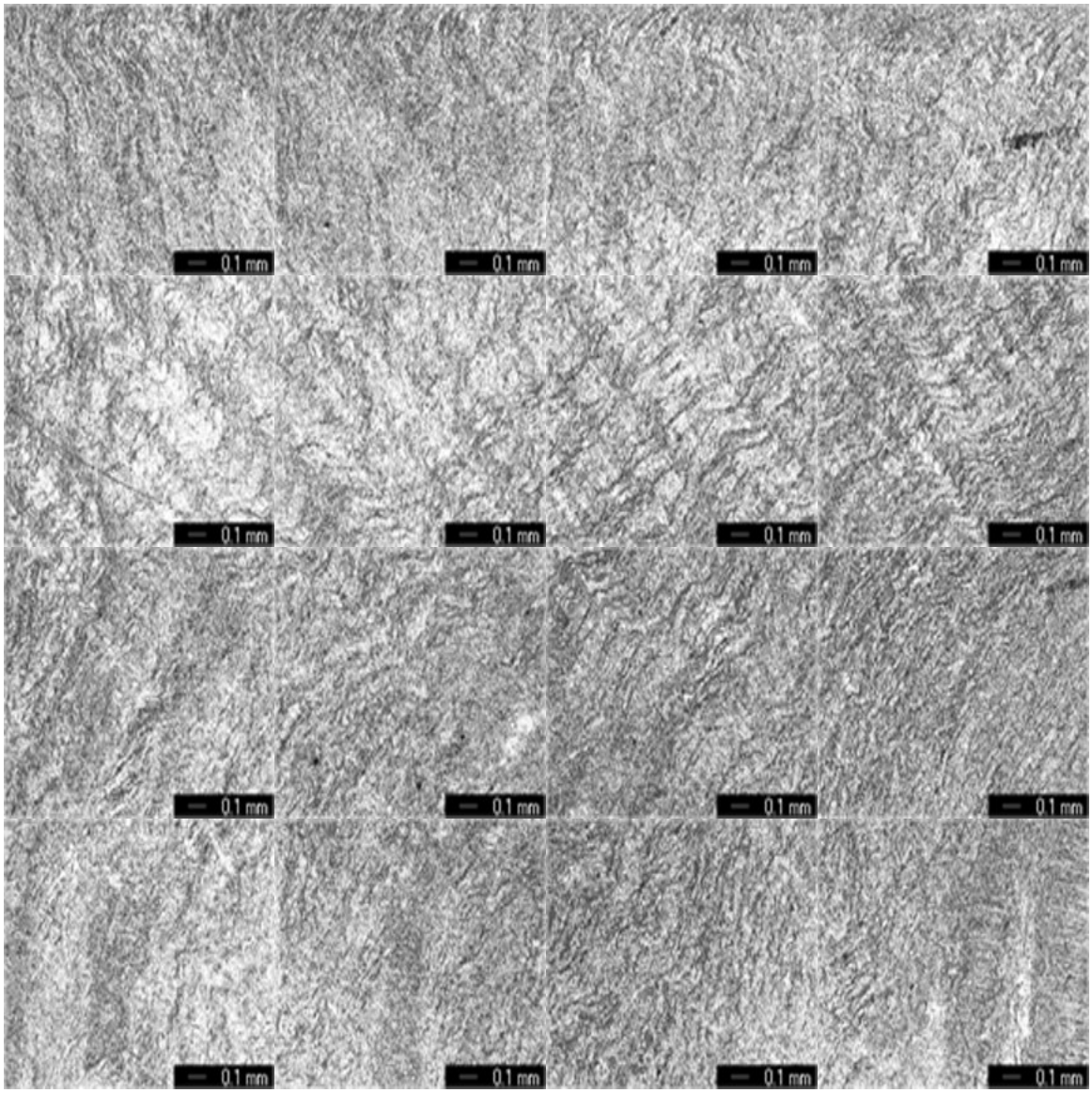

Figure 19. Panoramic View of Sample 2-1; ECAE 4E/No Annealing.

Top of Sample

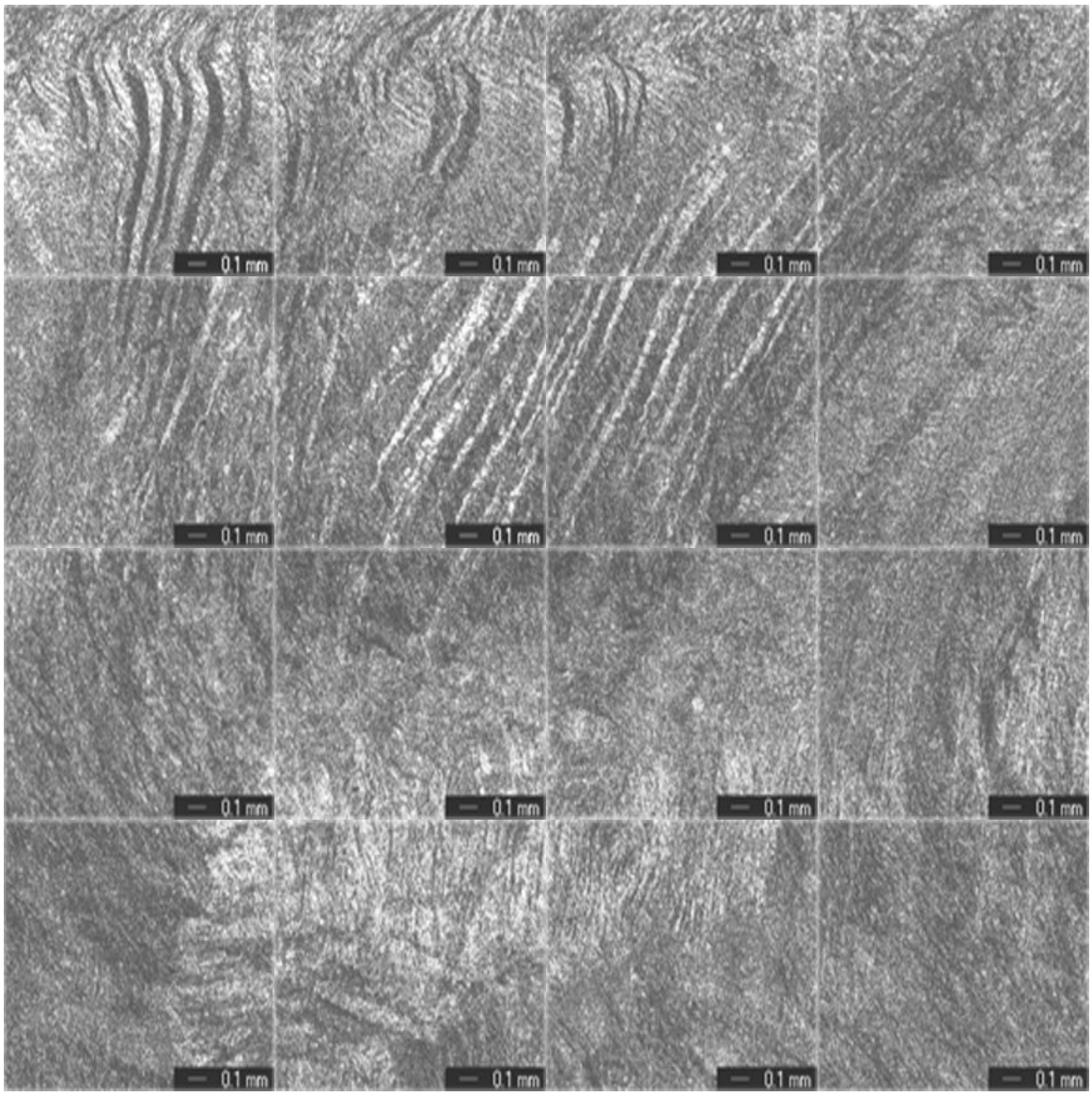

Figure 20. Panoramic View of Sample 19-1; ECAE 4E/No Annealing.

Top of Sample

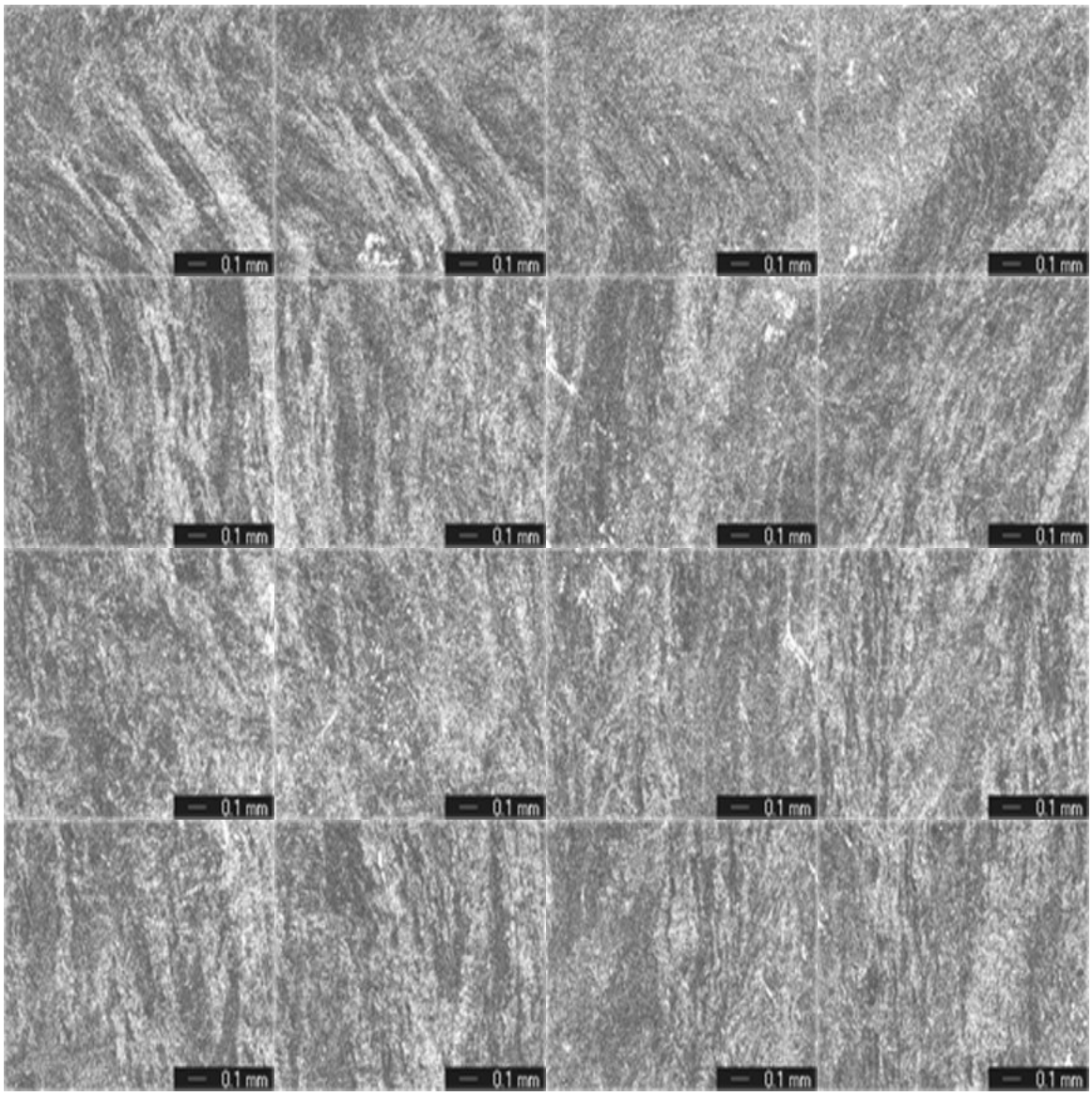

Figure 21. Panoramic View of Sample 4-1; ECAE 8E/No Annealing.

2. Wah Chang

The purpose of this section is to report the presence or not of deformation banding in the Wah Chang as-received rod and a section of the rod that underwent ECAE route 4E. The orientation mapping of the as-received rod is shown in Figure 22 using cylindrical coordinates. The z-direction is associated with the longitudinal direction and the θ-plane is associated with the optically observed plane. Deformation banding in the as-received material shows banding in the longitudinal direction and on the θ-plane as shown in Figure 23. Figure 24 is a close-up view of the as-received sample clearly showing deformation bands in the longitudinal direction. This suggests that the rod underwent area reduction (probably swaging) thereby forming deformation bands in the z-direction. After ECAE route 4E, the deformation banding is eliminated as shown in Figure 25. Figure 26 shows a close-up view the ECAE/4E processed Wah Chang material clearly showing that ECAE produces a more homogenized deformation banding structure. It should be noted that prior to ECAE, the rod was annealed at 900^{o} C thereby causing partial recrystallization as shown in Figure 27.

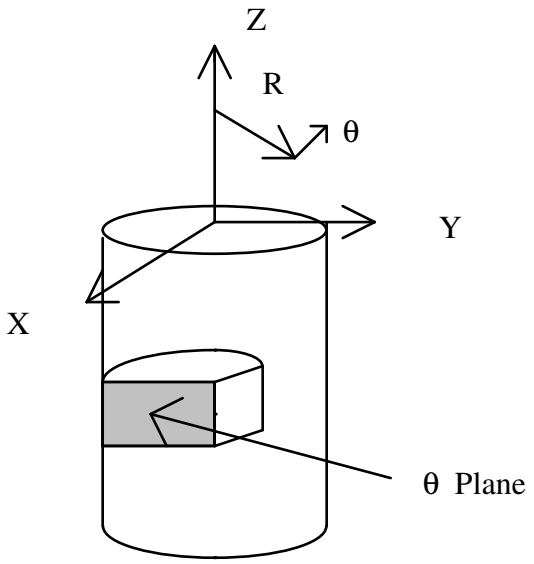

Figure 22. Orientation of Specimen With Respect to Wah Chang Rod.

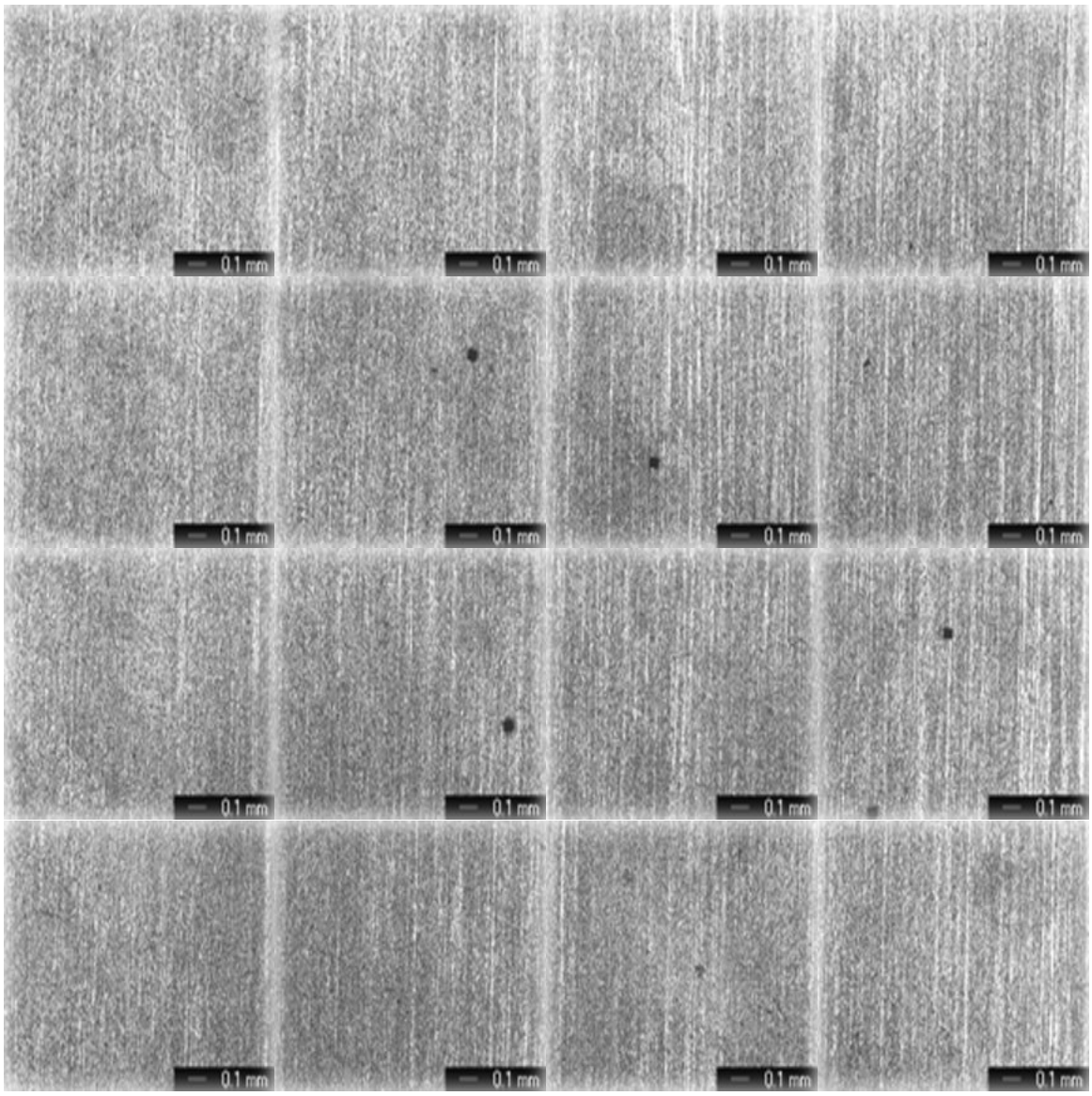

Figure 23. Panoramic View of Sample WC-1; As-Received/No Annealing.

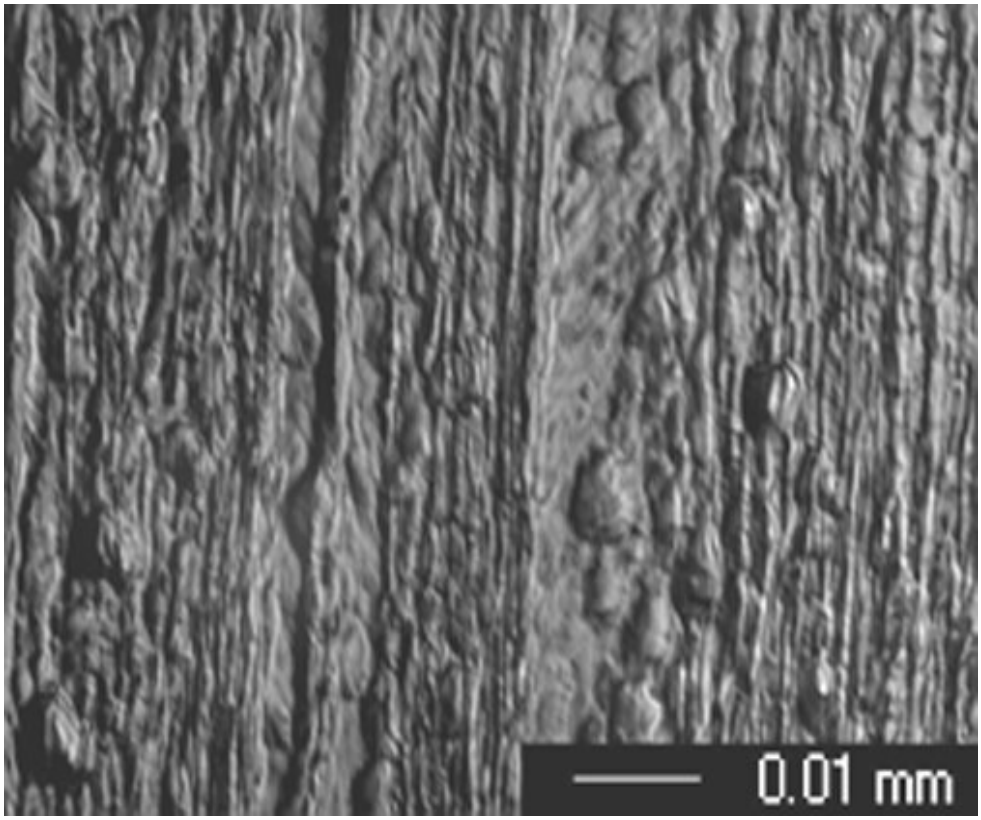

Figure 24. Close Up Micrograph of Wah Chang Nb; As-Received/No Annealing.

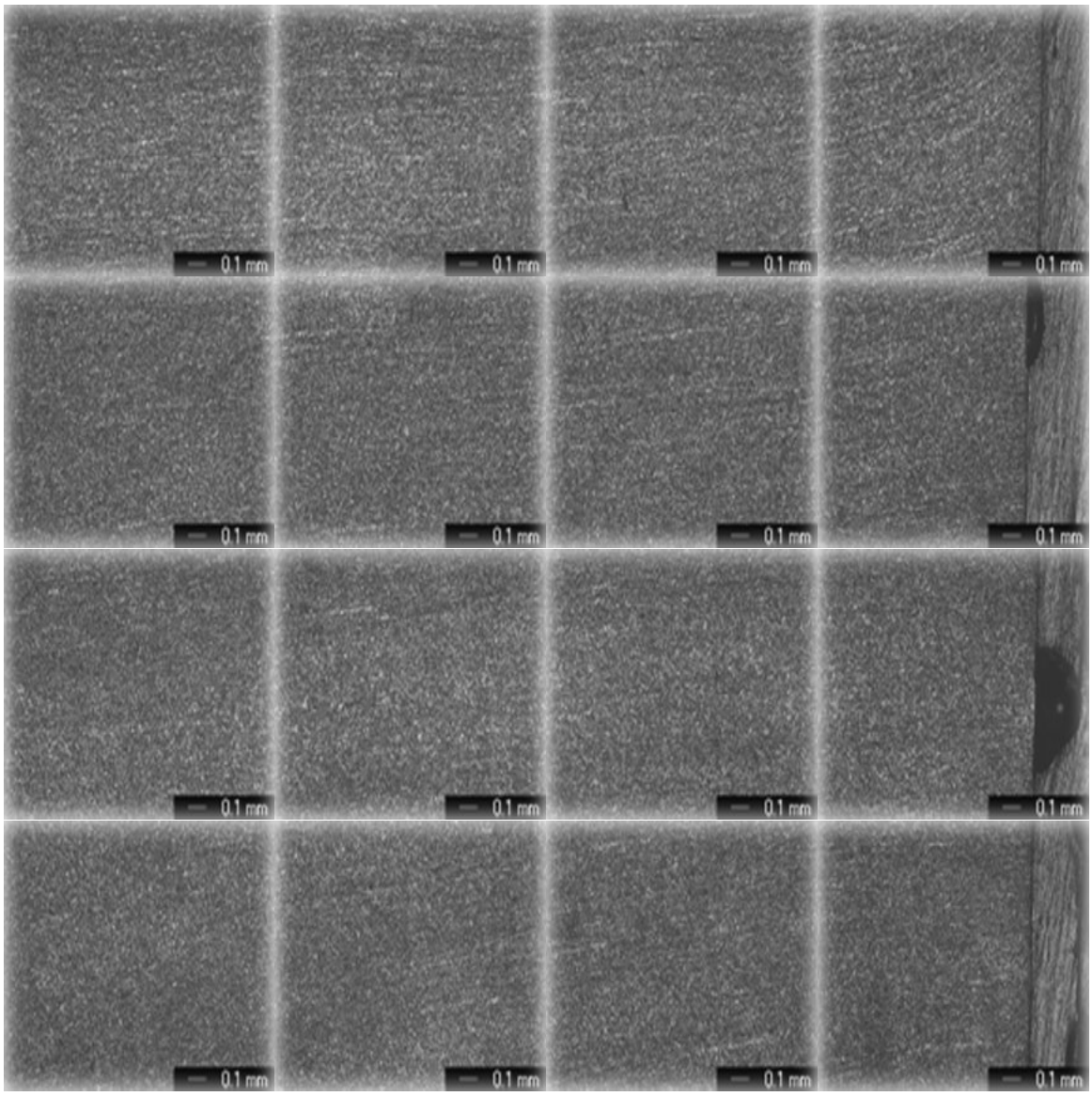

Figure 25. Panoramic View of ECAE Processed Wah Chang Niobium; Sample W2-1 ECAE 4E/No Annealing.

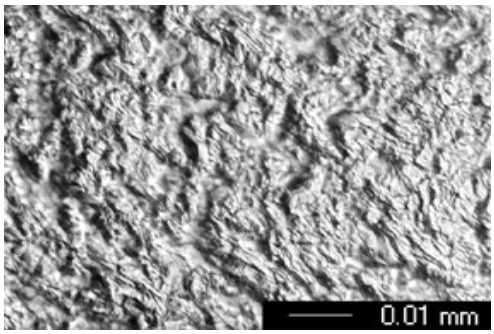

Figure 26. Close Up Micrograph of ECAE Processed Wah Chang Nb; ECAE 4E/No Annealing.

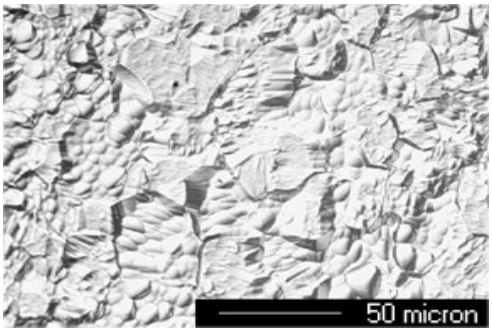

Figure 27. As-Received Wah Chang Material Annealed at 900^{o} C; Micrograph of Sample ID WC_900C_40xA.

E. Optical Microscopy of Reference Metals and Wah Chang ECAE Processed Material Annealed at 1100^{o} C

In order to examine the recrystallized microstructure as a function of ECAE route, it was necessary to look at all specimens at a common annealing temperature. Since all samples were fully recrystallized at 1100^{o} C, this temperature was chosen. Because all samples annealed at 1100^{o} C are approximately 7 mm by 7mm, panoramic micrographs were taken for each sample thereby covering most of the full sample cross-section.

1. Reference Metals Samples

A total of 16 micrographs (4×4) magnified at 5x each were taken for each of the ECAE processed Reference Metals specimens annealed at 1100^{o} C to produce a panoramic view of each specimen as shown in Figures 28, 29, 30 , 31, 32, 33 and 34. Optical microscopy shows the effectiveness of ECAE to break up large grained niobium to be a function of route (strain) and original grain orientation. Although samples subjected to duplicate routes did not produce similar grain morphologies, reproducibility of the microstructure does improve with increasing strain. Irreproducibility was most pronounced in the duplicate samples that under went 1 pass. The average grain diameter for duplicate samples 3-8 (ECAE 1A/1100^{o} C annealing) 18-8 (ECAE 1A/1100^{o} C annealing) was the largest of the processed/1100^{o} C annealed samples. The average grain diameter decreased from the as-cast material to the 4E processed material but increased in the 8E sample. Furthermore, banding was not consistent. The average grain diameter for sample 4-8 (ECAE 4E/1100^{o} C annealing) is larger than that of samples 2-8 (ECAE 4E/1100^{o} C annealing) and 19-8 (ECAE 4E/1100^{o} C annealing).

Duplicate samples that underwent route 1A (billets 3 and 18) show the most significant differences in grain morphology a shown in Figures 28 and 29. Note that grain refinement of billet 3 (banding present) is significantly finer than that of billet 18. Furthermore, sample 3-7 has a banding morphology while sample 18-7 (no banding) does not. A finer grain structure in sample 3-7 is expected since sample 3-1 shows more activated slip systems as shown in the as worked micrograph. This is due to a more favorable original grain orientation prior to extrusion.

Duplicate samples that underwent route 2C (billets 17 and 24) show improvement over route 1A yet differences still exists as shown in Figures 30 and 31. The grain size of sample 17-8 (banding present) is slightly smaller than that of sample 24-8 (no banding). Furthermore sample 17-8 shows banding while sample 24-8 has a more homogeneous microstructure. The banding in sample 17-8 is expected because the as-worked micrographs show banding.

Although duplicate samples that underwent route 4E (billets 2 and 19) show the least differences in grain morphology as shown in Figures 32 and 33, differences still exists. The average grain diameter of sample 2-8 (banding present) is smaller than that of sample 19-8 (no banding).

Sample 4 which underwent route 8E (billet 4) is shown in Figure 34. The average grain diameter of sample 4-8 (banding present) is larger than that of samples 2-8 and 19-8. Note significant banding.

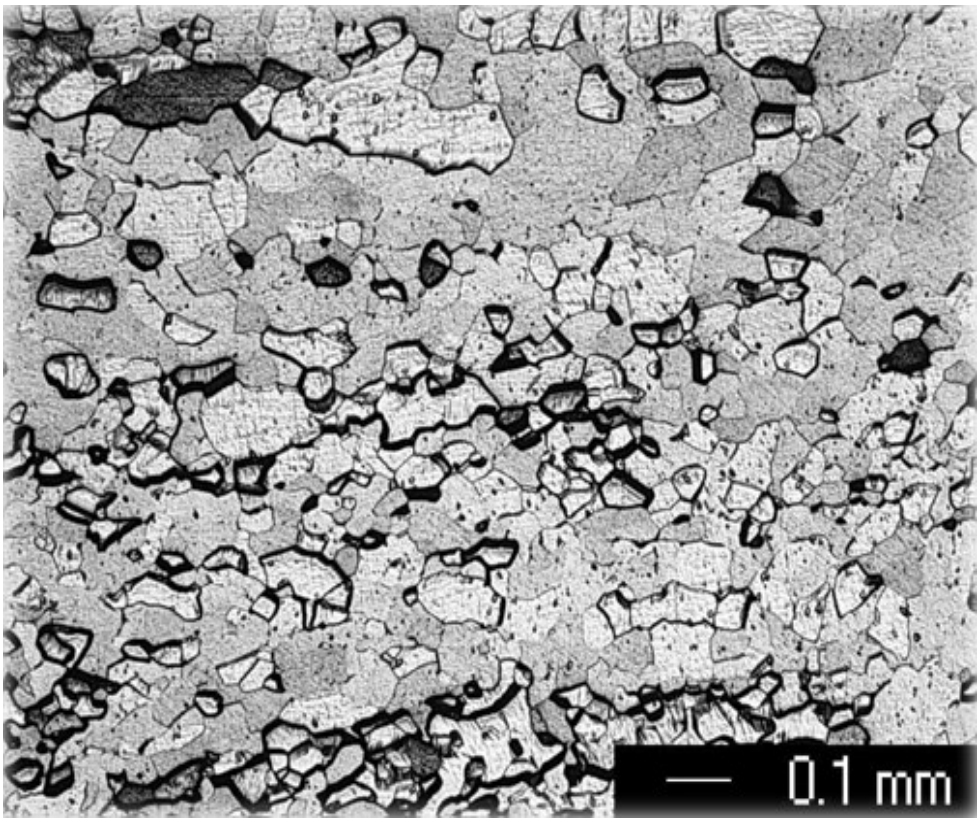

Figure 28. Section View of Sample 3-8 ECAE/1A Processed Pure Nb Annealed at 1100^{o}C.

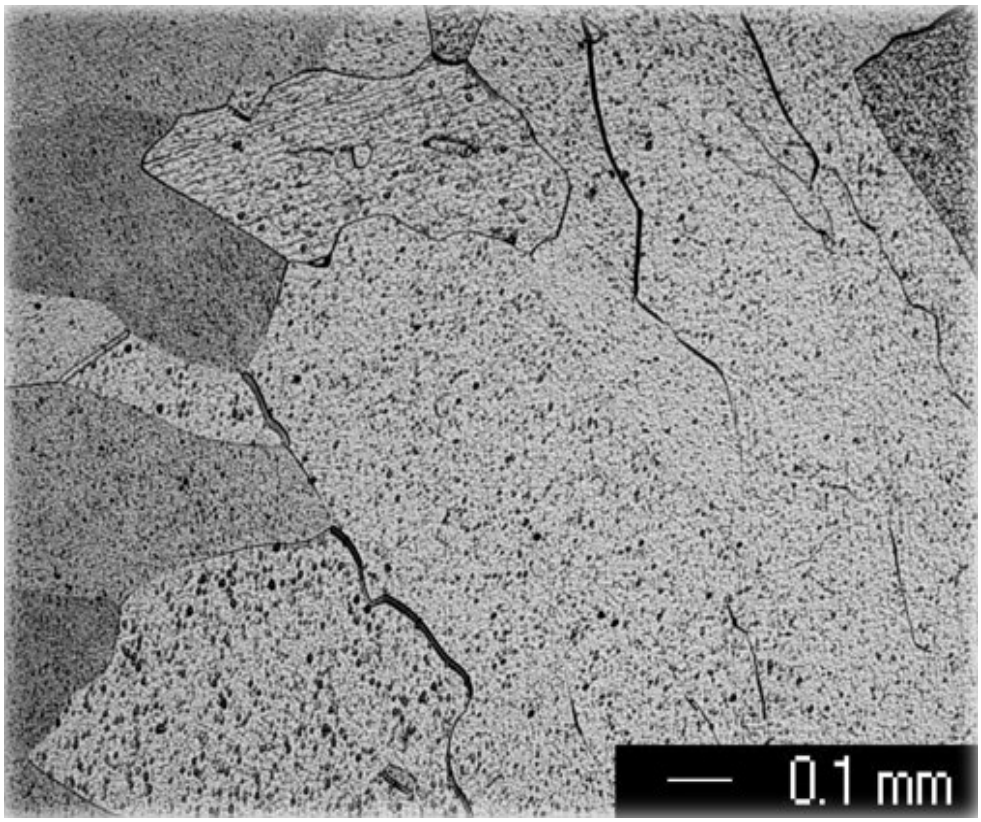

Figure 29. Section view of Sample 18-8 ECAE/1A Processed Pure Nb Annealed at 1100^{o}C.

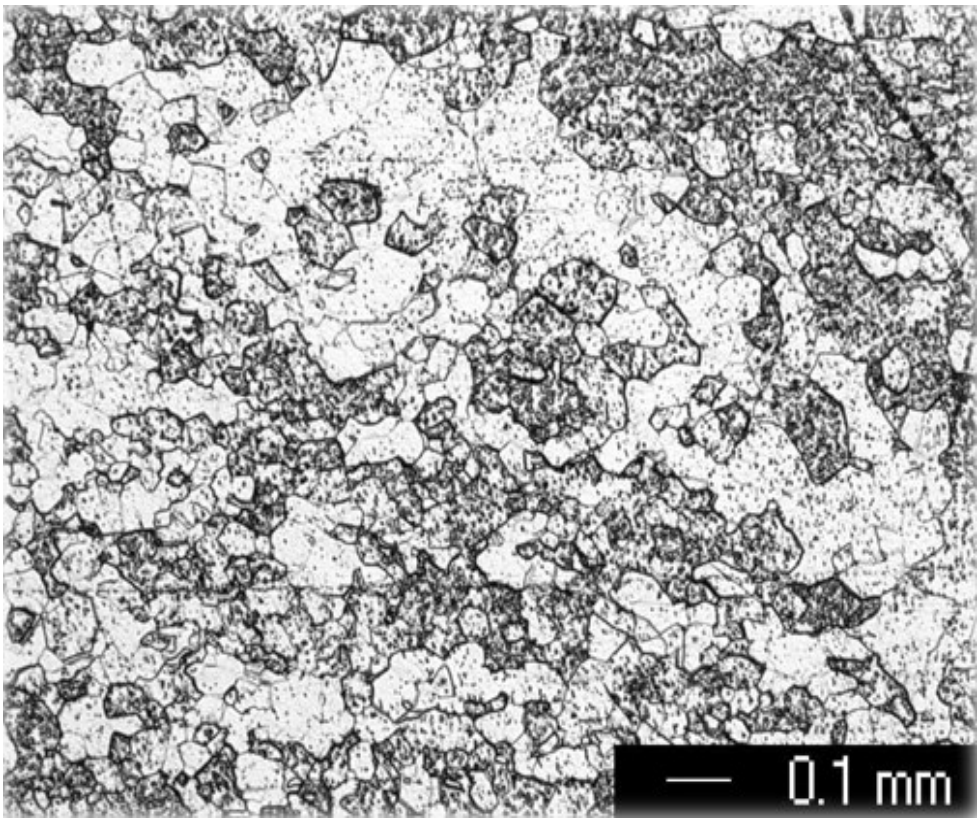

Figure 30. Section View of Sample 17-8 ECAE/2C Processed Pure Nb Annealed at 1100^{o}C.

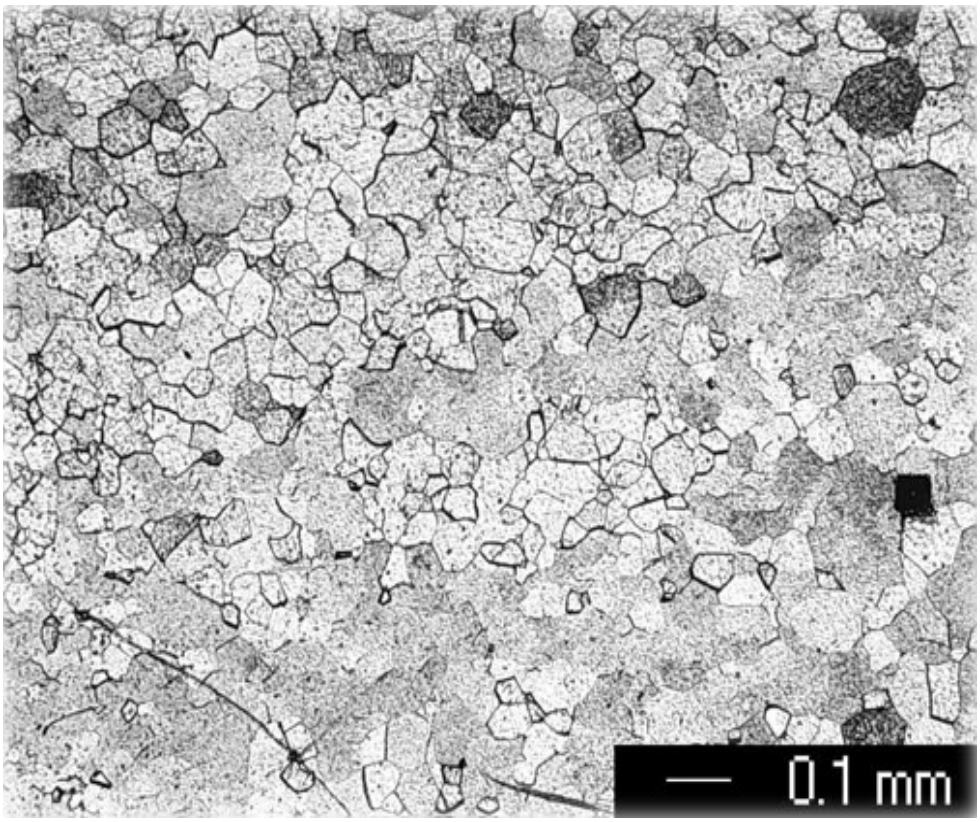

Figure 31. Section View of Sample 24-8 ECAE/2C Processed Pure Nb Annealed at 1100^{o}C.

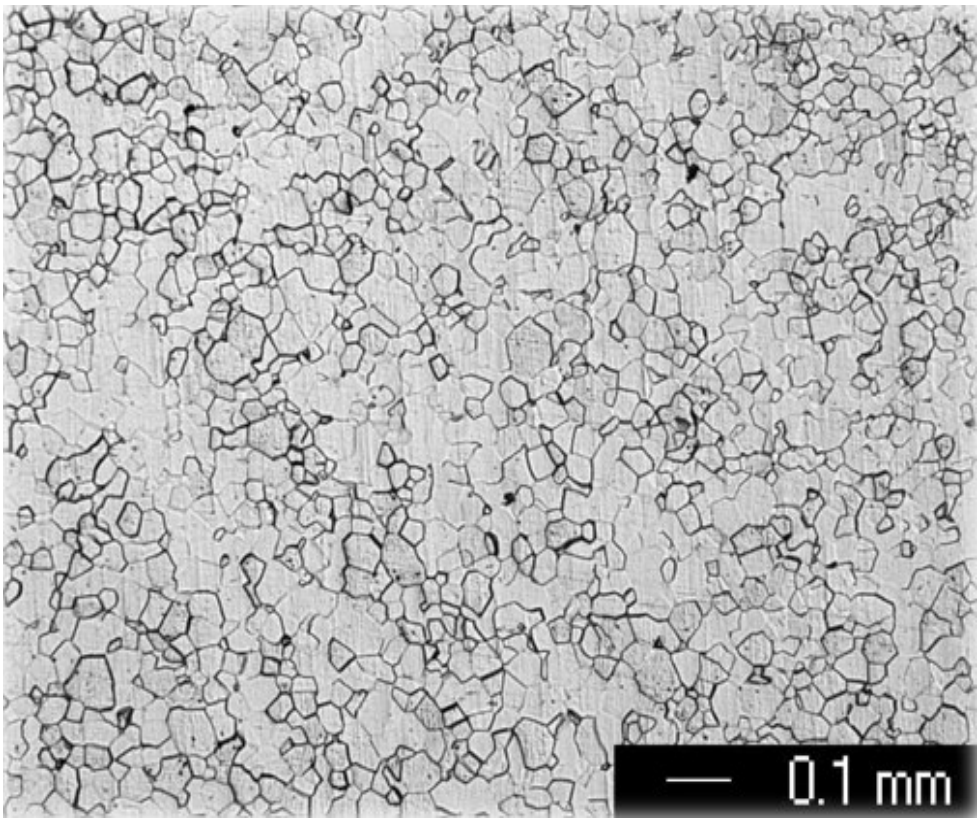

Figure 32. Section View of Sample 2-8 ECAE/4E Processed Pure Nb Annealed at 1100^{o}C.

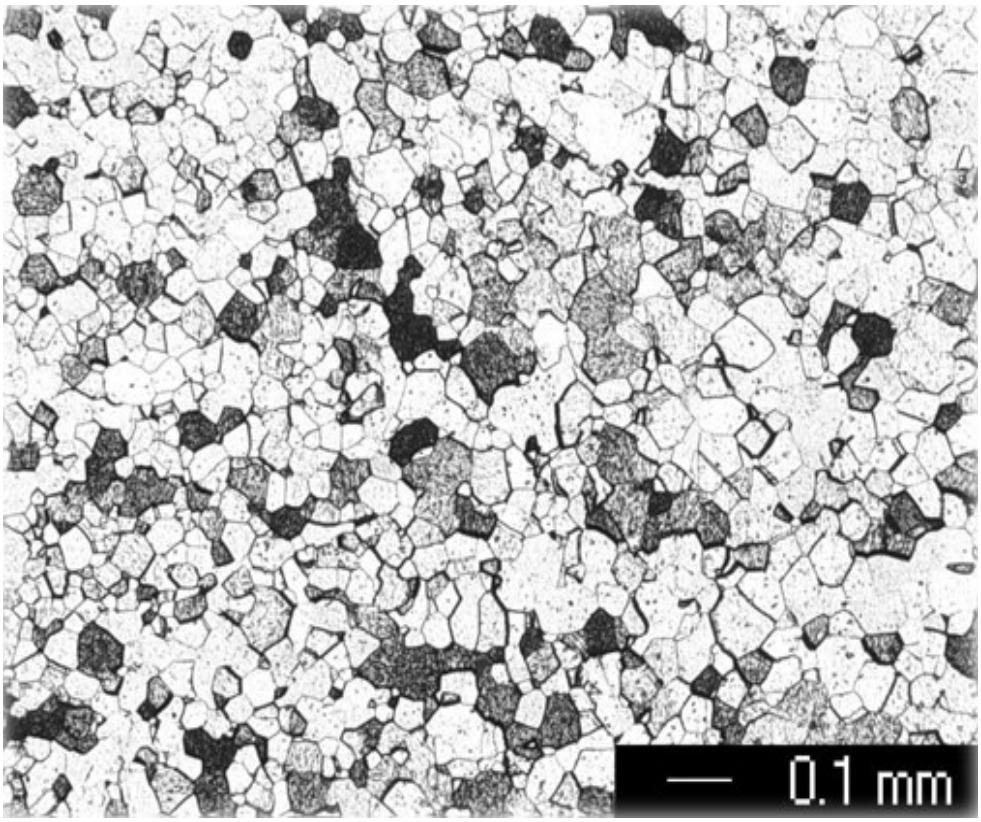

Figure 33. Section View of Sample 19-8 ECAE/4E Processed Pure Nb Annealed at 1100^{o}C.

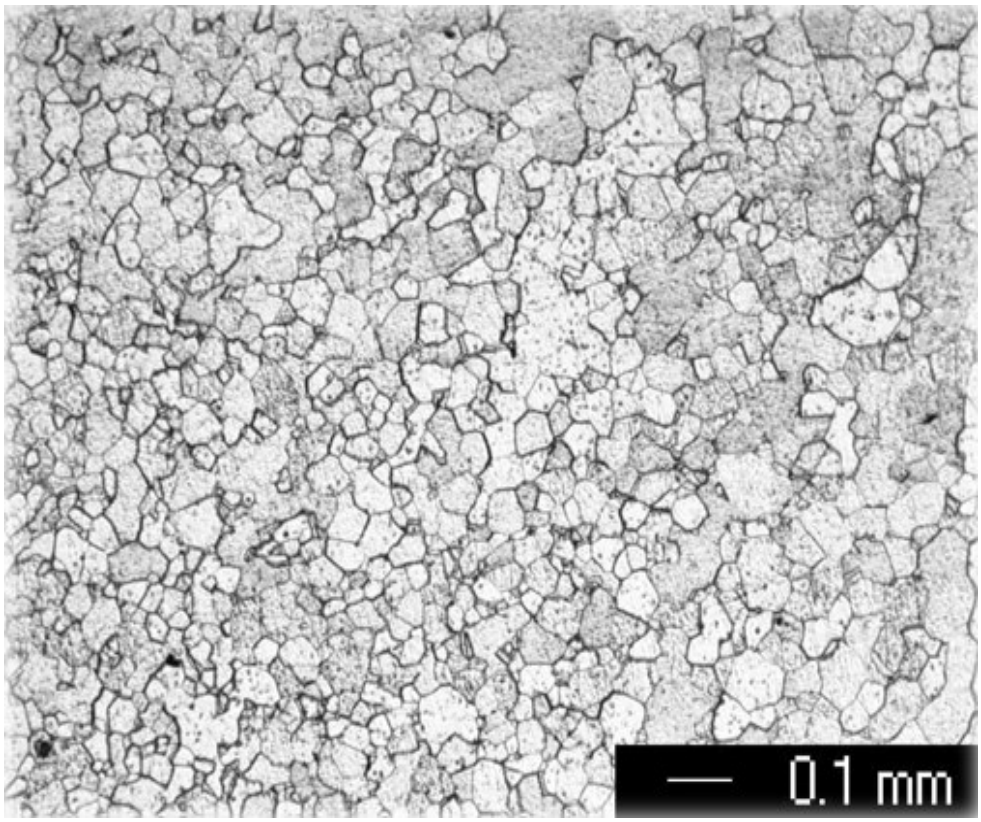

Figure 34. Section View of Sample 4-8 ECAE/8E Processed Pure Nb Annealed at 1100°C.

2. Wah Chang Samples

A total of 16 micrographs (4×4) magnified at 5x each were taken for the Wah Chang ECAE/4E processed specimen and 12 were taken for the Wah Chang as-received specimen to produce panoramic views for each specimen. Figure 35 shows that crystal banding in the longitudinal direction was developed in the 1100^{o} C annealed Wah Chang as-received sample. Figure 36 shows that the microstructure loses its banding morphology after EACE/4E yet the grain morphology is still not homogenized.

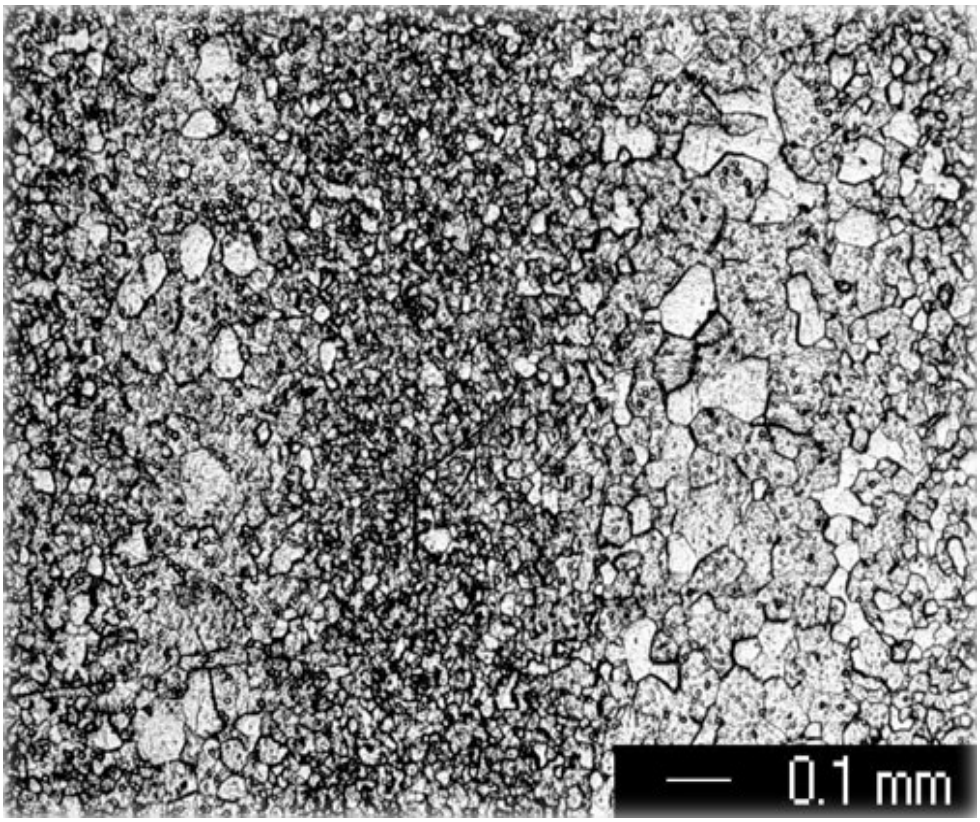

Figure 35. SectionView of Wah Chang As-Received Material Annealed at 1100^{o} C.

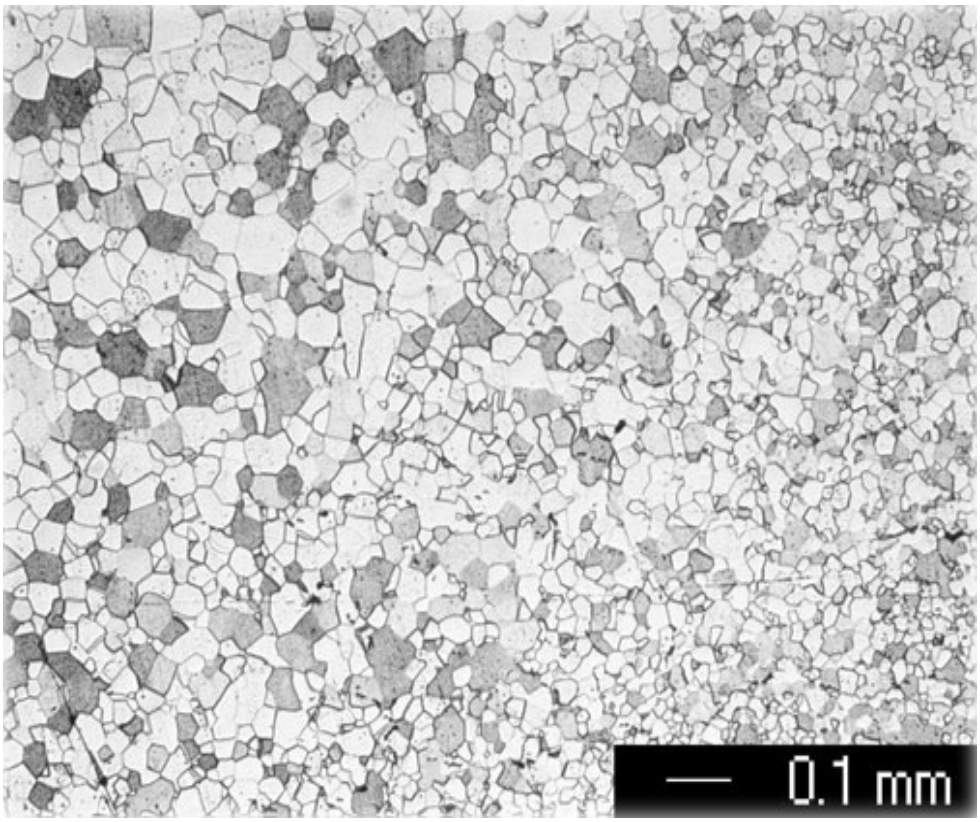

Figure 36. Section View of Wah Chang ECAE/4E Processed Material Annealed at 1100^{o} C.

F. Grain Size Calculations of Reference Metals 4E and 8E ECAE Processed Material Annealed at 1000^{o} C and 1100^{o} C

Because routes 4E and 8E proved to be the most promising ECAE processing methods in this research, a more quantitative analysis was performed. Average grain diameters and grain diameter distributions were calculated for the 1000^{o} C and 1100^{o} C annealed samples. Furthermore, banding morphology was considered.

Routes 4E and 8E processed material begin to show signs of recrystallization at the 800^{o} C annealed state as shown in Figure 37. Because the worked material is fully recrystallized at 1000^{o} C this was the starting point of the quantitative analyses. The methodology for the grain size calculations is as follows. Because each annealed sample is approximately 7mm×7mm, a total of 16 panoramic micrographs (4×4) at 5x magnification were taken for each sample covering a majority of each specimen. A representative micrograph was then taken for each of the panoramic micrographs and analyzed for grain sizes utilizing IPTK. Average grain size, standard deviation and grain size distribution calculations were calculated two different ways: panoramic and spatial. The panoramic calculations took into account the total number of grains measured. For example, specimen 2-7 involved calculating the grain diameters of 1194 grains and then taking the average (27.5 μm) along with the standard deviation (11.6). Note that the panoramic calculations are not a measurement of the spatial distribution because all grain measurements are clumped into one formula. Grain size distribution graphs were divided into 1 μm intervals. The spatial calculations took into account the average of each of the representative micrographs. For example, specimen 2-7 involved calculating the average of each of the 16 representative micrographs. These 16 averages were then averaged (28.2 μm) along with the standard deviation (4.9). Note that the spatial standard deviation is a way to quantify the spatial distribution. Figures 38, 39, 40, 41, 42, 43, 44, 45, 46, 48 and 49 show panoramic micrographs and representative micrographs of samples 2-7 (route 4E), 19-7 (route 4E) and 4-7 (route 8E) annealed at 1000^{o} C and 1100^{o} C.

Recrysallization grain morphologies of routes 4E and 8E annealed at 1000^{o} C and 1100^{o} C are not consistent. Banding was present in approximately half of the samples. Differences varied among billets of duplicate routes and average grain sizes did not always increase with increasing annealing temperature. Some samples show banding while others are more homogeneous. Billet 2 (4E) shows banding in both the 1000^{o} C and 1100^{o} annealing states as shown in Figures 38 and 44. Billet 19 (4E) shows slight banding in the 1000^{o} C state and slight banding in the 1100^{o} state as shown in Figures 40 and 46. Billet 4 (8E) shows no banding in the 1000^{o} C state yet pronounced banding in the 1100^{o} state as shown in Figures 42 and 48. Although the average grain size did not always increase with increasing annealing temperature, the grain size distribution graphs widened with increasing annealing temperature. Figures 50, 51, 52, 53, 54 and 55 show the average grain diameters for each of the representative micrographs and the distributions.

Average panoramic grain diameters [μm] and average spatial grain diameters [μm] were taken for samples that underwent routes 4E and 8E annealed at 1000^{o} C and 1100^{o} C as shown in Figures 56 and 57. Average grain diameters did not always increase with increasing annealing temperature. The average grain sizes decreased from the 1000^{o} C state to the 1100^{o} state for billets 2 and 4. The average grain sizes for billet 19 show a significant increase from the 1000^{o} C state to the 1100^{o} state. Route 4E samples annealed at 1000^{o} C resulted in an average grain diameter of 27.5 ± 10.6 μm for billet 2 (banding was present) and an average grain diameter of 31.7 ± 12.9 μm for billet 19 (slight banding). Route 8E (banding was not present) annealed at 1000^{o} C resulted in an average grain diameter of 35.8 ± 13.5 μm. Route 4E samples annealed at 1100^{o} C resulted in an average grain diameter of 25.9 ± 12.9 μm for billet 2 (banding was present) and an average grain diameter of 42.2 ± 19.8 μm for billet 19 (slight banding). Route 8E (banding was present) annealed at 1100^{o} C resulted in an average grain diameter of 29.3 ± 15.1 μm. In an attempt to quantitatively analyze banding, the averages for each of the representative samples were averaged along with the standard deviation as shown in Figure 24. Billets 19 (4E) and 2 (8E) show a relatively large change in the spatial standard deviation from the 1000^{o} state to the 1100^{o} state while billet 2 shows a smaller change. Larger changes in spatial standard deviations can be attributed to banding. The spatial standard deviations in the 1000^{o} C annealed state is 4.9 for billet 2 (4E/ Banding was present), 3.3 for billet 19 (4E/slight banding) and is 2.1 for billet 4 (8E/Banding was not present). The spatial standard deviations in the 1100^{o} C annealed state is 7.1 for billet 2 (4E/Banding was present), 11.8 for billet 19 (4E/slight banding) and is 11.0 for billet 4 (8E/Banding was present). Tables 8 and 9 summarize the average grain diameters along with the standard deviations for both the panoramic and spatial calculations.

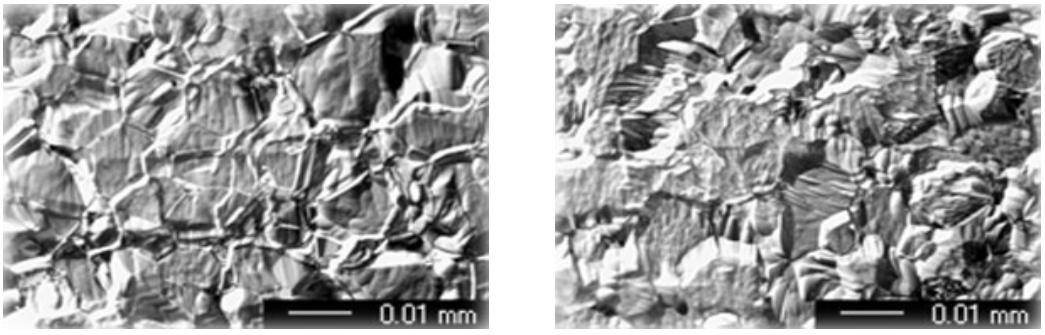

a) b)

Figure 37. Microstructures of 4E and 8E Processed Niobium. a) Sample 19-5 (4E/800^{o}C) b) Sample 4-5 (8E/800^{o}C).

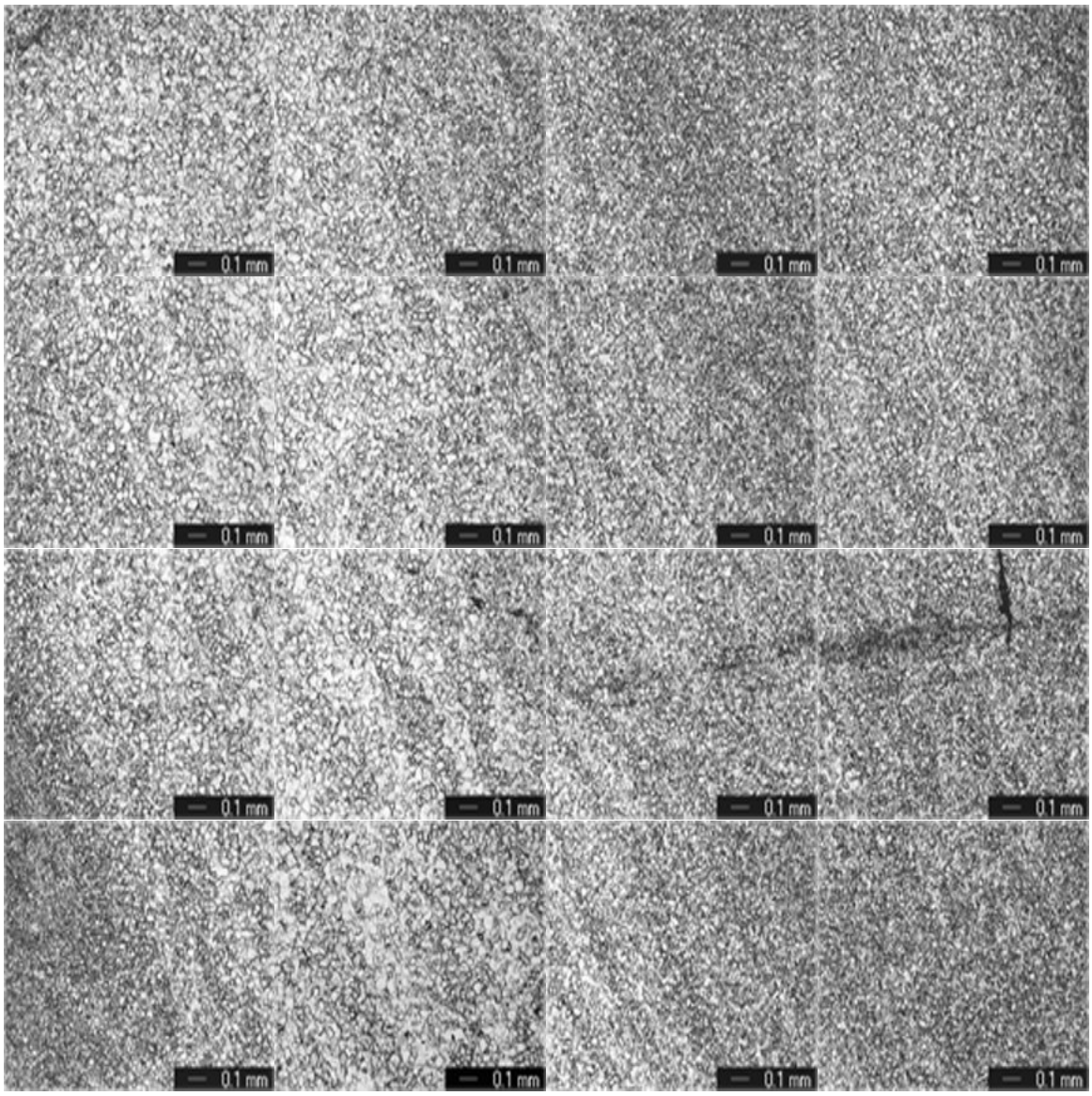

Figure 38. Panoramic View of Sample 2-7 ECAE/4E Processed Pure Nb Annealed at 1000^{o}C.

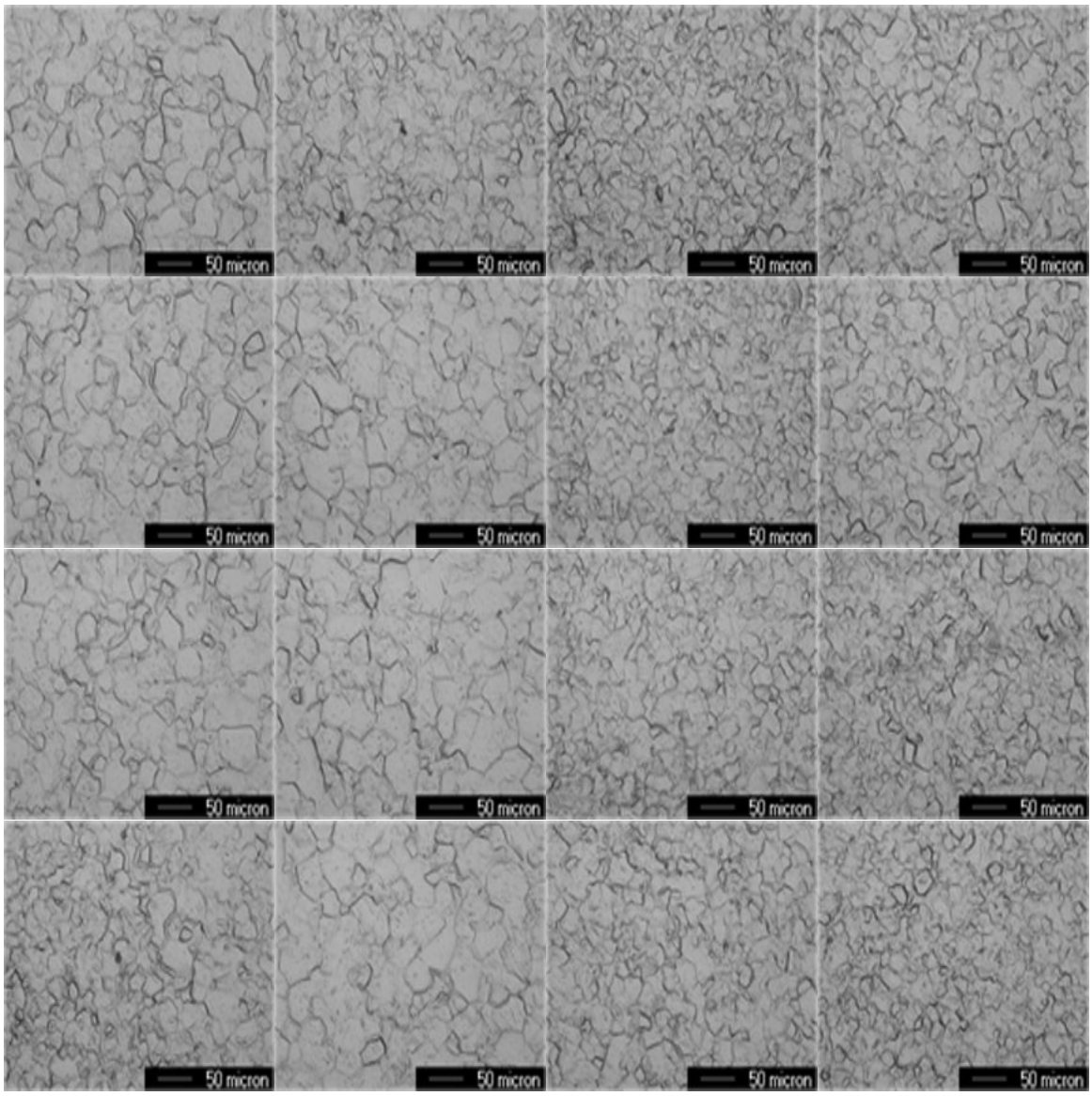

Figure 39. Sample 2-7 That Underwent ECAE 4E/1000^{o}C Annealing. Representative Micrographs of Panoramic Micrographs. Each is 20x Magnification.

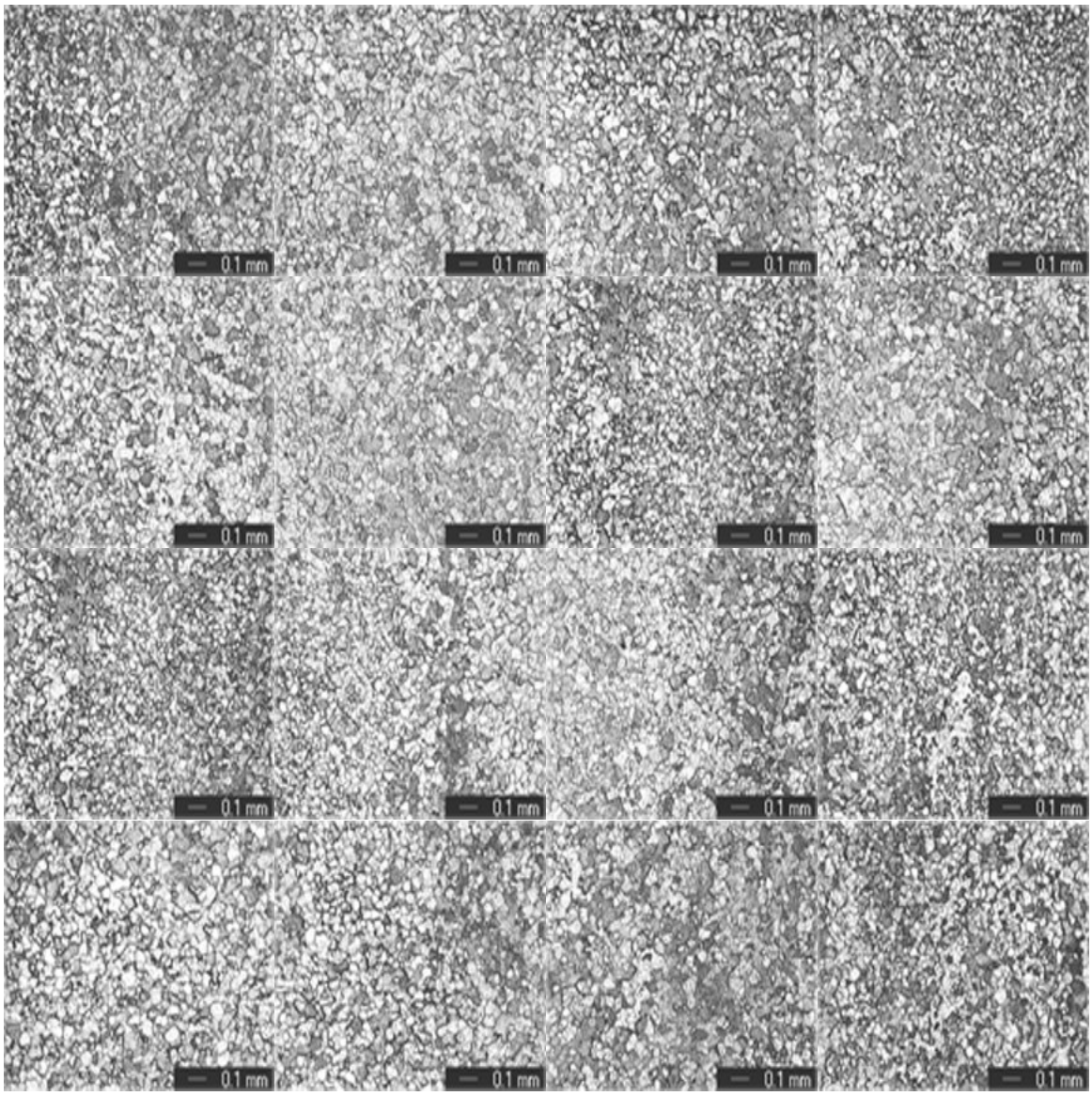

Figure 40. Panoramic View of sample19-7 ECAE/4E Processed Pure Nb Annealed at 1000^{o} C.

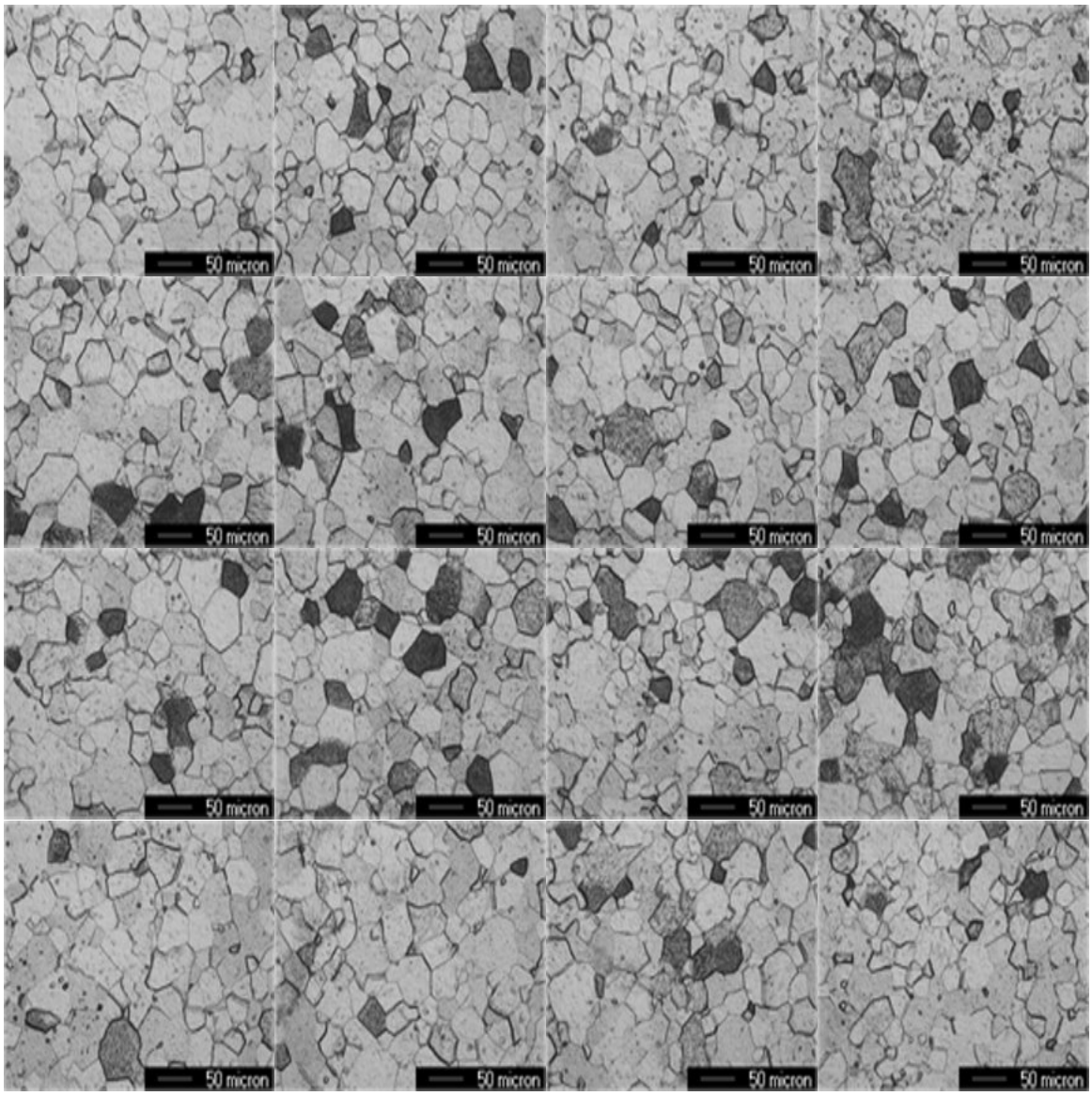

Figure 41. Sample 19-7 That Underwent ECAE 4E/1000^{o}C Annealing. Representative Micrographs of Panoramic Micrographs. Each is 20x Magnification.

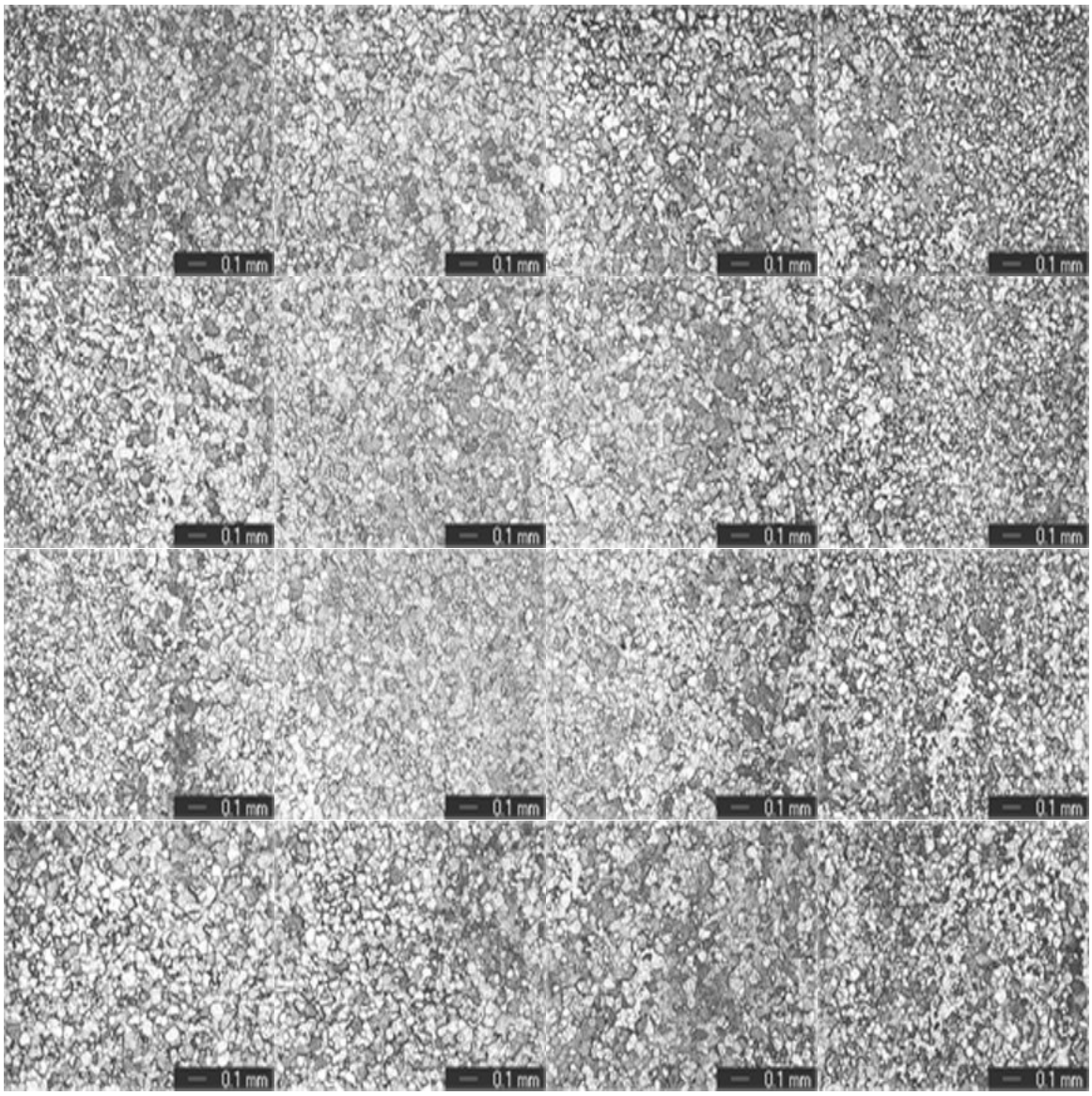

Figure 42. Panoramic View of Sample 4-7 ECAE/8E Processed Pure Nb Annealed at 1000^{o}C.

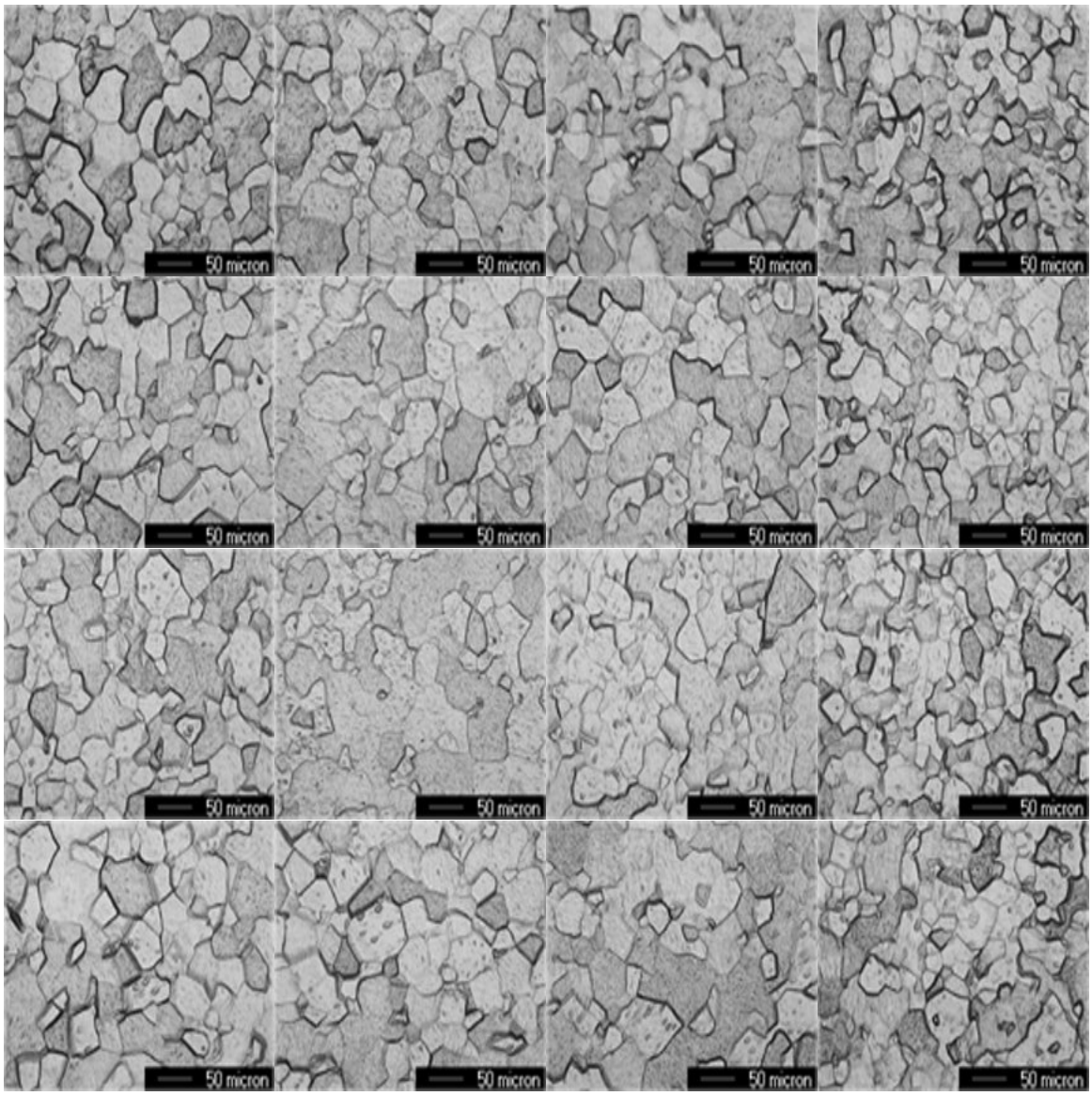

Figure 43. Sample 4-7 That Underwent ECAE 8E/1000^{o}C Annealing. Representative Micrographs of Panoramic Micrographs. Each is 20x Magnification.

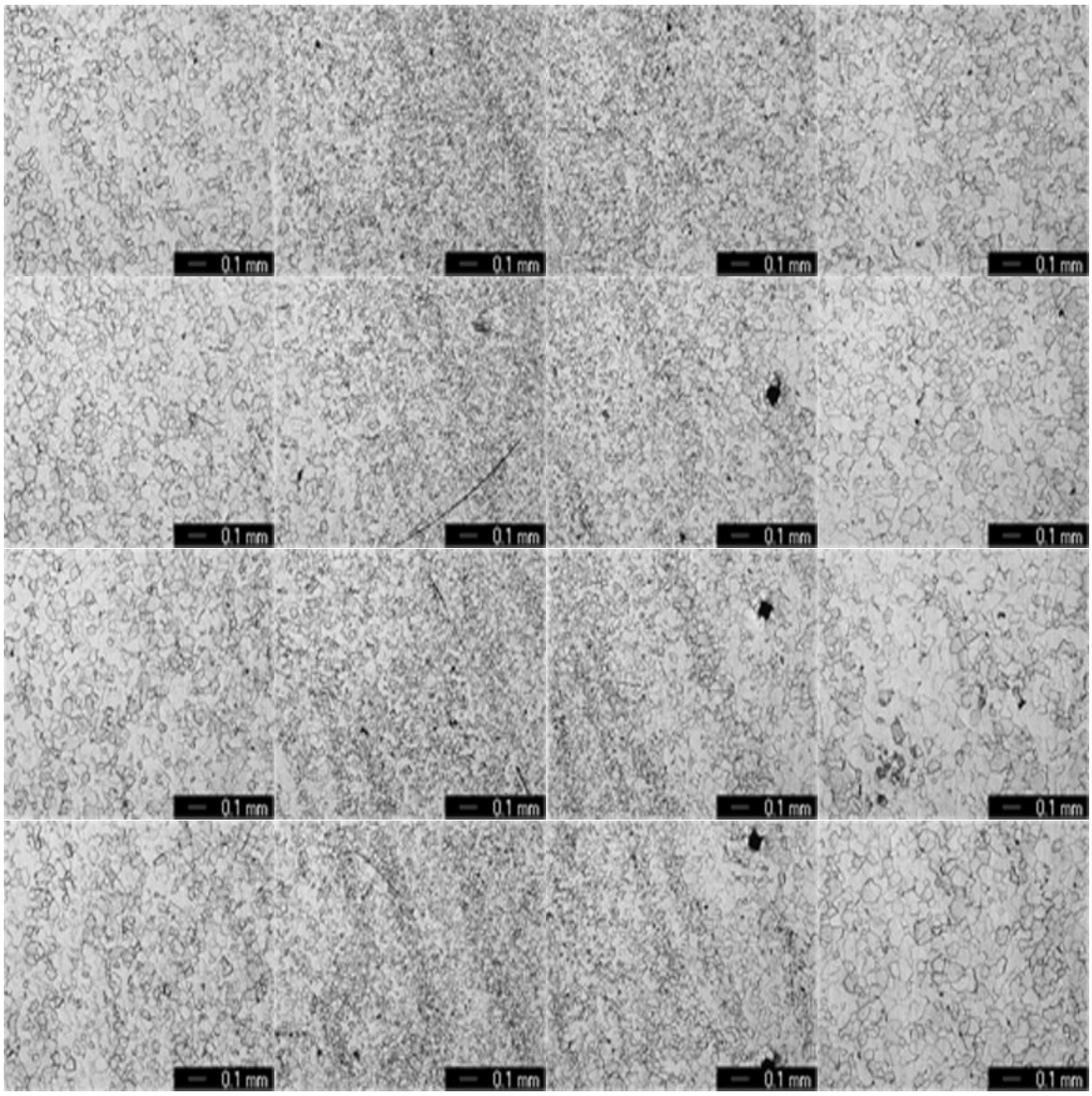

Figure 44. Panoramic View of Sample 2-8 ECAE/4E Processed Pure Nb Annealed at 1100^{o}C.

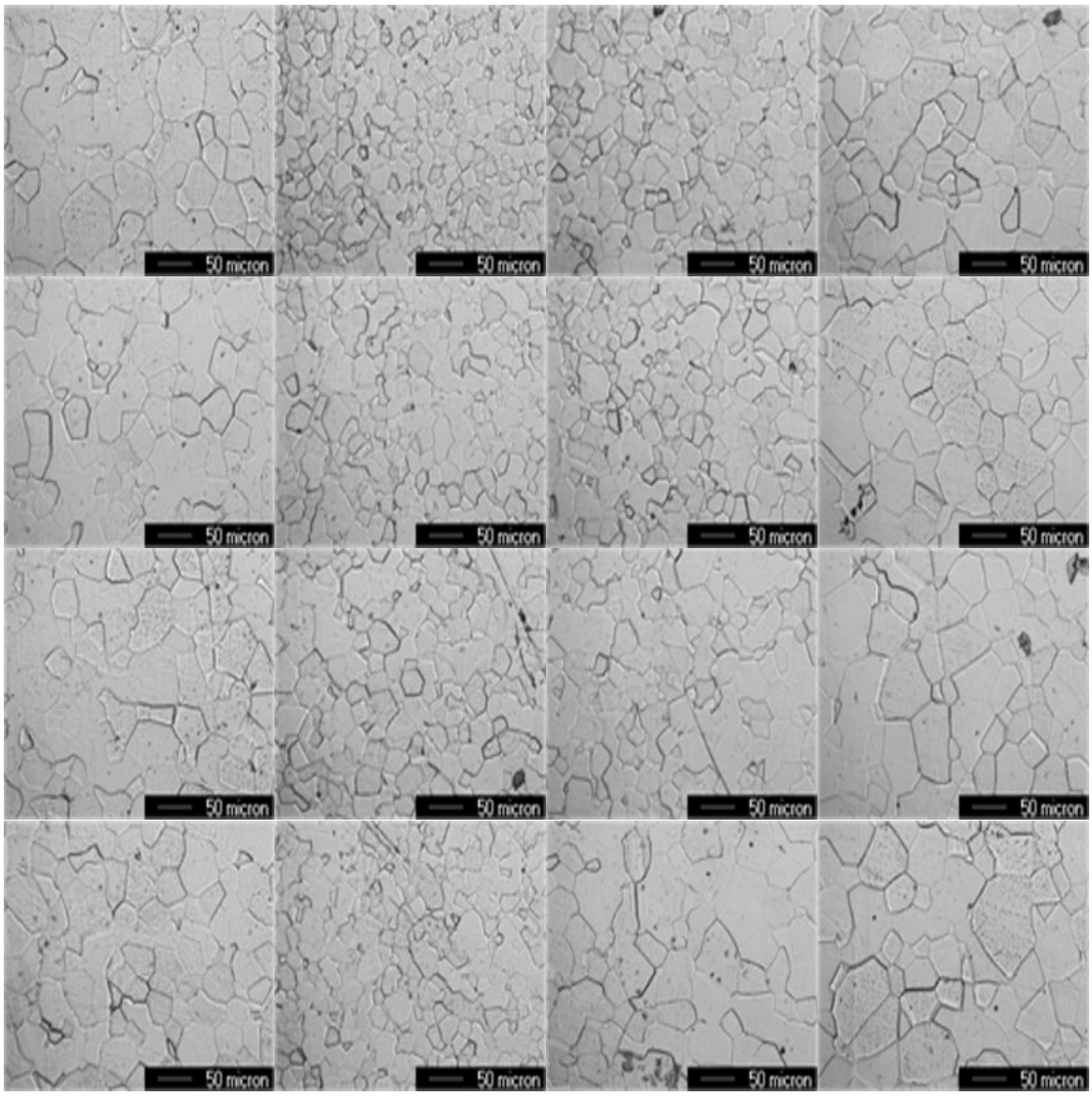

Figure 45. Sample 2-8 That Underwent ECAE 4E/1100^{o}C Annealing. Representative Micrographs of Panoramic Micrographs. Each is 20x Magnification.

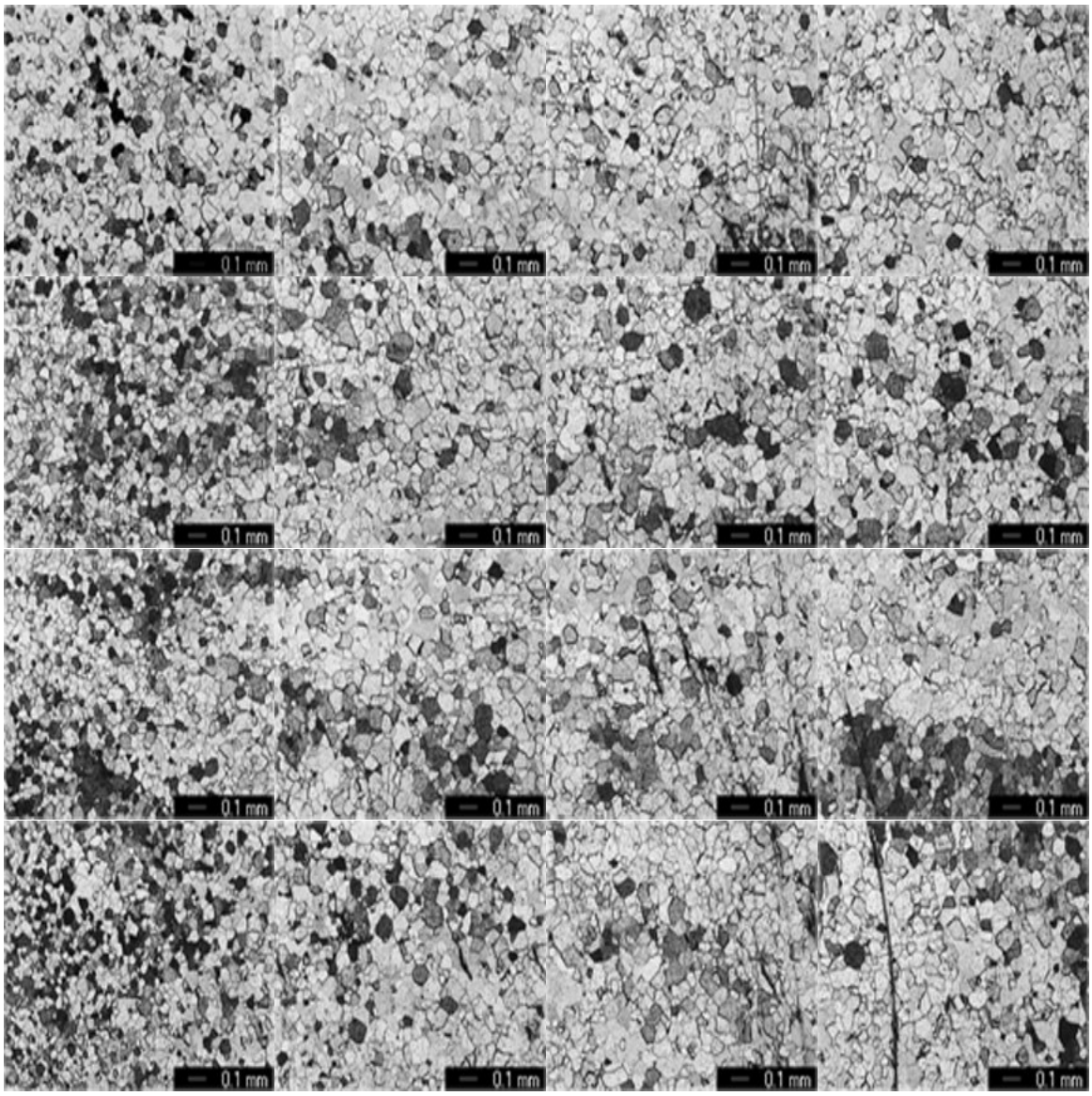

Figure 46. Panoramic View of Sample 19-8 ECAE/4E Processed Pure Nb Annealed at 1100^{o}C.

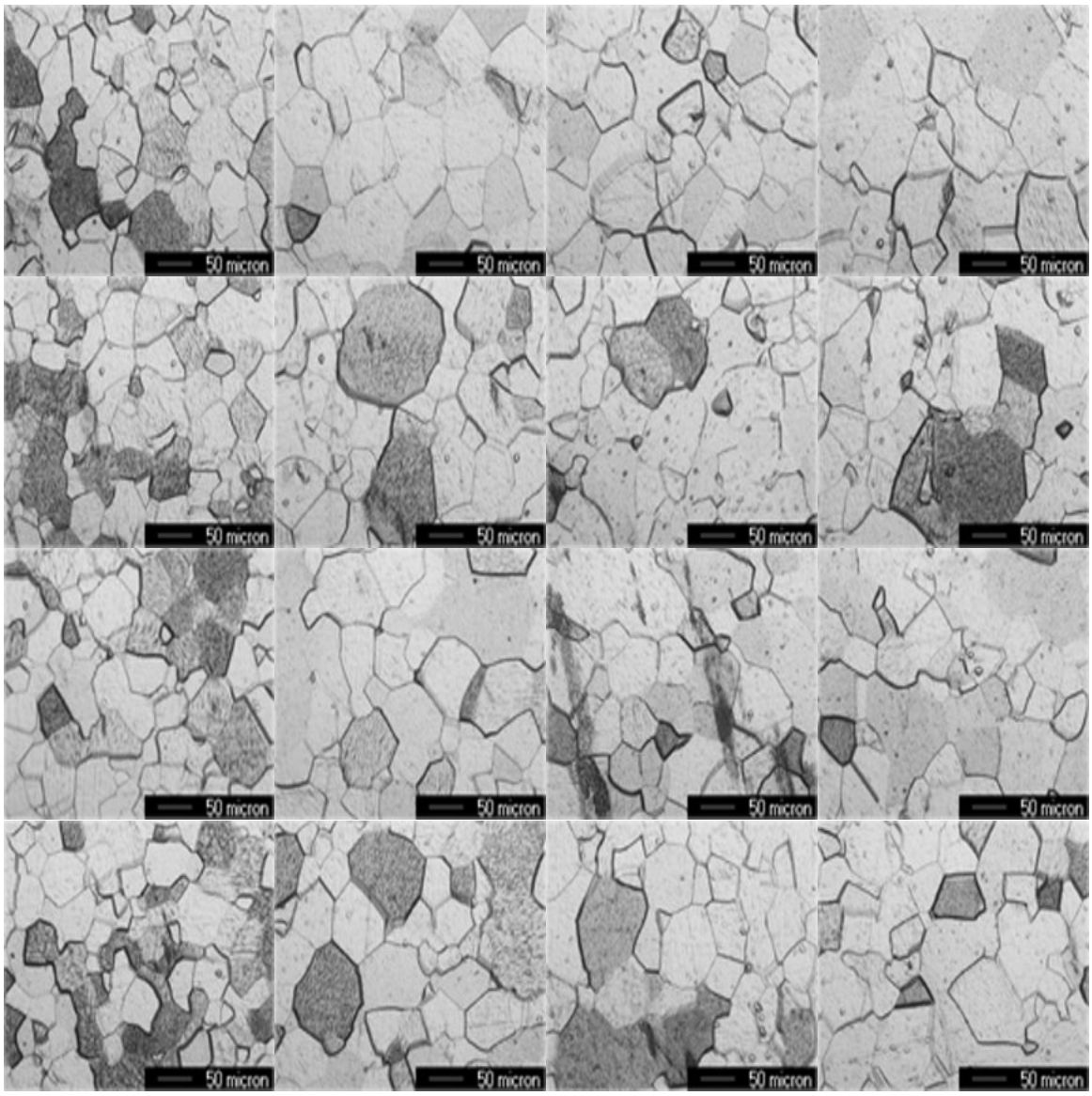

Figure 47. Sample 19-8 That Underwent ECAE 4E/1100^{o}C Annealing. Representative Micrographs of Panoramic Micrographs. Each is 20x Magnification.

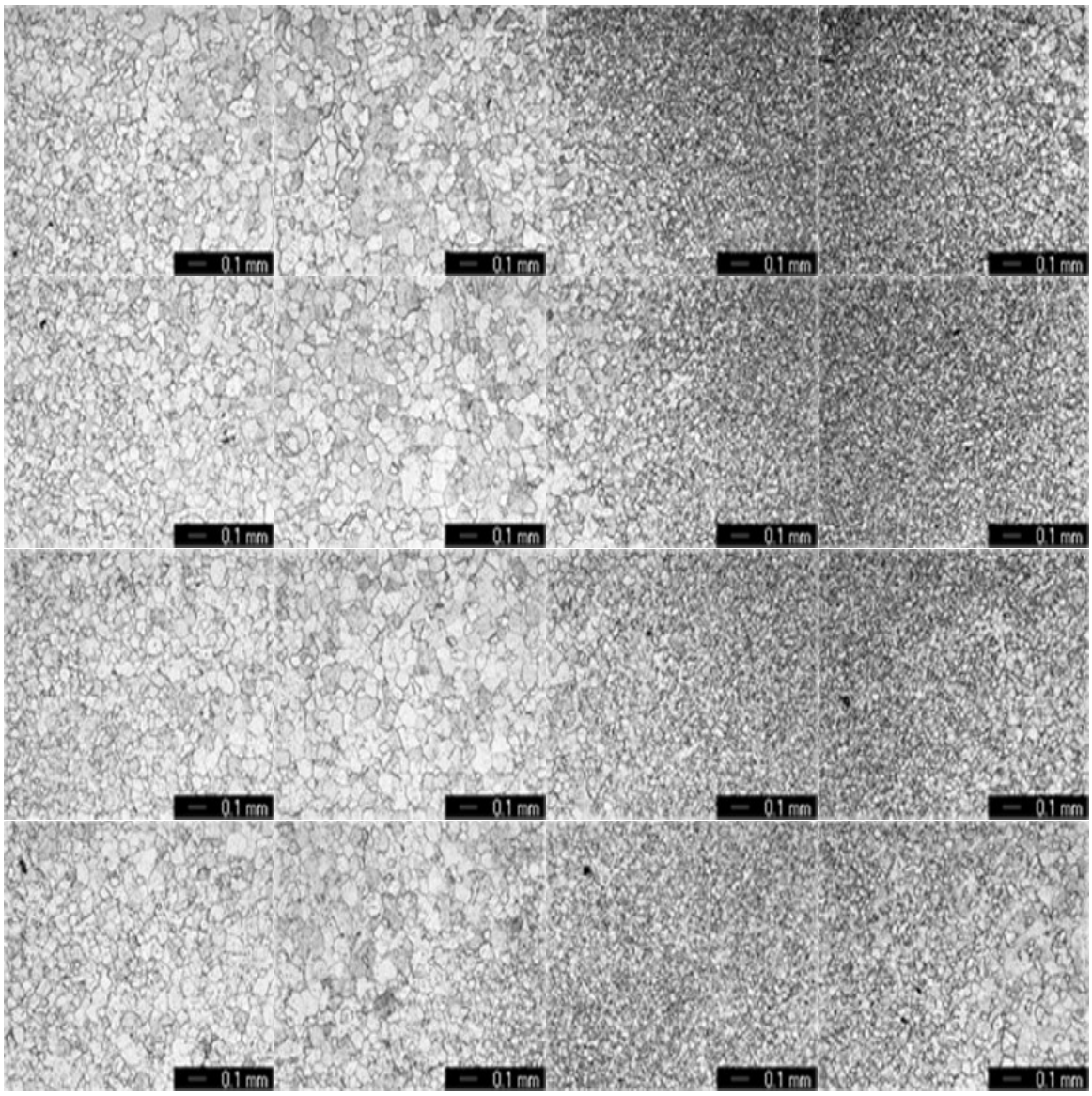

Figure 48. Panoramic View of Sample 4-8 ECAE/4E Processed Pure Nb Annealed at 1100^{o}C.

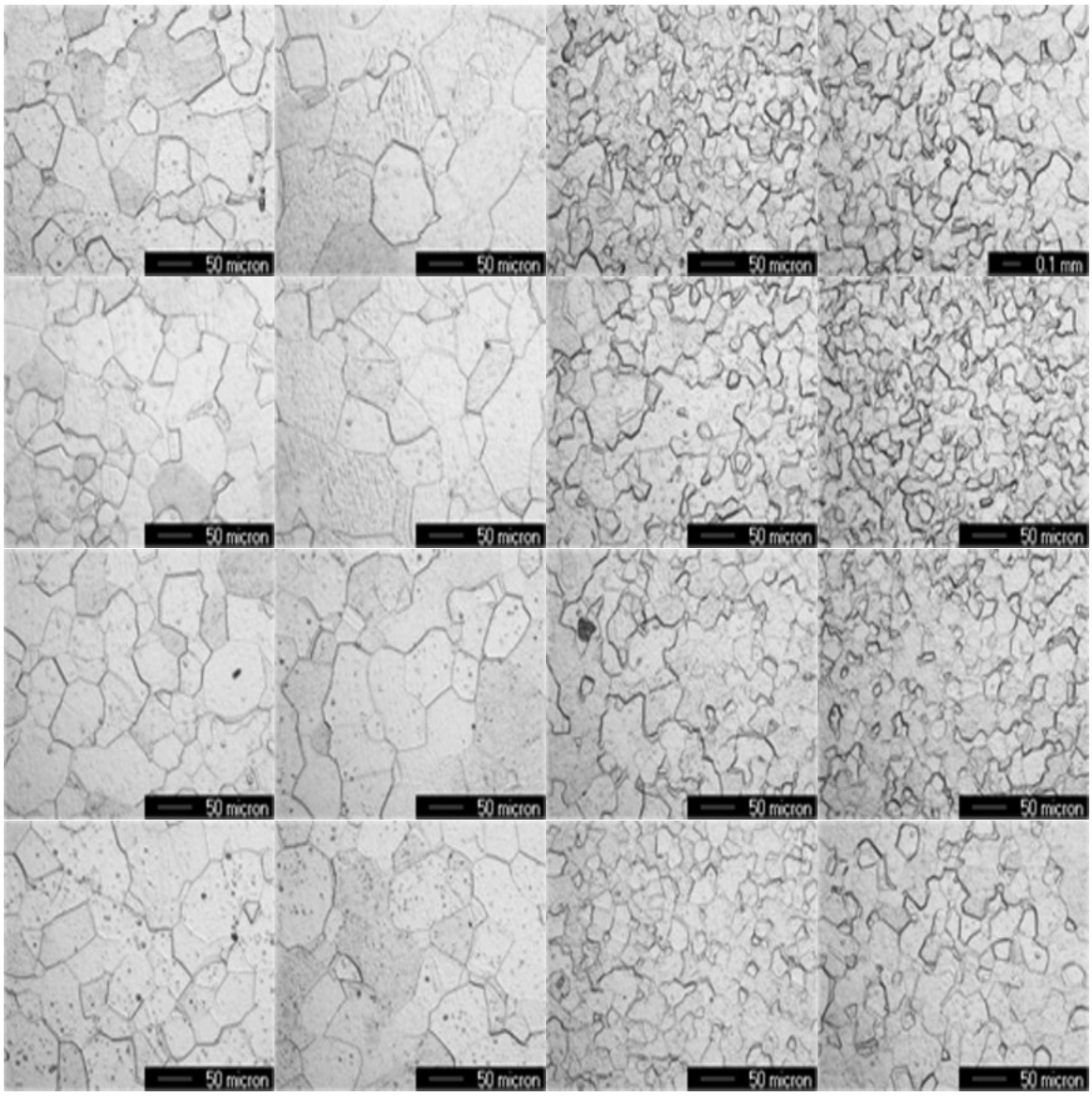

Figure 49. Sample 4-8 That Underwent ECAE 8E/1100^{o}C Annealing. b) Representative Micrographs of Panoramic Micrographs. Each is 20x Magnification.

35	26	21	26
32	32	24	30
32	38	25	24
25	32	27	22

a)

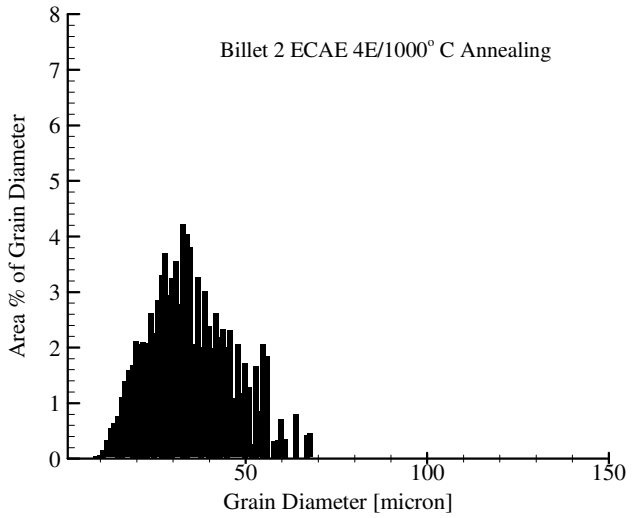

b)

Figure 50. a) Average Grain Diameters of Individual Representative Micrographs for Sample 2-7.
b) Panoramic Grain Size Distribution for Sample 2-7.

36	20	21	33
29	20	22	35
31	25	24	38
34	22	36	40

a)

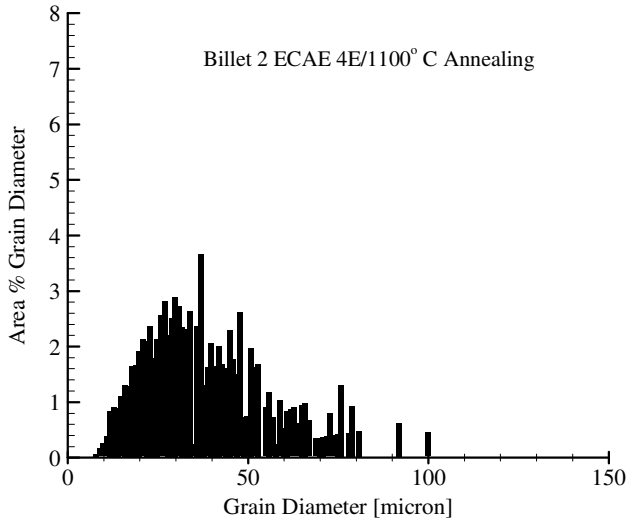

b)

Figure 51. a) Average Grain Diameters of Individual Representative Micrographs for Sample 2-8.
b) Panoramic Grain Size Distribution for Sample 2-8.

31	33	37	39
38	33	30	31
31	30	29	29
32	30	32	28

a)

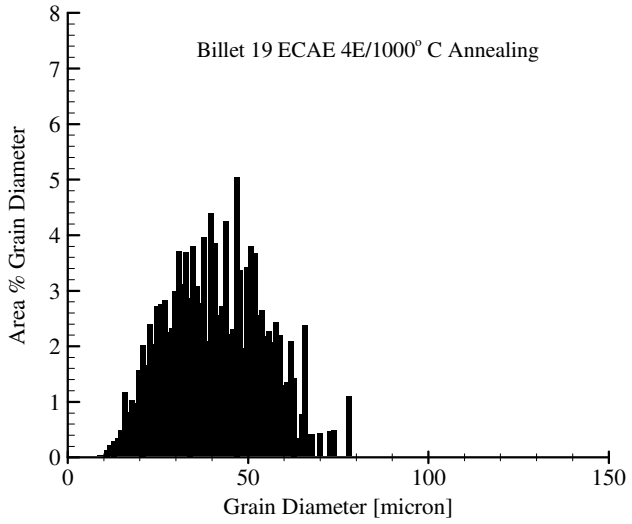

b)

Figure 52. a) Average Grain Diameter of Individual Representative Micrographs for Sample 19-7.
b) Panoramic Grain Size Distribution for Sample 19-7.

33	50	47	50
40	47	39	47
39	49	46	42
35	48	49	46

a)

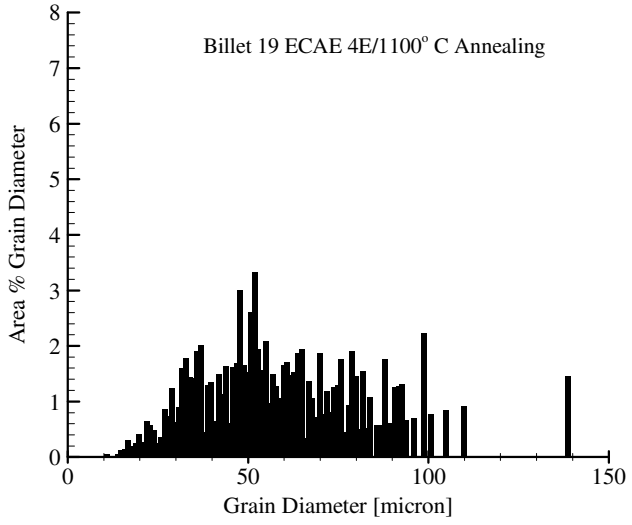

b)

Figure 53. a) Average Grain Diameter of Individual Representative Micrographs for Sample 19-8.
b) Panoramic Grain Size Distribution for Sample 19-8.

34	36	34	34
36	41	37	35
33	36	38	35
38	37	36	33

a)

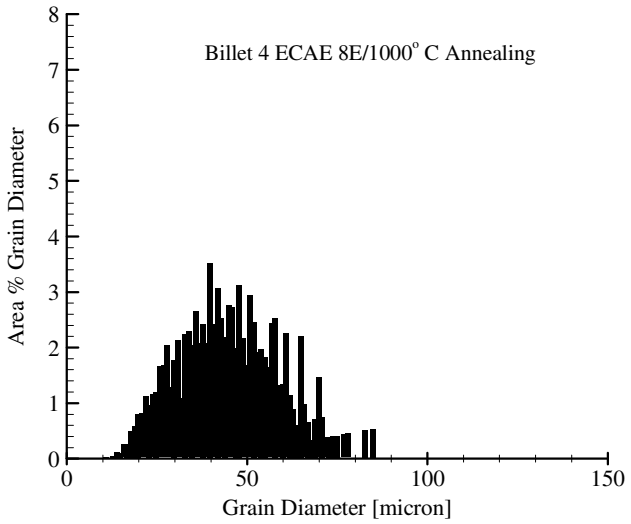

b)

Figure 54. a) Average Grain Diameter of Individual Representative Micrographs for Sample 4-7.
b) Panoramic Grain Size Distribution for Sample 4-7.

37	51	22	26
35	51	24	24
44	48	27	23
41	44	24	27

a)

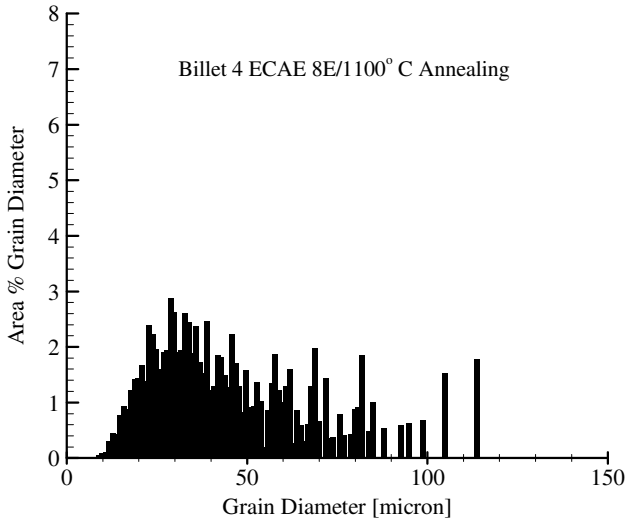

b)

Figure 55. a) Average Grain Diameter of Individual Representative Micrographs for Sample 4-8.
b) Panoramic Grain Size Distribution for Sample 4-8.

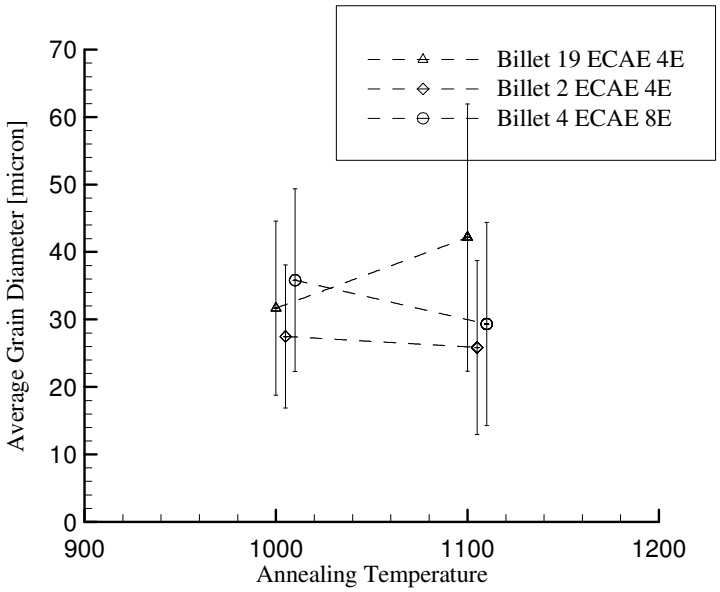

Figure 56. Average Grain Diameter of Reference Metals 4E and 8E ECAE Processed Nb Annealed at 1000^{o} C and 1100^{o} C.

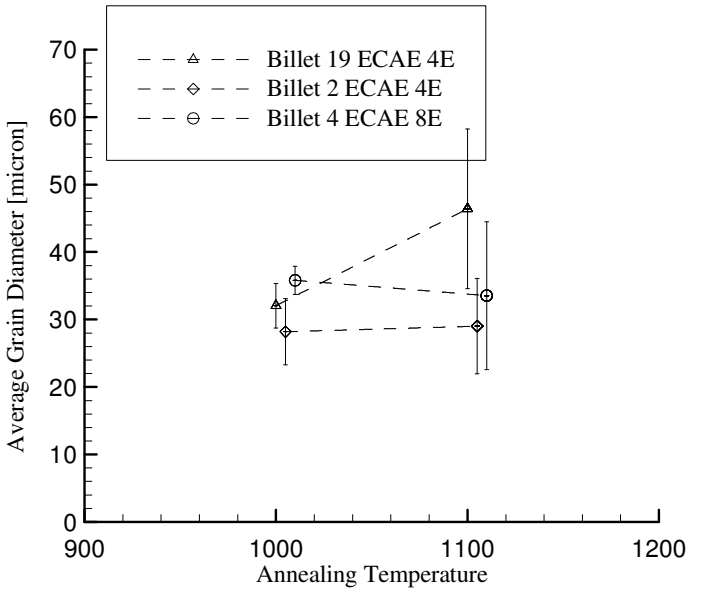

Figure 57. Average Spatial Grain Diameter of Reference Metals 4E and 8E ECAE Processed Nb Annealed at 1000^{o} C and 1100^{o} C.

Table 8. Average Grain Diameter of Reference Metals Panoramic Calculations.

Billet ID	1000° C Annealing		1100° C Annealing	
	Avg Grain Dia. [μm]	Standard Dev.	Avg Grain Dia. [μm]	Standard Dev.
2 (route 4E)	27.5	10.6	25.9	12.9
19 (route 4E)	31.7	12.9	42.2	19.8
4 (route 8E)	35.8	13.5	29.3	15.1

Table 9. Average Grain Diameter of Reference Metals Spatial Calculations.

Billet ID	1000° C Annealing		1100° C Annealing	
	Avg Grain Dia. [μm]	Standard Dev.	Avg Grain Dia. [μm]	Standard Dev.
2 (route 4E)	28.9	4.9	29.2	7.1
19 (route 4E)	32.1	3.3	46.4	11.8
4 (route 8E)	35.8	2.1	33.6	11.0

G. Grain Size Calculations of Wah Chang ECAE/4E Processed Material Annealed at 1000° C and 1100° C

Grain size calculations were performed on Wah Chang ECAE/4E processed material annealed at 1000° C and 1100° C. Methodology of the calculations was the same as that of the Reference Metals. The recrystallized grain morphology of the as-received Wah Chang material shows banding in the z-direction for both the 1000° C and 1100° C annealed states as shown in Figures 58, 59, 60 and 61. After ECAE/4E processing, banding is eliminated yet the grain morphology is not homogeneous as shown in Figures 62, 63, 64 and 65. The average of the representative micrographs and the distribution graphs are shown in Figures 66 and 67. The distribution graphs narrow with decreasing annealing temperature. Average panoramic and representative grain diameters are shown in Figures 68 and 69. The average grain diameter and standard deviation of the ECAE/annealed Wah Chang rod decreases slightly from 21.0 ± 9.5 μm in the 1100° C state to 17.8 ± 6.3 μm in the 1000° C state. Note that grain sizes for the ECAE processed Wah Chang material are significantly less and more homogeneous than that of the Reference Materials. See Tables 10 and 11.

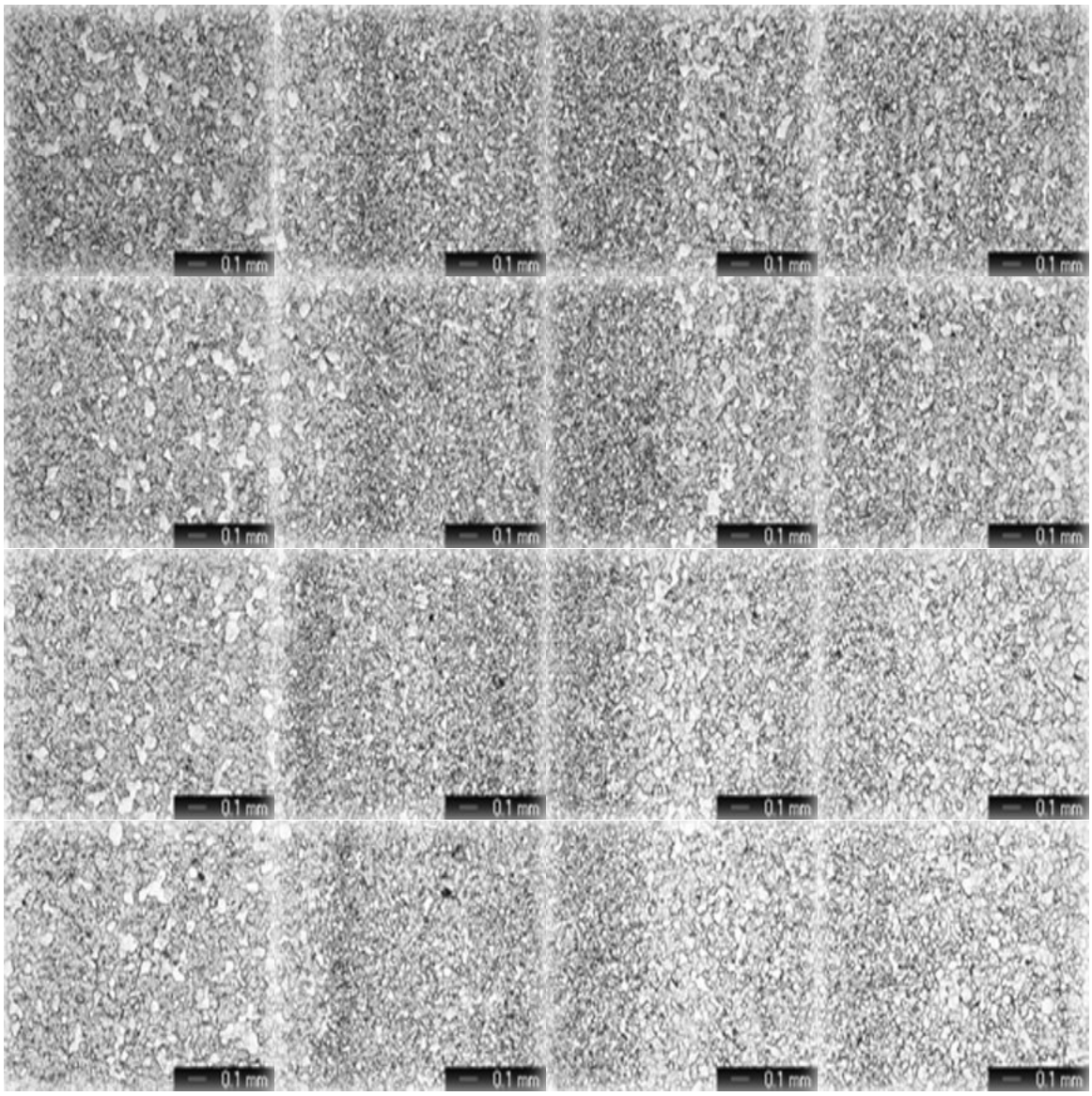

Figure 58. Panoramic View of Sample Wah Chang As-Received Pure Nb Annealed at 1000^{o}C.

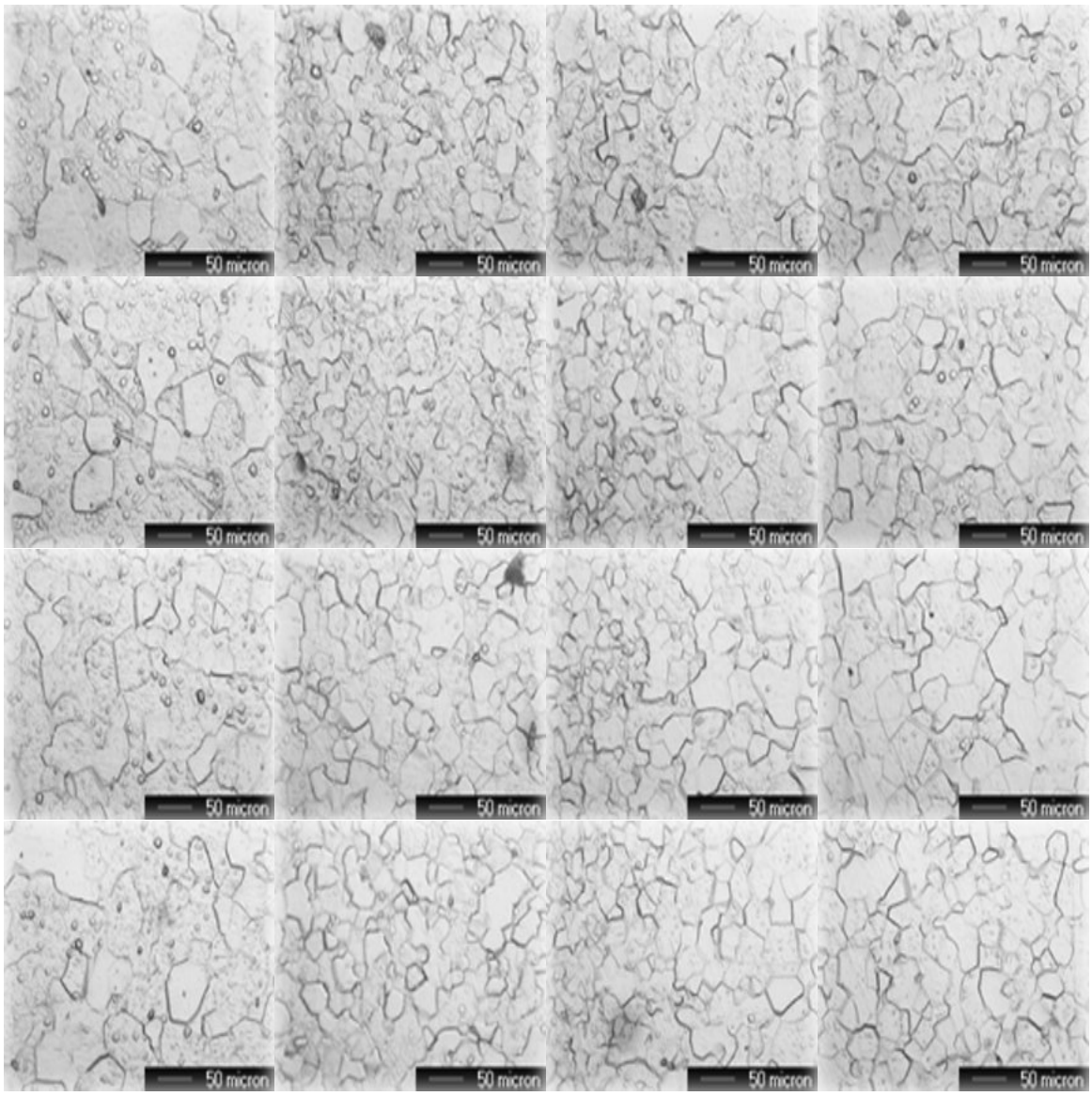

Figure 59. Panoramic View of Wah Chang As-Received Pure Nb Annealed at 1000°C. Representative Micrographs of Panoramic Micrographs. Each is 20x Magnification.

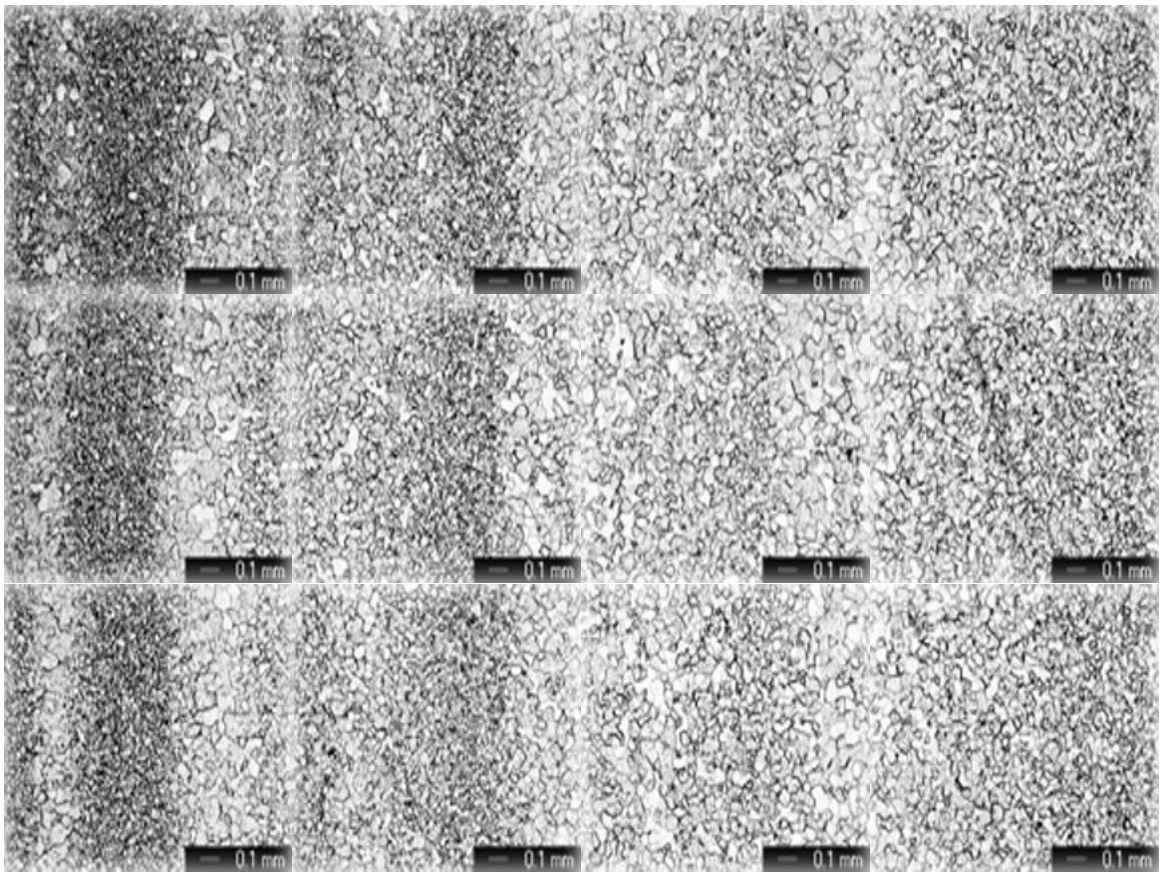

Figure 60. Panoramic View of Sample Wah Chang As-Received Pure Nb Annealed at 1100^{o}C.

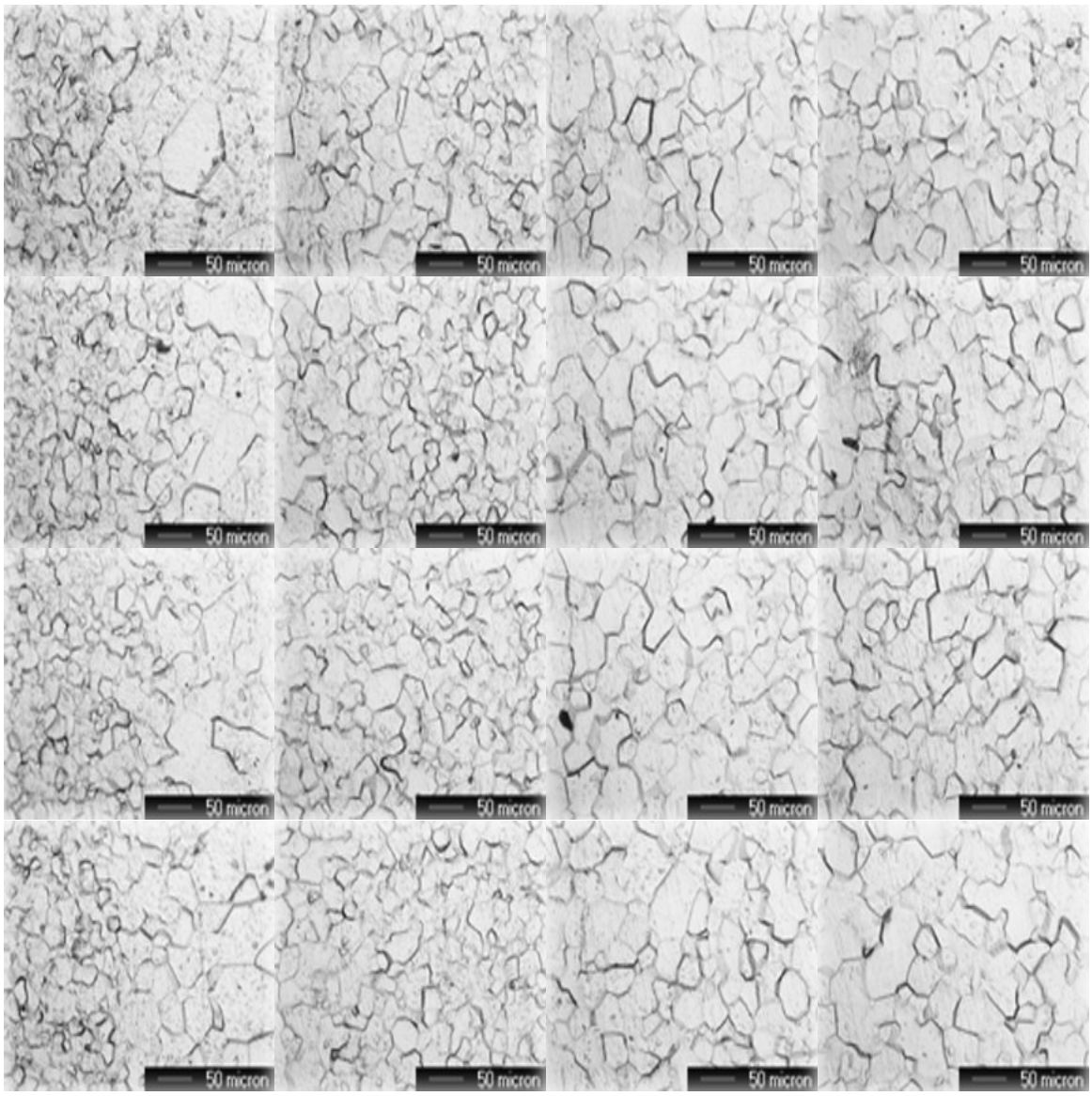

Figure 61. Panoramic View of Wah Chang As-Received Pure Nb Annealed at 1100°C. Representative Micrographs of Panoramic Micrographs. Each is 20x Magnification.

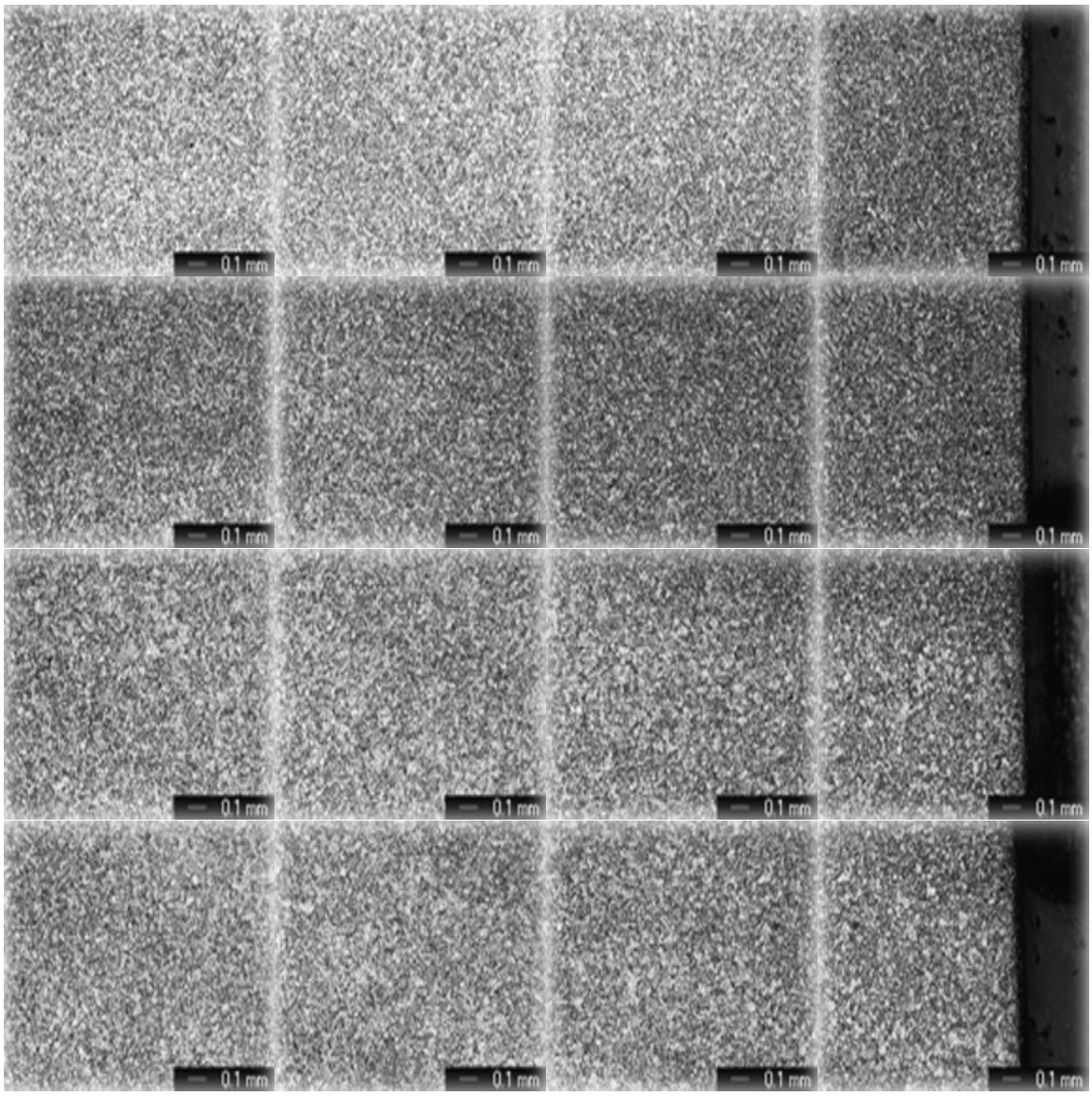

Figure 62. Panoramic View of Sample Wah Chang ECAE/4E Processed Pure Nb Annealed at 1000^{o}C.

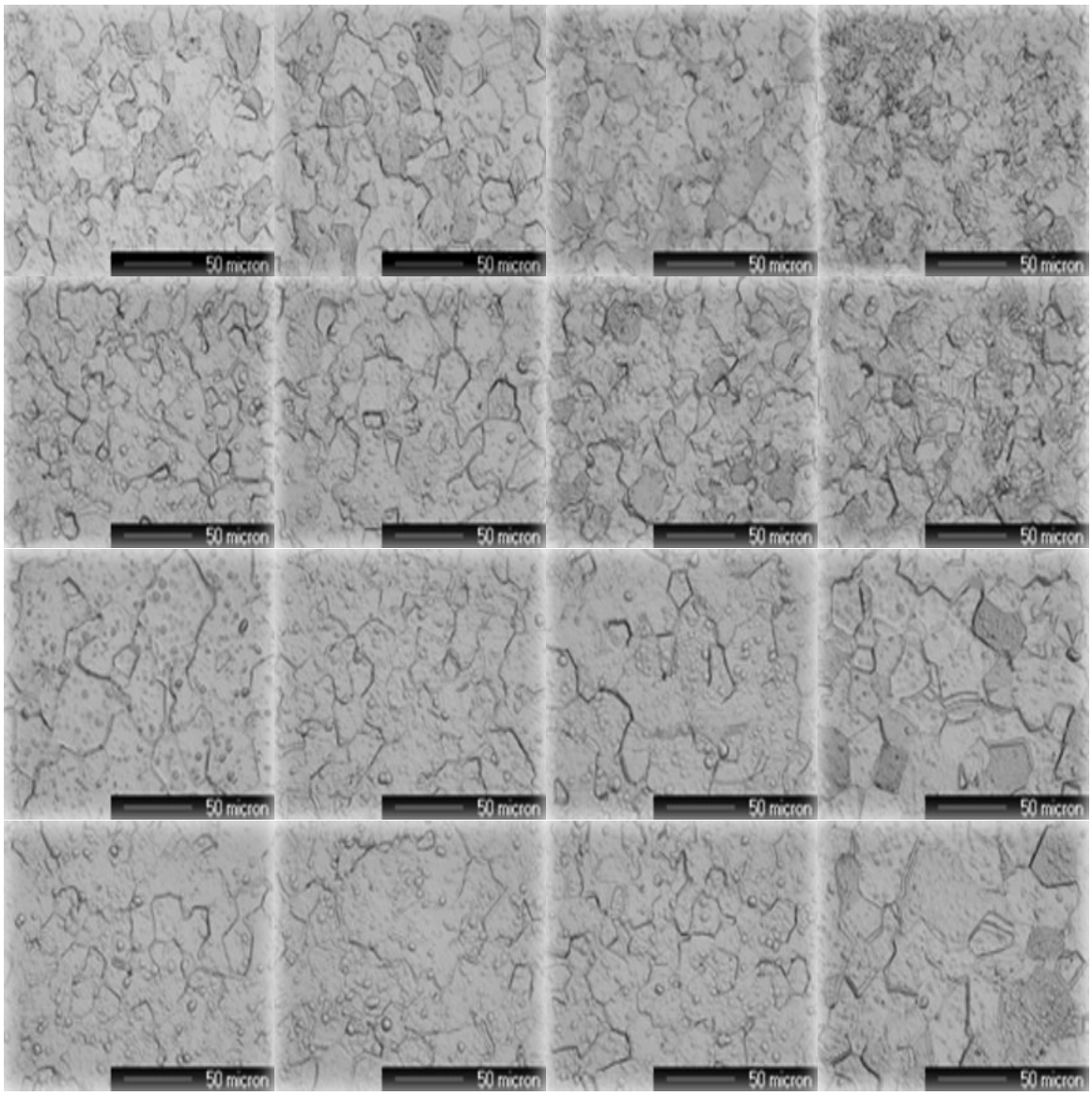

Figure 63. Panoramic View of Wah Chang ECAE/4E Processed Pure Nb Annealed at 1000°C. Representative Micrographs of Panoramic Micrographs. Each is 40x Magnification.

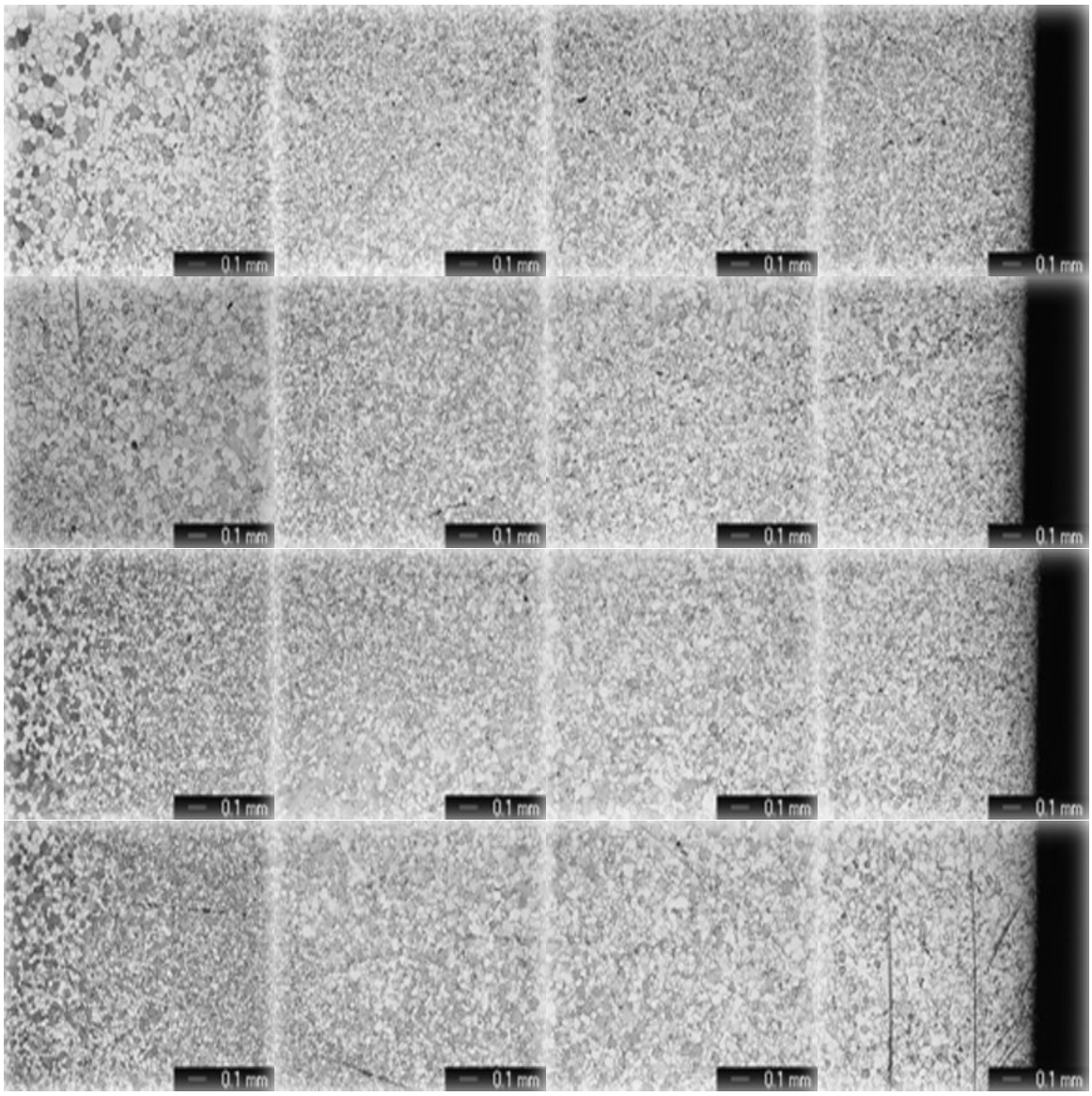

Figure 64. Panoramic View of Sample Wah Chang ECAE/4E Processed Pure Nb Annealed at 1100°C.

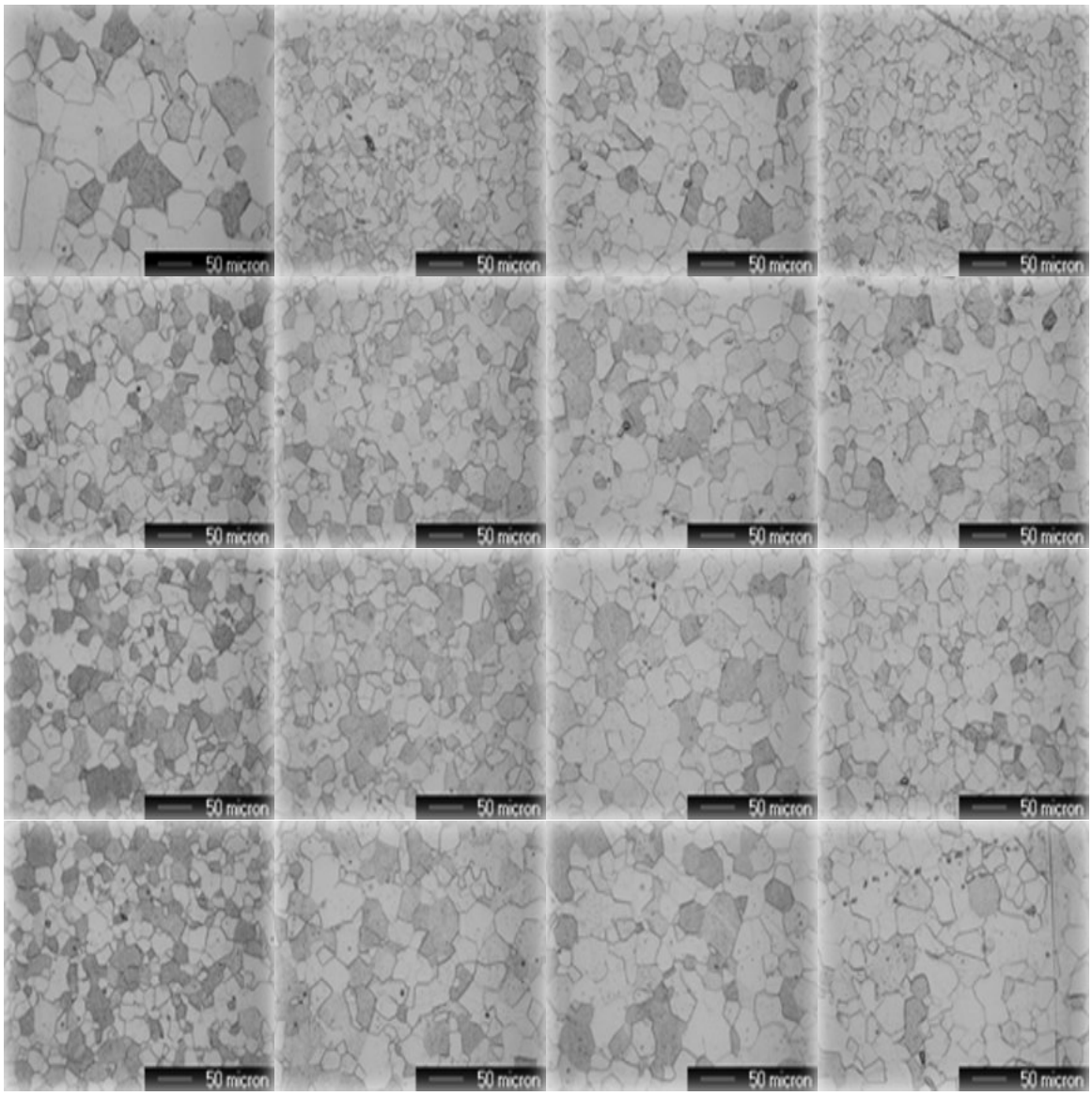

Figure 65. Panoramic View of Wah Chang ECAE/4E Processed Pure Nb Annealed at 1100°C. Representative Micrographs of Panoramic Micrographs. Each is 20x Magnification.

16	18	16	15
16	17	16	18
21	17	21	22
19	20	18	24

a)

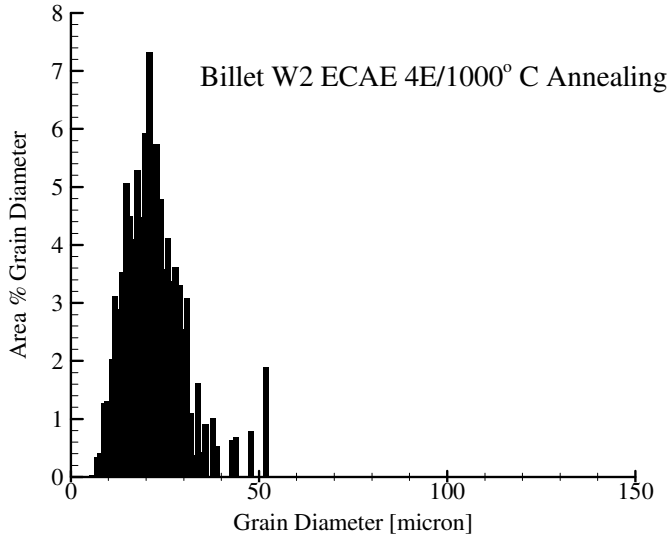

b)

Figure 66. a)Average Grain Diameter of Individual Representative Micrographs for Sample w2-1000°C/4E.
b) Panoramic Grain Size Distribution for Sample w2-1000°C/4E

31	15	15	17
21	18	25	23
19	21	26	23
19	23	26	27

a)

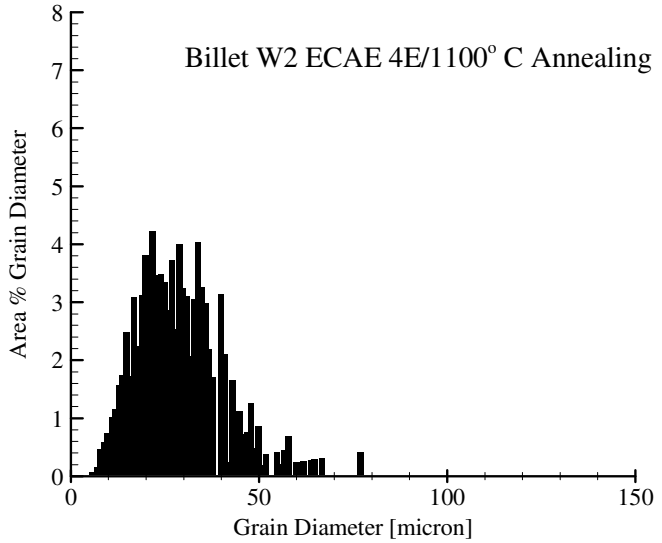

b)

Figure 67. a) Average Grain Diameter of Individual Representative Micrographs for Sample w2-1100°C/4E.
b) Panoramic Grain Size Distribution for Sample w2-1100°C/4E.

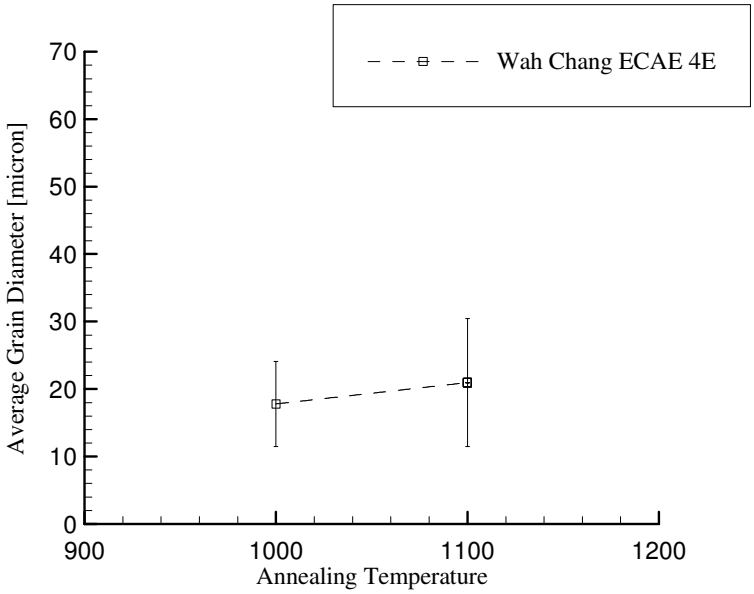

Figure 68. Average Grain Diameter of Wah Chang 4E ECAE Processed Nb Annealed at 1000^{o} C and 1100^{o} C.

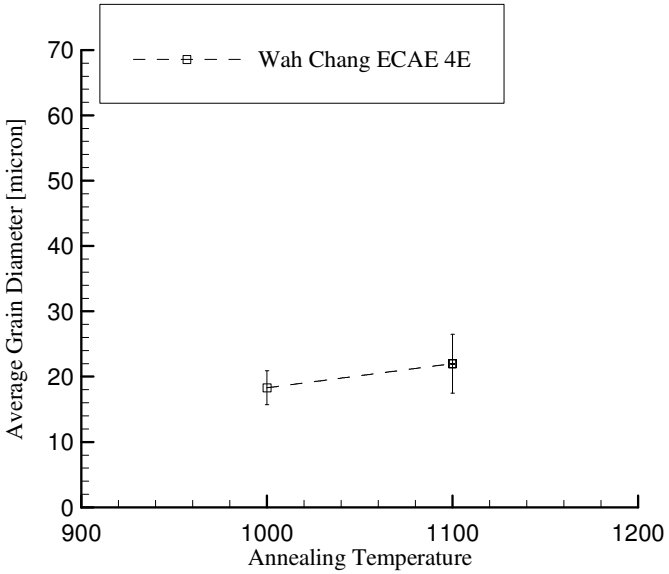

Figure 69. Average Spatial Grain Diameter of Wah Chang 4E ECAE Processed Nb Annealed at 1000^{o} C and 1100^{o} C.

Table 10. Average Grain Diameter of Wah Chang Panoramic Calculations.

Billet ID	1000° C Annealing		1100° C Annealing	
	Avg Grain Dia. [μm]	Standard Dev.	Avg Grain Dia. [μm]	Standard Dev.
W2 (route 4E)	17.8	6.3	21	9.5

Table 11. Average Grain Diameter of Wah Chang Spatial Calculations.

Billet ID	1000° C Annealing		1100° C Annealing	
	Avg Grain Dia. [μm]	Standard Dev.	Avg Grain Dia. [μm]	Standard Dev.
W2 (route 4E)	18.3	2.6	22	4.5

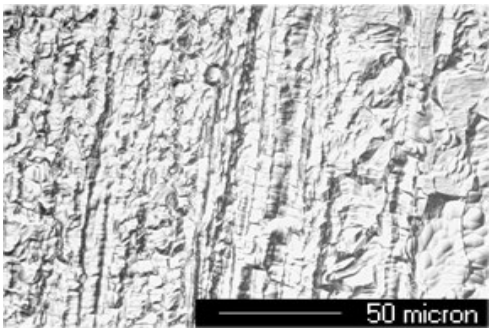

Figure 70. As-Received Wah Chang Material Annealed at 900° C; Micrograph of Sample ID WC-900C-40xJ.

H. Tensile Tests

1. Introduction

Tensile tests of as-cast, as-worked, recovered and recrystallized Reference Metals niobium has been completed for ECAE routes 1A, 2C, 4E and 8E. Ultimate tensile strength, 0.2 % yield strength, failure strains and toughness have been determined as a function of ECAE route, annealing temperature and $Vickers_{300}$ hardness for a total of 36 samples.

Pure niobium was tensile tested using two separate methods: as-cast and recrystallized materials were tested using a 3mm extensometer; as-worked and recovered materials were tested using a half inch extensometer. The as-cast and recrystallized materials were first tested using the three mm extensometer when it was realized that samples were not necking near the center of the specimen. This made it difficult to place the extensometer at the necking region. As a solution, all other samples (as-worked and recovered) samples were tested using the half inch extensometer. To be consistent, strain failures were calculated by placing the tests pieces back together and measuring the length with calipers and determining the elongation at failure by standard methods. A total of 36 samples were tested (14 as-cast and recrystallized, 13 as-worked and 9 recovered). Toughness is defined as the area under the stress/strain curve. Areas were approximated by drawing triangles or squares over plots and then taking the area of the squares or triangles as shown in Figure 71. Note that the positive and negative areas cancel each other out. It is believed that the error for the toughness approximation method is below 10%. The following is an example of how toughness for sample 24-3B was calculated.

$$\text{Toughness (sample 24-3B)} = \frac{1}{2} \times 400 \times 0.24 = 48 MJ / m^3$$

0.2 % yield stress measurements were taken by blowing-up the stress/strain figure and drawing a line parallel to the elastic region as shown in Figure 72. All specimens were cut from the niobium blocks as shown in Figure 73. All samples were originally cut to a 3 mm×3 mm cross section, but due to the strength of the as-worked and recovered material, these samples were sliced lengthwise by EDM to reduce the cross sectional area by half as shown in Figure 74. A horizontal line was then drawn from the intersection of the elastic parallel line and the stress/strain curve to determine the 0.2 % yield stress. A similar method was used to determine the maximum stress. The stress/strain curve was blown-up to at the maximum stress and a horizontal line was drawn to the stress axis. Results were averaged when duplicate samples were tested along with the standard deviations (in parentheses). The following definitions apply for all tensile test tables:

* Used Dr. Hartwig's 3mm extensometer.
** Used Dr. Lagoudas's half inch extensometer.
† Strain rate 5×10^{-5}
‡ Strain rate 10^{-2}

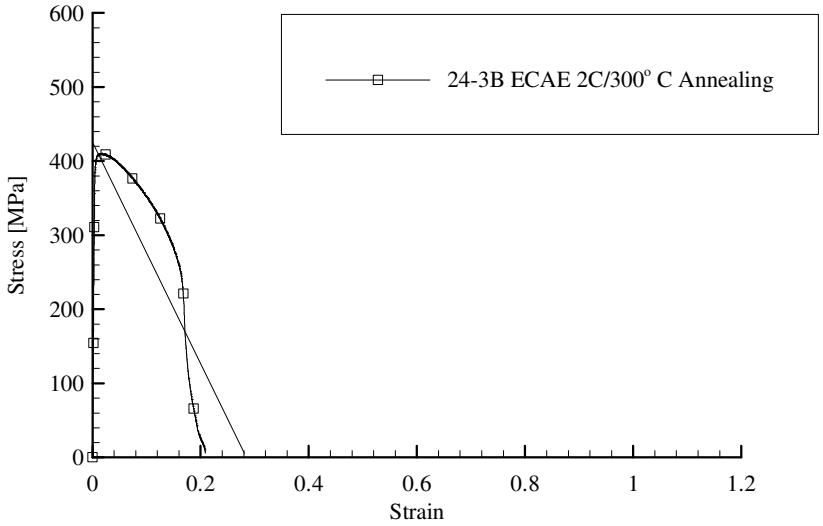

Figure 71. Example of Toughness Calculation for Sample 24-3B.

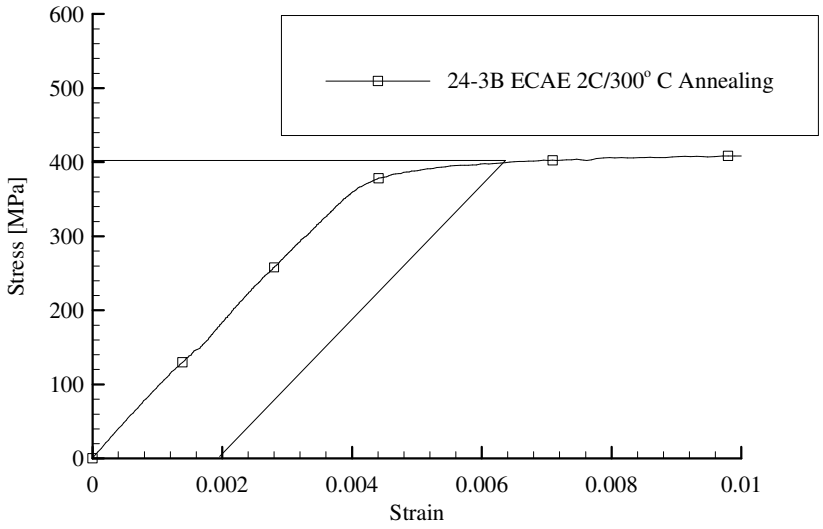

Figure 72. Example of 0.2 % Yield Stress Determination for Sample 24-3B.

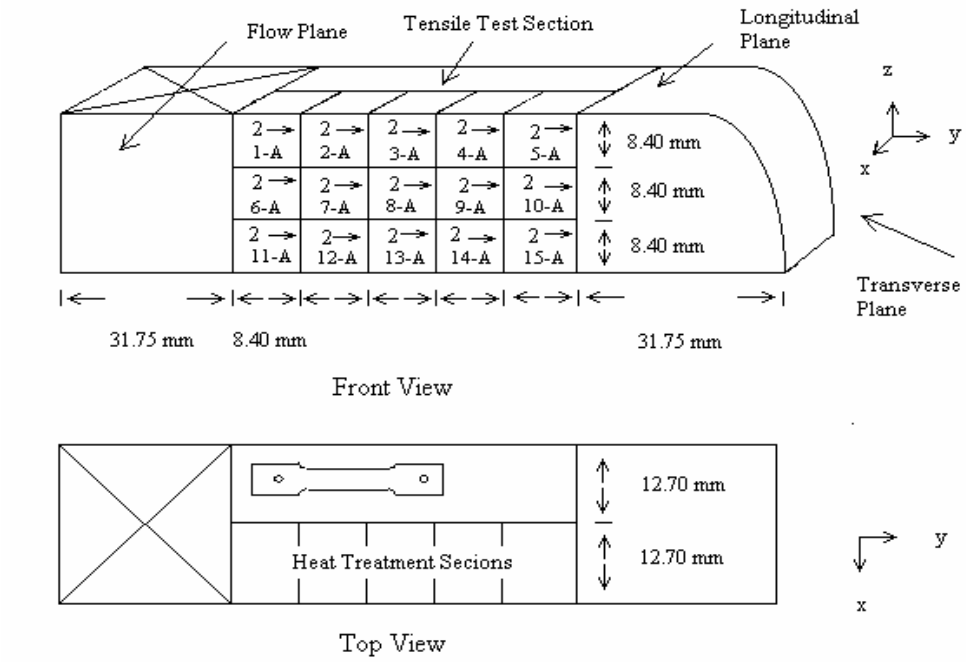

Figure 73. Schematic of Tensile Test Specimen Orientation with Respect to Billet.

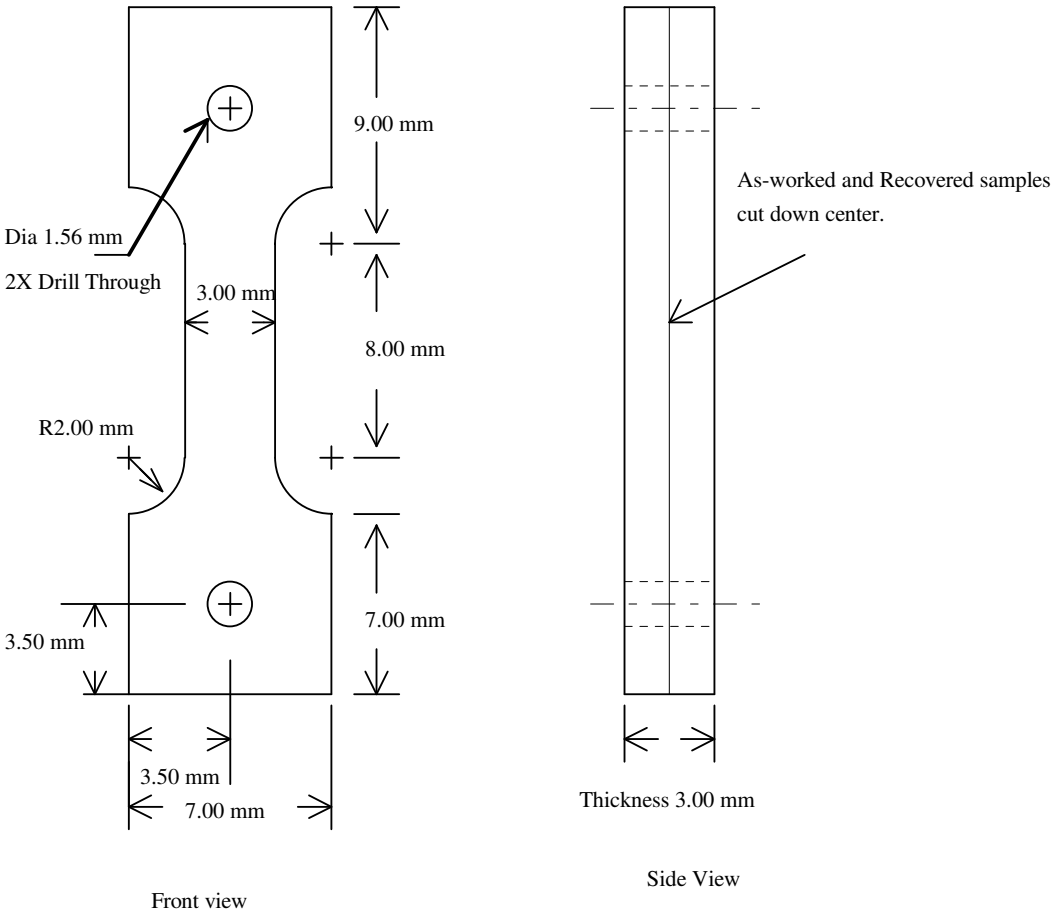

TOLERANCES	Dog-Bone Diagram	
XX.: ± 0.01 mm	Niobium	OCT. 3, 2003

Figure 74. Tensile Test Specimen Schematic of Niobium.

2. Failure Strain Results (Elongation)

Failure strain results for ECAE processed niobium show that the strain failure is an increasing function of annealing temperature as shown in Figure 75. Recrystallized failure strains for the ECAE processed material (average of 0.64) were approximately three times that of the as-worked (average of 0.21) and of the recovered samples (average of 0.21). The as-cast material showed the largest failure strain with an average of 0.90. Because grain size is an increasing function of annealing temperature, one can conclude that the failure strain of the ECAE processed material would continue to increase with increasing annealing temperature, eventually

reaching that of the as-cast value. Another data point around the 800° C annealing mark would closer determine the rate at which the as-cast failure strain would be reached. Figure 76 shows the failure strain as a function of $Vickers_{300}$ hardness and Figure 77 shows strain failure as a function of number of passes. Note that the failure strain of the as-cast material is approximately 33%larger than the processed recrystallized material. Failure strains are shown in Tables 12, 13 and 14.

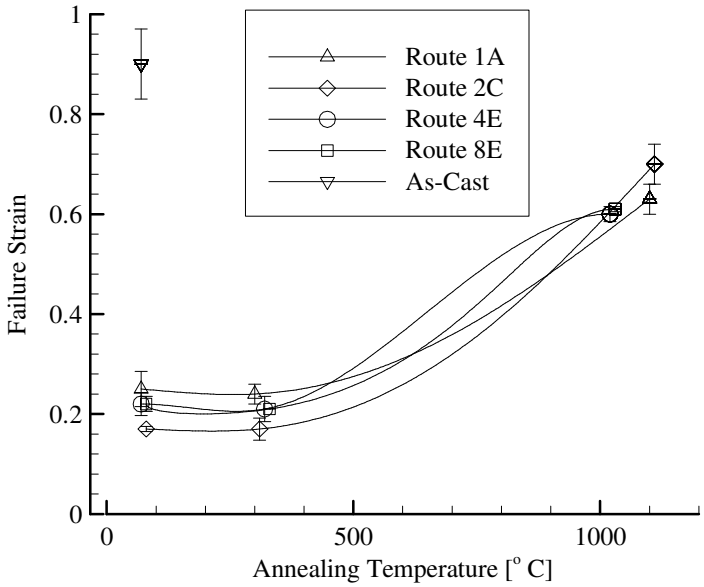

Figure 75. Failure Strain vs Annealing Temperature for Reference Metals As-Cast and ECAE Processed Niobium.

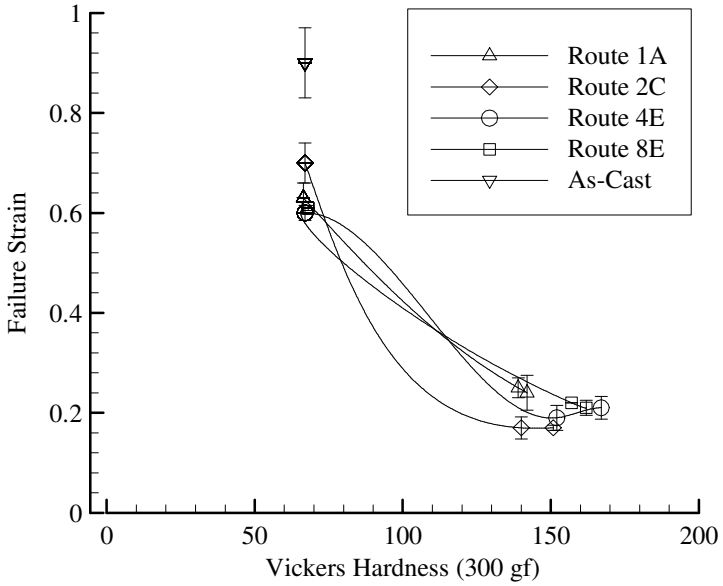

Figure 76. Failure Strain vs Vickers Hardness for Reference Metals As-Cast and ECAE Processed Niobium.

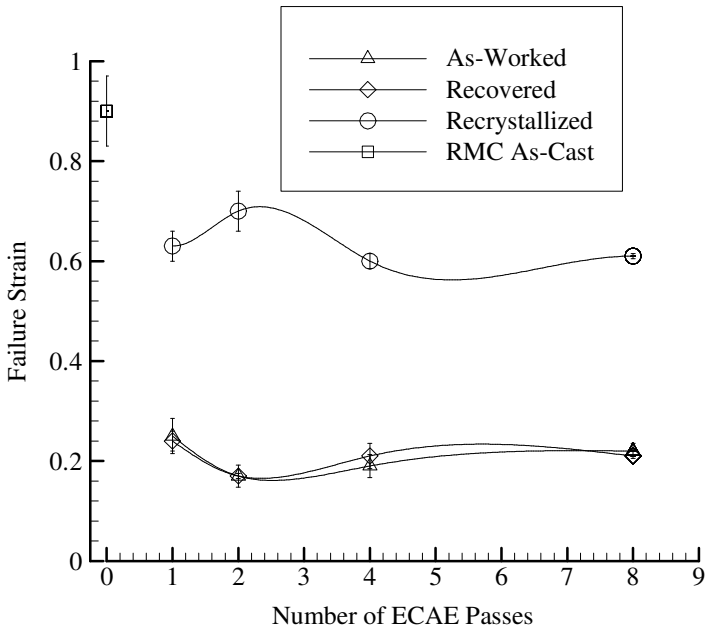

Figure 77. Failure Strain vs Number of Passes for Reference Metals As-Cast and ECAE Processed Niobium.

Table 12. Failure Strain for As-Worked ECAE Processed Reference Metals and Wah Chang Materials.

Specimen Id	Route/Anneal Temp.	Cross sect. Area [mm^2]	Strain $\gamma_{failure}$	Avg. $\gamma_{failure}$ (STD)	Vickers Hardness (300gf)
3-1B**	1A/As-Work	3.95	0.23	0.25 (0.035)	146.68
3-2B**	1A/As-Work	4.08	0.31		
18-5B**	1A/As-Work	4.11	0.22		131.58
18-6B**	1A/As-Work	4.05	0.25		
17-5B**	2C/As-Work	4.07	0.17	0.17 (0.005)	137.12
17-6B**	2C/As-Work	4.04	0.18		
24-4B**	2C/As-Work	3.87	0.17		142.42
2-3A**	4E/As-Work	3.46	0.23	0.19 (0.023)	151.7
2-3B**	4E/As-Work	3.95	0.17		
2-4A**	4E/As-Work	4.10	0.18		
2-4B**	4E/As-Work	4.11	0.18		
4-4A**	8E/As-work	4.01	0.20	0.22 (0.015)	156.92
4-4B**	8E/As-work	4.08	0.23		
Avg.			**0.21 (0.04)**		**144.4 (8.53)**
WC-2A**	As-Received/As-work	3.96	0.25	0.25 (0.005)	141.68
WC-2B**	As-Received/As-work	4.20	0.24		
Avg.			**0.25 (0.005)**		**141.68**
W2-2A**	4E/As-Work	4.07	0.21	0.21 (0.005)	153.68
W2-2B**	4E/As-Work	4.11	0.20		
Avg.			**0.21 (0.005)**		**153.68**

Table 13. Failure Strain for Recovered ECAE Processed Reference Metals and Wah Chang Materials.

Specimen Id	Route/Anneal Temp.	Cross sect. Area [mm^2]	Strain $\gamma_{failure}$	Avg. $\gamma_{failure}$ (STD)	Vickers Hardness (300gf)
18-3B**	1A/300°C	4.11	0.22	0.24 (0.02)	141.58
18-4B**	1A/300°C	4.07	0.26		
17-3B**	2C/300°C	4.08	0.14	0.17 (0.022)	150.92
17-4B**	2C/300°C	4.08	0.18		
24-3B**	2C/300°C	4.06	0.19		150.44
2-1B**	4E/300°C	4.06	0.24	0.21 (0.025)	167.26
2-2A**	4E/300°C	4.06	0.20		
2-2B**	4E/300°C	4.06	0.18		
4-3B**	8E/300°C	4.05	0.21	0.21	161.88
Avg.			**0.20 (0.033)**		**155.4 (10.1)**
WC-1B**	AsRec/300°C	4.16	0.25	0.25	142.2
W2-1B**	4E/300°C	4.10	0.20	0.20	157.3

Table 14. Failure Strain for Recrystallized Reference Metals Material.

Specimen Id	Route/Anneal Temp.	Cross sect. Area [mm^2]	Strain $\gamma_{failure}$	Avg. $\gamma_{failure}$ (STD)	Vickers Hardness (300gf)
11-1*†	As-Cast	8.85	0.85	0.90 (0.07)	67
11-2*	As-Cast	8.67	0.86		
11-3*	As-Cast	8.94	1.02		
11-4*‡	As-Cast	8.94	0.86		
18-1*	1A/1100°C	8.91	0.60	0.63 (0.03)	66.42
18-2*	1A/1100°C	8.88	0.66		
17-1*	2C/1100°C	8.94	0.66	0.70 (0.04)	67.74
17-2*	2C/1100°C	8.97	0.75		
24-1*	2C/1100°C	8.85	0.73		66.56
24-2*	2C/1100°C	8.82	0.65		
19-1*	4E/1000°C	8.94	0.59	0.60 (0.015)	67.36
19-2*	4E/1000°C	9.12	0.62		
4-1*	8E/1000°C	8.88	0.62	0.61 (0.005)	67.94
4-2*	8E/1000°C	8.94	0.61		
Avg.			**0.72 (0.13)**		**67.17 (0.57)**

3. 0.2 % Yield Stress Results

The 0.2 % yield stresses for all routes reached a maximum at the recovery stage and a minimum at the recrystallization stage as shown in Figure 78. Yield stress for the as-cast material was found to be strain rate sensitive. 0.2 % yield stress increased with increasing strain rate as shown in Table 17. Yield stresses at the recrystallization temperatures are approximately equal for all routes (average recrystallization yield stress is 147 MPa). The as-cast material has an average yield stress of 104 MPa which is approximately 1/3 less than that of the processed recrystallized material. Figure 79 shows the 0.2 % yield stress as a function of hardness and Figure 80 shows the 0.2% yield stress as a function of the number of passes. This indicates that the yield stress is an increasing function of hardness for all routes. Furthermore, the hardness increases from the as-worked to the recovered stage and then decreases to the recrystallized stage. Note that this decline in the later part of the graph indicates that the 0.2 % yield stress of the ECAE processed material is approaching the value of the as-cast material. This indicates that the 0.2 % yield stress decreases as the grain size increases. 0.2% yield stresses are shown in Tables 15, 16 and 17.

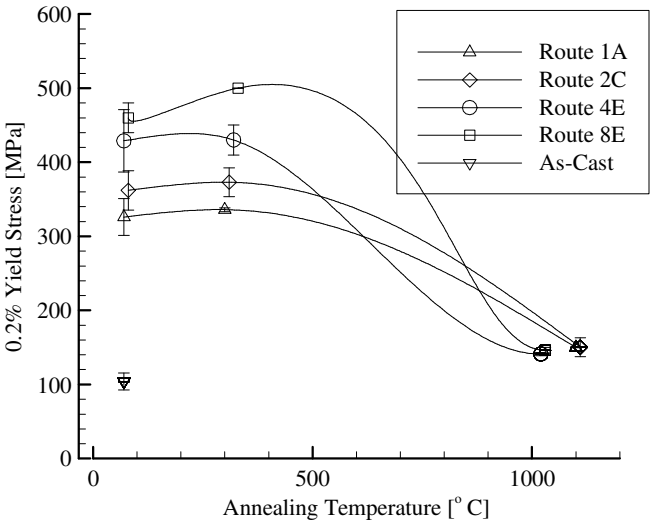

Figure 78. 0.2 % Yield Stress vs Annealing Temperature for Reference Metals As-Cast and ECAE Processed Niobium.

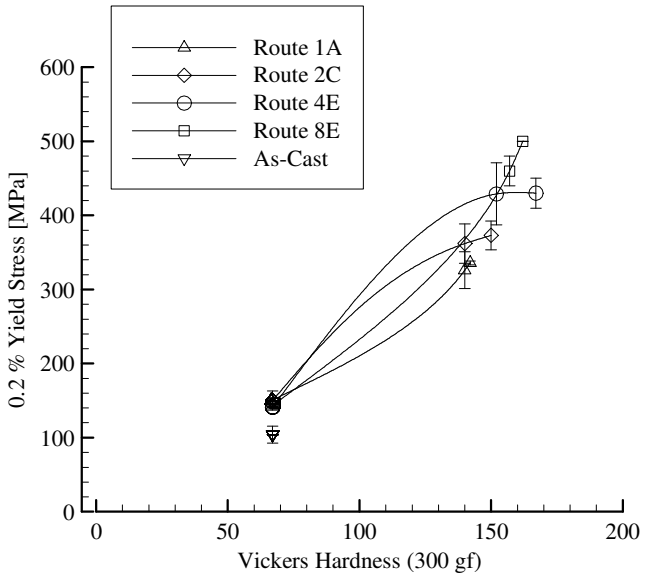

Figure 79. 0.2 % Yield Stress vs Vickers Hardness for Reference Metals As-Cast and ECAE Processed Niobium.

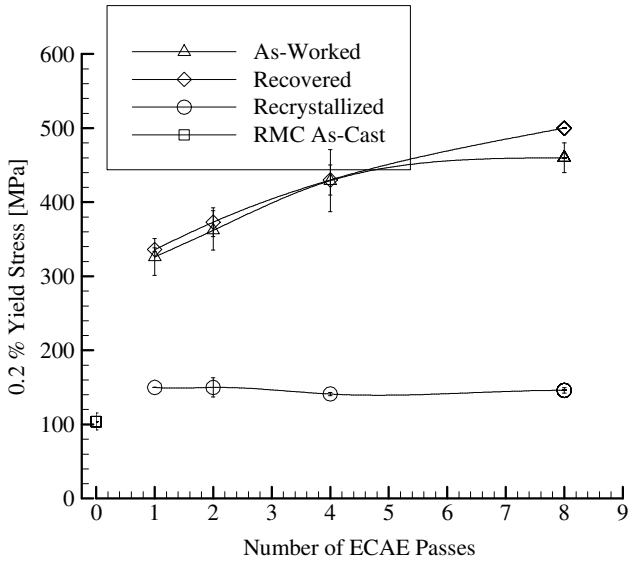

Figure 80. 0.2 % Yield Stress vs Number of Passes for Reference Metals As-Cast and ECAE Processed Niobium.

Table 15. 0.2% Yield Stresses for As-Worked ECAE Processed Reference Metals and Wah Chang Materials.

Specimen Id	Route/Anneal Temp.	Cross sect. Area [mm^2]	0.2% σ_{yield} [MPa]	Avg. 0.2% σ_{yield} [MPa] (STD)	Vickers Hardness (300gf)
3-1B**	1A/As-Work	3.95	340	326 (24.8)	146.68
3-2B**	1A/As-Work	4.08	300		
18-5B**	1A/As-Work	4.11	305		131.58
18-6B**	1A/As-Work	4.05	360		
17-5B**	2C/As-Work	4.07	376	362 (26.4)	137.12
17-6B**	2C/As-Work	4.04	325		
24-4B**	2C/As-Work	3.87	385		142.42
2-3A**	4E/As-Work	3.46	390	429 (41.9)	151.7
2-3B**	4E/As-Work	3.95	490		
2-4A**	4E/As-Work	4.10	390		
2-4B**	4E/As-Work	4.11	445		
4-4A**	8E/As-work	4.01	480	460 (20)	156.92
4-4B**	8E/As-work	4.08	440		
Avg.			**386.6 (59.9)**		**144.4 (8.53)**
WC-2A**	As-Received/As-work	3.96	465	445 (20)	141.68
WC-2B**	As-Received/As-work	4.20	425		
Avg.			**445 (20)**		**141.68**
W2-2A**	4E/As-Work	4.07	420	430 (10)	153.68
W2-2B**	4E/As-Work	4.11	440		
Avg.			**430 (10)**		**153.68**

Table 16. 0.2% Yield Stresses for Recovered ECAE Processed Reference Metals and Wah Chang Materials.

Specimen Id	Route/Anneal Temp.	Cross sect. Area [mm^2]	0.2% σ_{yield} [MPa]	Avg. 0.2% σ_{yield} [MPa] (STD)	Vickers Hardness (300gf)
18-3B**	1A/300°C	4.11	338	336 (2.5)	141.58
18-4B**	1A/300°C	4.07	333		
17-3B**	2C/300°C	4.08	365	373 (19.3)	150.92
17-4B**	2C/300°C	4.08	355		
24-3B**	2C/300°C	4.06	400		150.44
2-1B**	4E/300°C	4.06	430	430 (20.5)	167.26
2-2A**	4E/300°C	4.06	480		
2-2B**	4E/300°C	4.06	460		
4-3B**	8E/300°C	4.05	500	500	161.88
Avg.			**406.8 (59.7)**		**155.4 (10.1)**
WC-1B**	AsRec/300°C	4.16	435	435	142.2
W2-1B**	4E/300°C	4.10	425	425	157.3

Table 17. 0.2% Yield Stresses for Recrystallized Reference Metals Material.

Specimen Id	Route/Anneal Temp.	Cross sect. Area [mm^2]	0.2% σ_{yield} [MPa]	Avg. 0.2% σ_{yield} [MPa] (STD)	Vickers Hardness (300gf)
11-1*†	As-Cast	8.85	93.0	104 (11.5)	67
11-2*	As-Cast	8.67	100.1		
11-3*	As-Cast	8.94	98.9		
11-4*‡	As-Cast	8.94	123.1		
18-1*	1A/1100°C	8.91	149.8	150 (0.1)	66.42
18-2*	1A/1100°C	8.88	150.0		
17-1*	2C/1100°C	8.94	167.0	150 (12.8)	67.74
17-2*	2C/1100°C	8.97	158.4		
24-1*	2C/1100°C	8.85	139.0		66.56
24-2*	2C/1100°C	8.82	136.6		
19-1*	4E/1000°C	8.94	143.0	141 (2.0)	67.36
19-2*	4E/1000°C	9.12	139.0		
4-1*	8E/1000°C	8.88	142.5	146 (3.8)	67.94
4-2*	8E/1000°C	8.94	150.0		
Avg.			**135.0 (22.1)**	**147.53 (9.1) ECAE**	**67.17 (0.57)**

4. Ultimate Tensile Strength Results

The ultimate tensile strengths (UTS) for all routes reached a maximum at the recovery stage and reached a minimum at the recrystallization stage as shown in Figure 81. Maximum stress for the as-cast material was found to be strain rate sensitive. Ultimate tensile strength increased with increasing strain rate as shown in Table 19. The ultimate tensile strengths at the recrystallization temperatures were approximately equal (average recrystallization yield stress is 225 MPa). The as-cast material had an average yield stress of 154 MPa which is approximately 1/3 less than that of the ECAE recrystallized material. The ultimate tensile strength is an increasing function of hardness for all routes as shown in Figure 82. Figure 83 shows the maximum stress as a function of the number of passes. Note that the UTS of the ECAE recrystallized material approaches that of the as-cast material. Ultimate tensile strengths are shown in Tables 18, 19 and 20.

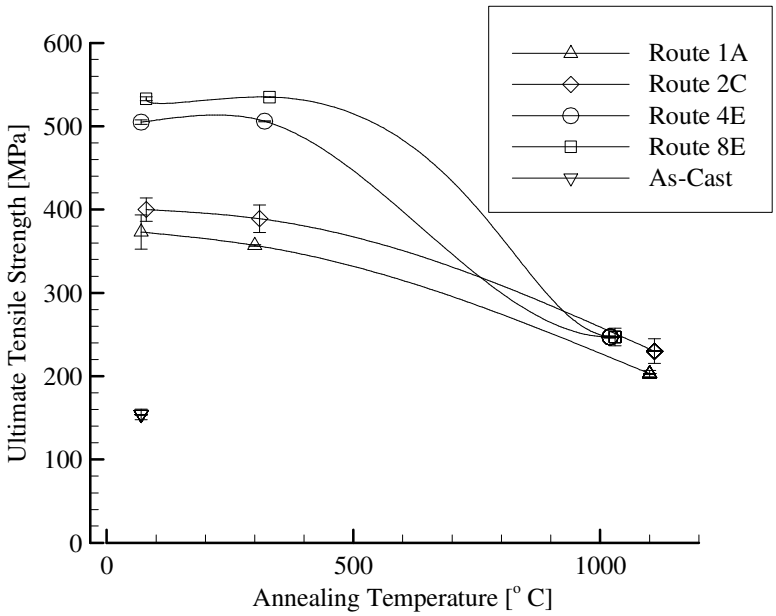

Figure 81. Ultimate Tensile Strength vs Annealing Temperature for Reference Metals As-Cast and ECAE Processed Niobium.

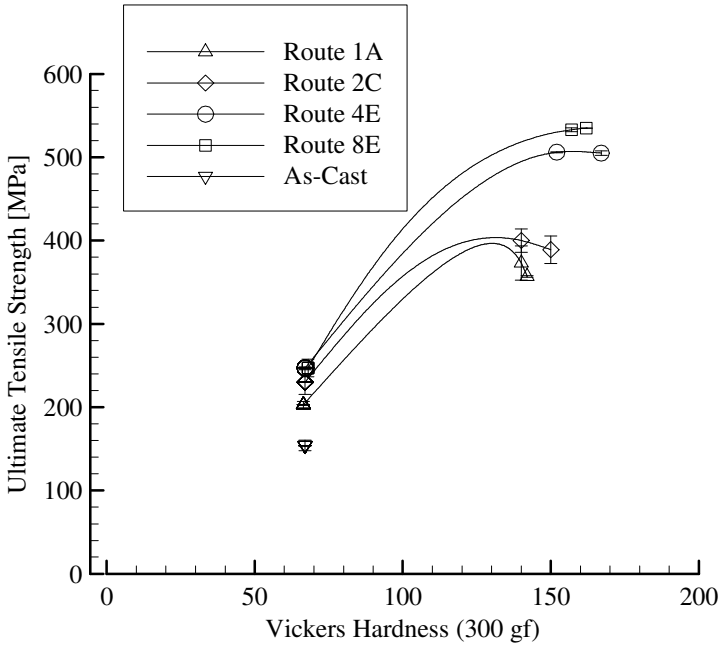

Figure 82. Ultimate Tensile Strength vs Vickers Hardness for Reference Metals As-Cast and ECAE Processed Niobium.

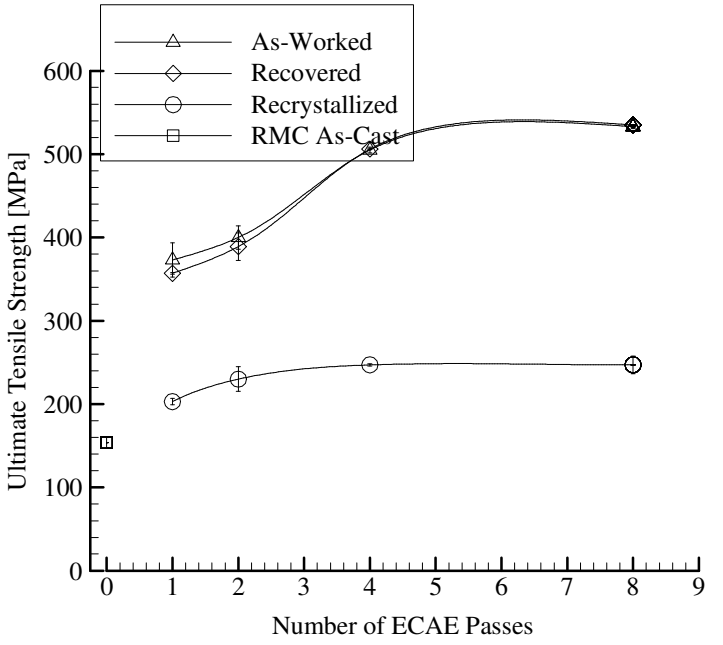

Figure 83. Ultimate Tensile Strength vs Number of Passes for Reference Metals As-Cast and ECAE Processed Niobium.

Table 18. Ultimate Tensile Strength for As-Worked ECAE Processed Reference Metals and Wah Chang Materials.

Specimen Id	Route/Anneal Temp.	Cross sect. Area [mm^2]	σ_{max} [MPa]	Avg. σ_{max} [MPa] (STD)	Vickers Hardness (300gf)
3-1B**	1A/As-Work	3.95	390	373 (20.5)	146.68
3-2B**	1A/As-Work	4.08	370		
18-5B**	1A/As-Work	4.11	340		131.58
18-6B**	1A/As-Work	4.05	390		
17-5B**	2C/As-Work	4.07	410	400 (14.1)	137.12
17-6B**	2C/As-Work	4.04	380		
24-4B**	2C/As-Work	3.87	410		142.42
2-3A**	4E/As-Work	3.46	505	505 (3.5)	151.7
2-3B**	4E/As-Work	3.95	510		
2-4A**	4E/As-Work	4.10	505		
2-4B**	4E/As-Work	4.11	500		
4-4A**	8E/As-work	4.01	530	533 (2.5)	156.92
4-4B**	8E/As-work	4.08	535		
Avg.			**444.2 (67.4)**		**144.4 (8.53)**
WC-2A**	As-Received/As-work	3.96	490	490 (0)	141.68
WC-2B**	As-Received/As-work	4.20	490		
Avg.			**490 (0)**		**141.68**
W2-2A**	4E/As-Work	4.07	480	480 (0)	153.68
W2-2B**	4E/As-Work	4.11	480		
Avg.			**480 (0)**		**153.68**

Table 19. Ultimate Tensile Strength for Recovered ECAE Processed Reference Metals and Wah Chang Materials.

Specimen Id	Route/Anneal Temp.	Cross sect. Area [mm^2]	σ_{max} [MPa]	Avg. σ_{max} [MPa] (STD)	Vickers Hardness (300gf)
18-3B**	1A/300°C	4.11	356	357 (1.0)	141.58
18-4B**	1A/300°C	4.07	358		
17-3B**	2C/300°C	4.08	370	389 (16.4)	150.92
17-4B**	2C/300°C	4.08	388		
24-3B**	2C/300°C	4.06	410		150.44
2-1B**	4E/300°C	4.06	506	506 (0.47)	167.26
2-2A**	4E/300°C	4.06	505		
2-2B**	4E/300°C	4.06	505		
4-3B**	8E/300°C	4.05	535	535	161.88
Avg.			**437.8 (75.0)**		**155.4 (10.1)**
WC-1B**	AsRec/300°C	4.16	480	480	142.2
W2-1B**	4E/300°C	4.10	475	475	157.3

Table 20. Ultimate Tensile Strength for Recrystallized Reference Metals Material.

Specimen Id	Route/Anneal Temp.	Cross sect. Area [mm^2]	σ_{max} [MPa]	Avg. σ_{max} [MPa] (STD)	Vickers Hardness (300gf)
11-1*†	As-Cast	8.85	146	154 (6.3)	67
11-2*	As-Cast	8.67	156		
11-3*	As-Cast	8.94	151		
11-4*‡	As-Cast	8.94	163		
18-1*	1A/1100°C	8.91	199	203 (4.0)	66.42
18-2*	1A/1100°C	8.88	207		
17-1*	2C/1100°C	8.94	231	230 (14.8)	67.74
17-2*	2C/1100°C	8.97	252		
24-1*	2C/1100°C	8.85	224		66.56
24-2*	2C/1100°C	8.82	211		
19-1*	4E/1000°C	8.94	248	247 (1.5)	67.36
19-2*	4E/1000°C	9.12	245		
4-1*	8E/1000°C	8.88	237	247 (10.5)	67.94
4-2*	8E/1000°C	8.94	258		
Avg.			**209.1 (38.7)**	**231.2ECAE (19.2)**	**67.17 (0.57)**

5. Toughness Results

The toughness results for ECAE processed niobium show that toughness is an increasing function of strain at the as-worked and recovered stages as shown if Figure 84. Recrystallized toughness for the ECAE processed material (average of 109.2 MJoule/m^3) is approximately that of the as-cast material. Figure 85 shows toughness as a function of hardness and Figure 86 shows the toughness as a function of the number of passes. Toughness values are shown in Tables 21, 22 and 23.

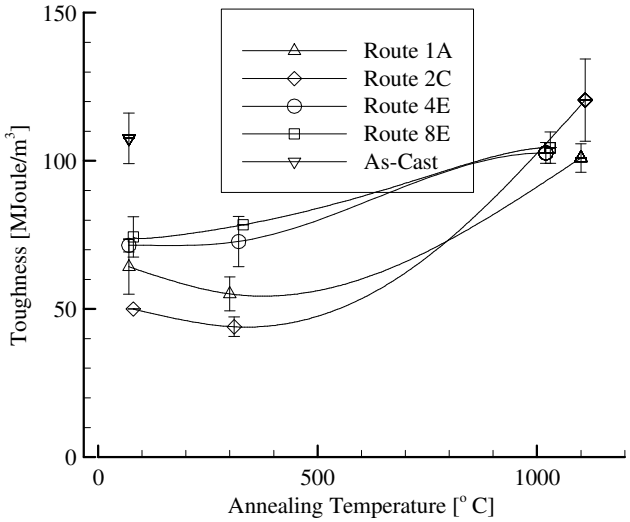

Figure 84. Toughness vs Annealing Temperature for Reference Metals As-Cast and ECAE Processed Niobium.

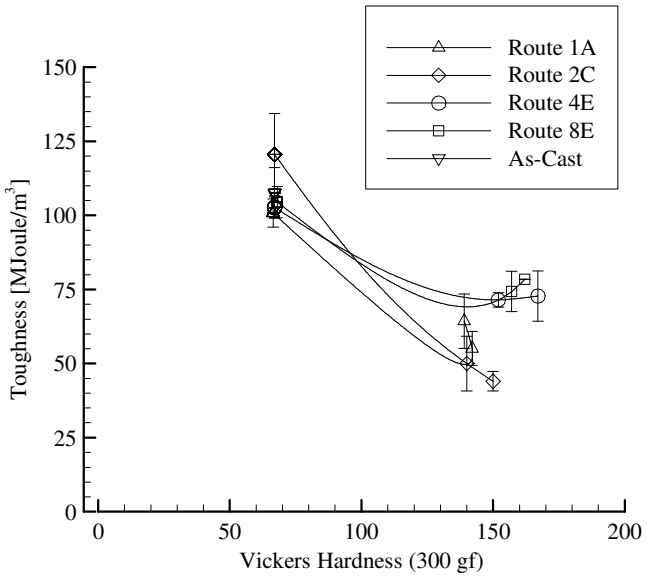

Figure 85. Toughness vs Vickers Hardness for Reference Metals As-Cast and ECAE Processed Niobium.

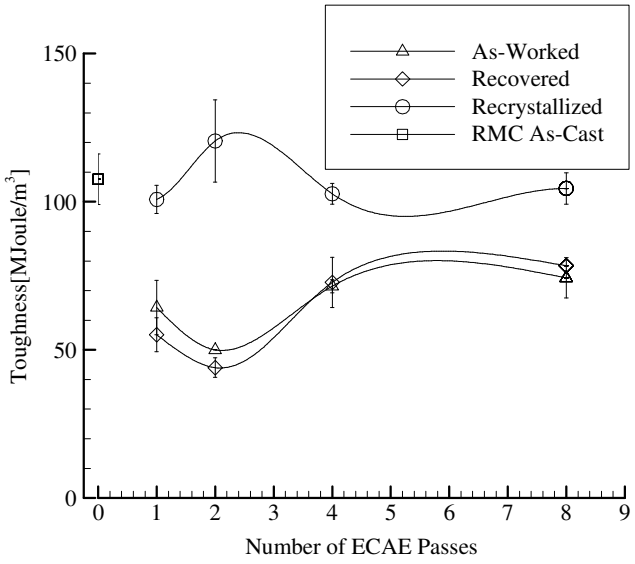

Figure 86. Toughness vs Number of Passes for Reference Metals As-Cast ECAE and Processed Niobium.

Table 21. Toughness for As-Worked ECAE Processed Reference Metals and Wah Chang Materials.

Specimen Id	Route/Anneal Temp.	Cross sect. Area [mm^2]	Toughness [$MJoule/m^3$]	Avg. Toughness [$MJoule/m^3$] (STD)	Vickers Hardness (300gf)
3-1B**	1A/As-Work	3.95	80	64.3 (9.2)	146.68
3-2B**	1A/As-Work	4.08	60		
18-5B**	1A/As-Work	4.11	57		131.58
18-6B**	1A/As-Work	4.05	60		
17-5B**	2C/As-Work	4.07	50	50 (0)	137.12
17-6B**	2C/As-Work	4.04	50		
24-4B**	2C/As-Work	3.87	50		142.42
2-3A**	4E/As-Work	3.46	75	71.5 (2.2)	151.7
2-3B**	4E/As-Work	3.95	70		
2-4A**	4E/As-Work	4.10	70		
2-4B**	4E/As-Work	4.11	70		
4-4A**	8E/As-work	4.01	67.5	74.3 (6.8)	156.92
4-4B**	8E/As-work	4.08	81		
Avg.			**64.7 (10.6)**		**144.4 (8.53)**
WC-2A**	As-Received/As-work	3.96	80	80 (0)	141.68
WC-2B**	As-Received/As-work	4.20	80		
Avg.			**80 (0)**		**141.68**
W2-2A**	4E/As-Work	4.07	75	75 (0)	153.68
W2-2B**	4E/As-Work	4.11	75		
Avg.			**75 (0)**		**153.68**

Table 22. Toughness for Recovered ECAE Processed Reference Metals and Wah Chang Materials.

Specimen Id	Route/Anneal Temp.	Cross sect. Area [mm^2]	Toughness [$MJoule/m^3$]	Avg. Toughness [$MJoule/m^3$] (STD)	Vickers Hardness (300gf)
18-3B**	1A/300°C	4.11	49.4	55.1 (5.7)	141.58
18-4B**	1A/300°C	4.07	60.8		
17-3B**	2C/300°C	4.08	40	44 (3.3)	150.92
17-4B**	2C/300°C	4.08	44		
24-3B**	2C/300°C	4.06	48		150.44
2-1B**	4E/300°C	4.06	83.2	72.8 (8.5)	167.26
2-2A**	4E/300°C	4.06	72.8		
2-2B**	4E/300°C	4.06	62.5		
4-3B**	8E/300°C	4.05	78.4	78.4 (0)	161.88
Avg.			**59.9 (14.8)**		**155.4 (10.1)**
WC-1B**	AsRec/300°C	4.16	80	80	142.2
W2-1B**	4E/300°C	4.10	70	70	157.3

Table 23. Toughness for Recrystallized Reference Metals Materials.

Specimen Id	Route/Anneal Temp.	Cross sect. Area [mm^2]	Toughness [$MJoule/m^3$]	Avg. Toughness [$MJoule/m^3$] (STD)	Vickers Hardness (300gf)
11-1*†	As-Cast	8.85	102	107.6 (8.55)	67
11-2*	As-Cast	8.67	103		
11-3*	As-Cast	8.94	122.4		
11-4*‡	As-Cast	8.94	103		
18-1*	1A/1100°C	8.91	96	100.8 (4.8)	66.42
18-2*	1A/1100°C	8.88	105.6		
17-1*	2C/1100°C	8.94	118.8	120.5 (13.9)	67.74
17-2*	2C/1100°C	8.97	142.5		
24-1*	2C/1100°C	8.85	116.8		66.56
24-2*	2C/1100°C	8.82	104		
19-1*	4E/1000°C	8.94	106.2	102.7 (3.5)	67.36
19-2*	4E/1000°C	9.12	99.2		
4-1*	8E/1000°C	8.88	99.2	104.5 (5.3)	67.94
4-2*	8E/1000°C	8.94	109.8		
Avg.			**109.2 (11.9)**	**109.8 (13.0) ECAE**	**67.17 (0.57)**

6. Strain Rate Sensitivity

Reference Metals as-cast material was tested at three different strain rates to determine strain rate sensitivity. Results show that 0.2 % yield stress and ultimate tensile strength are increasing functions of strain. Although it appears that failure strain is also strain rate sensitive when looking at the stress/strain curves (see figure 87), measuring calipers disputes this. This appearance of failure strain sensitivity to strain rate is due to positioning of the extensometer. Early necking made it difficult to place the extensometer in the appropriate position. Figure 88 shows a close up of the onset of plastic strain for various strain rates. Ultimate tensile strength values are 146, 153 and 163 for strain rates 10^{-5}, 10^{-3} and 10^{-2}respectively as shown in Figure 89. 0.2 % yield stress values are 94, 100 and 123 for strain rates 10^{-5}, 10^{-3} and 10^{-2} respectively as shown in Figure 90.

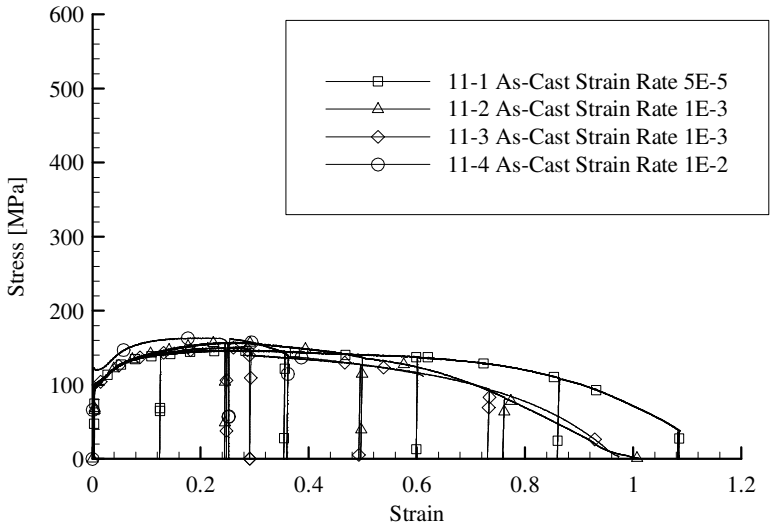

Figure 87. Stress/Strain Graphs of Reference Metals As-Cast Material at Various Strain Rates.

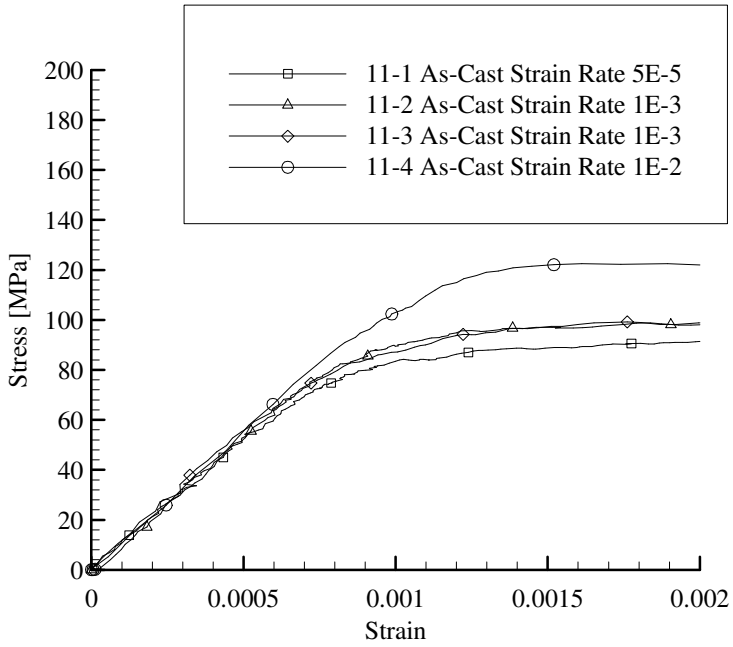

Figure 88. Close Up View of Reference Metals As-Cast Material Showing Strain Rate Sensitivity.

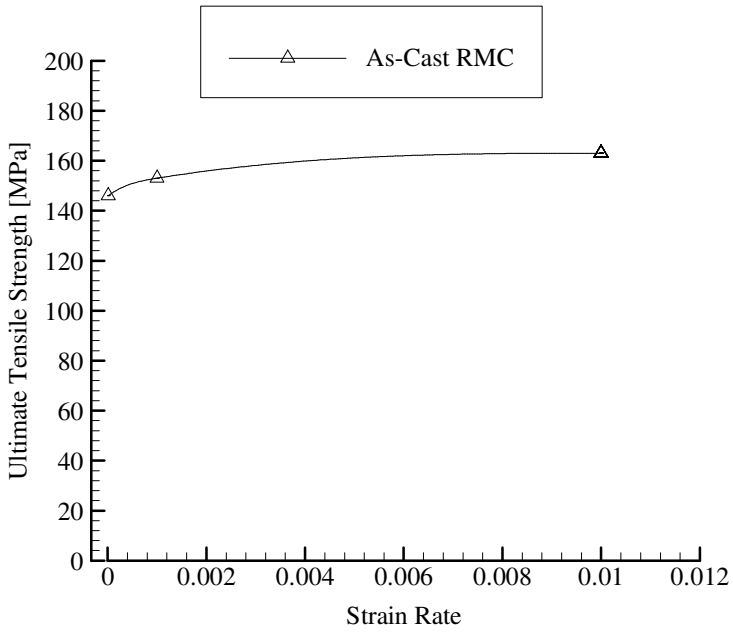

Figure 89. Ultimate Tensile Strength at Strain Rates of 10^{-5}, 10^{-3} and 10^{-2}.

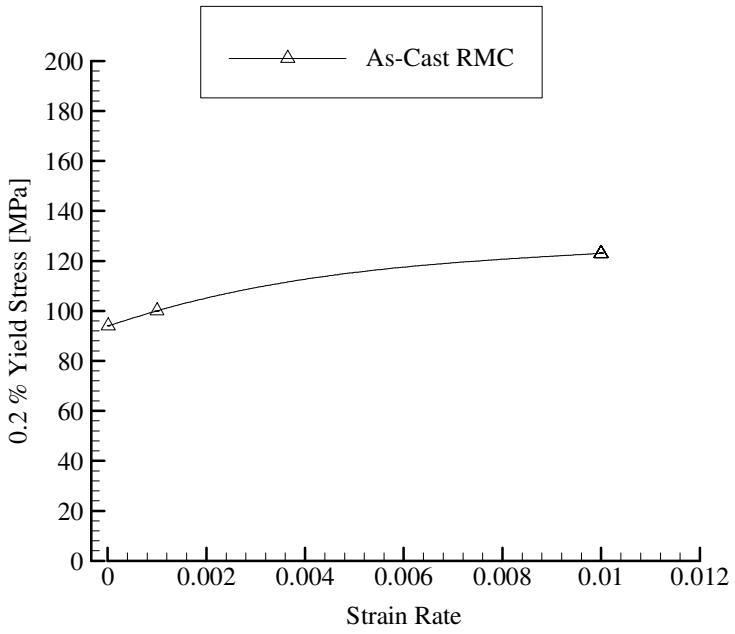

Figure 90. 0.2 % Yield Stress at Strain Rates of 10^{-5}, 10^{-3} and 10^{-2}.

Stress/strain curves for recrystallize material are shown in Figures 91, 92, 93, 94 and 95. Stress/strain curves for worked material are shown in Figures 96, 97, 98, 99, 100, 101 and 102. Stress/strain curves for recovered material are shown in Figures 103, 104, 105, 106, 107 and 108. Stress/strain curves for the Wah Chang material are shown in Figures 109, 110, 111 and 112.

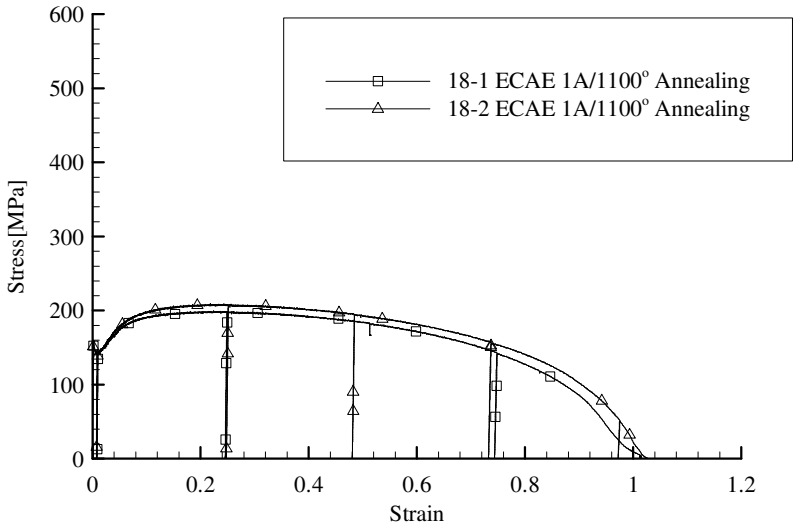

Figure 91. Stress/Strain Graphs of Reference Metals ECAE/1A Processed Niobium Annealed at 1100° C (Samples 18-1and 18-2).

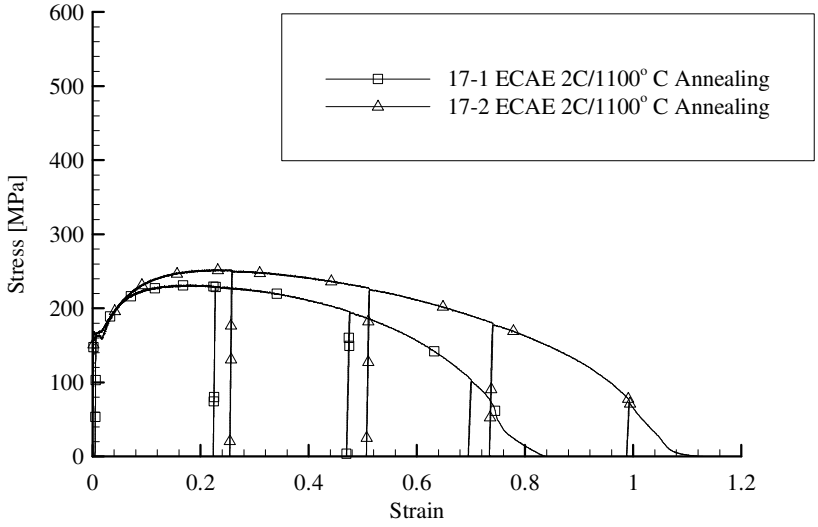

Figure 92. Stress/Strain Graphs of Reference Metals ECAE/2C Processed Niobium Annealed at 1100° C (Samples 17-1and 17-2).

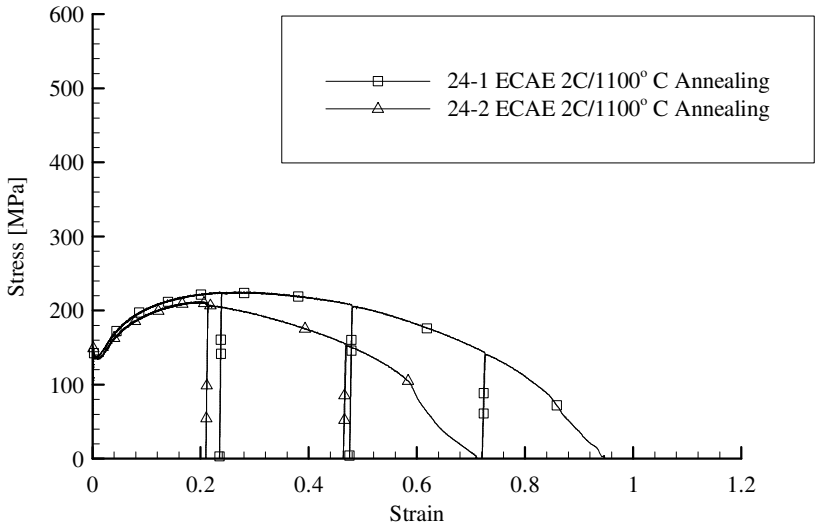

Figure 93. Stress/Strain Graphs of Reference Metals ECAE/2C Processed Niobium Annealed at 1100°C (Samples 24-1and 24-2).

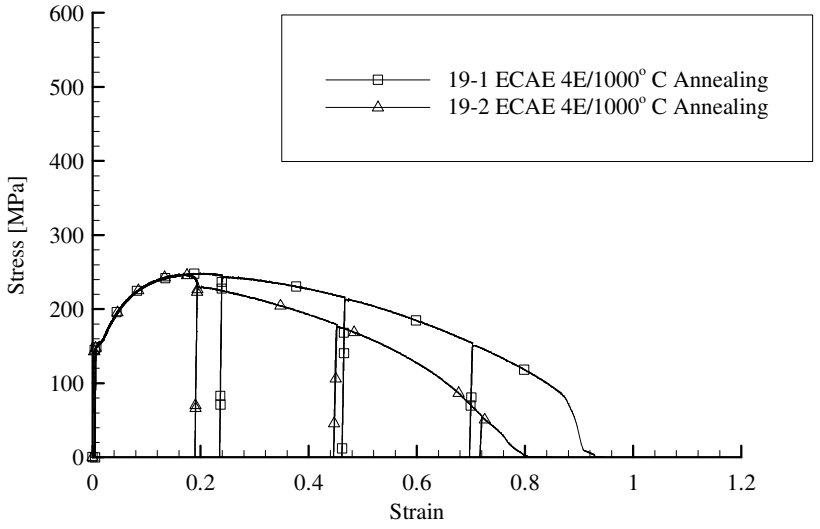

Figure 94. Stress/Strain Graphs of Reference Metals ECAE/4E Processed Niobium Annealed at 1000° C (Samples 19-1and 19-2).

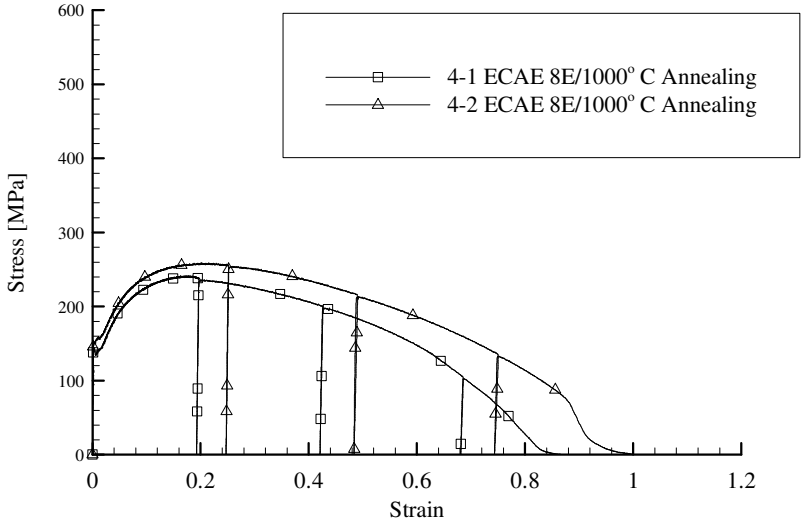

Figure 95. Stress/Strain Graphs of Reference Metals ECAE/8E Processed Niobium Annealed at 1000° C (Samples 4-1and 4-2).

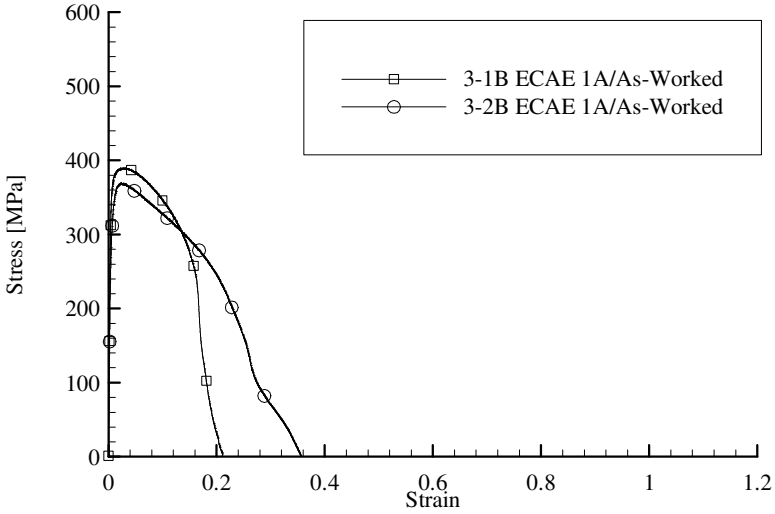

Figure 96. Stress/Strain Graphs of Reference Metals ECAE/1A As-Worked Processed Niobium (Samples 3-1B and 3-2B).

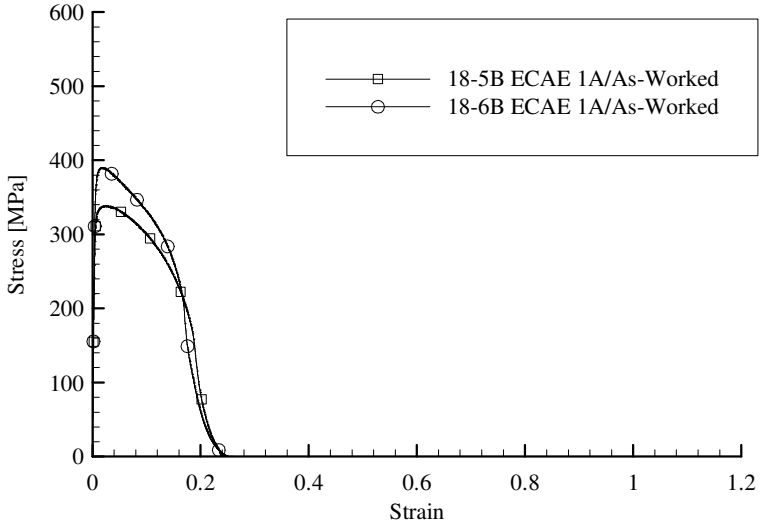

Figure 97. Stress/Strain Graphs of Reference Metals ECAE/1A As-Worked Processed Niobium (Samples 18-5B and 18-6B).

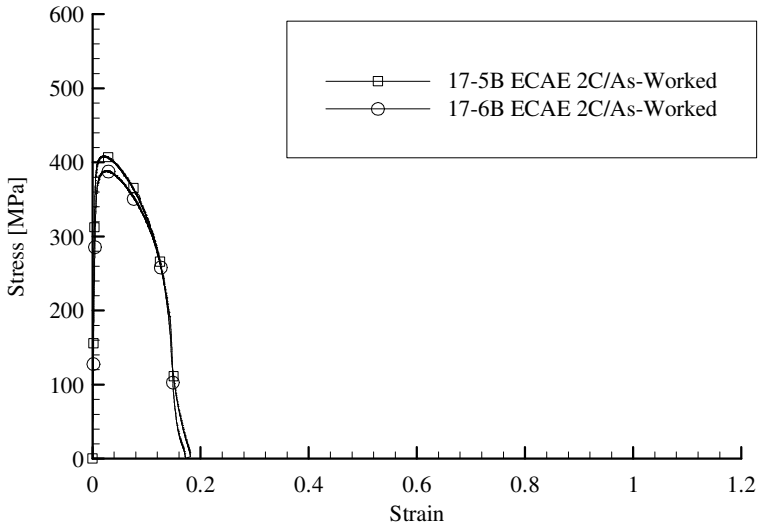

Figure 98. Stress/Strain Graphs of Reference Metals ECAE/2C As-Worked Processed Niobium (Samples 17-5B and 17-6B).

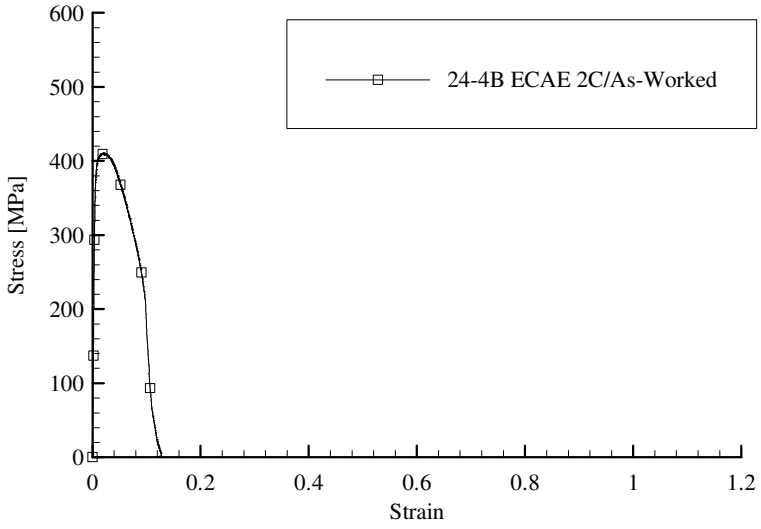

Figure 99. Stress/Strain Graphs of Reference Metals ECAE/2C As-Worked Processed Niobium (Sample 24-4B).

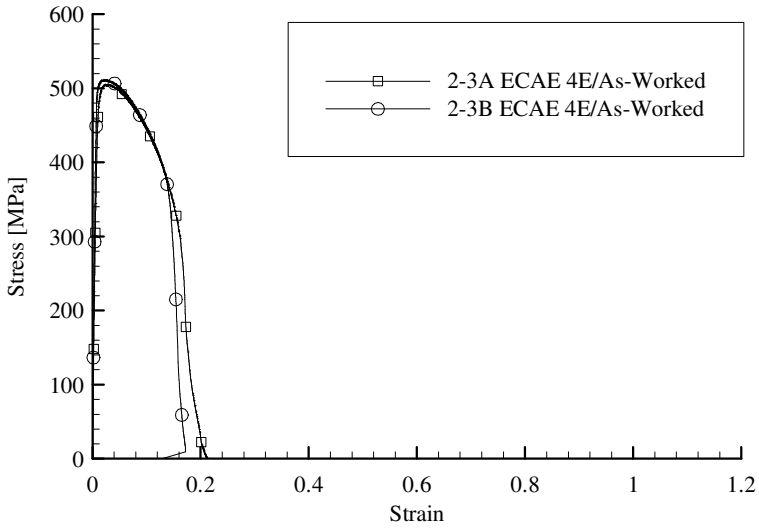

Figure 100. Stress/Strain Graphs of Reference Metals ECAE/4E As-Worked Processed Niobium (Samples 2-3A and 2-3B).

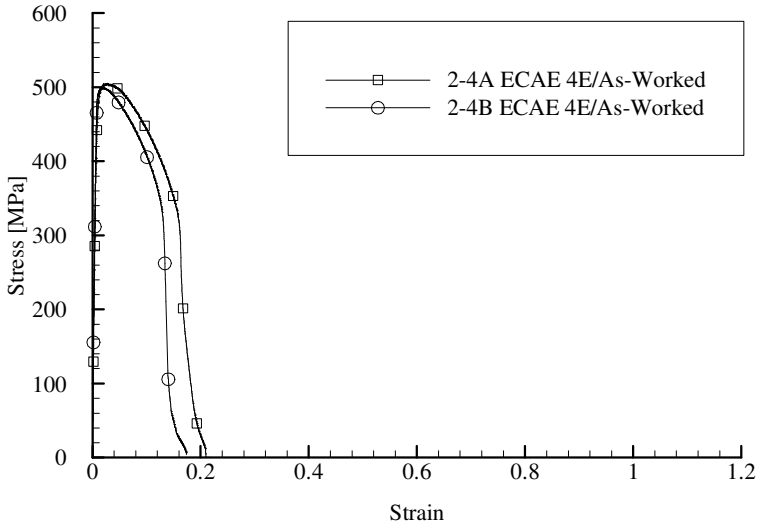

Figure 101. Stress/Strain Graphs of Reference Metals ECAE/4E As-Worked Processed Niobium (Samples 2-4A and 2-4B).

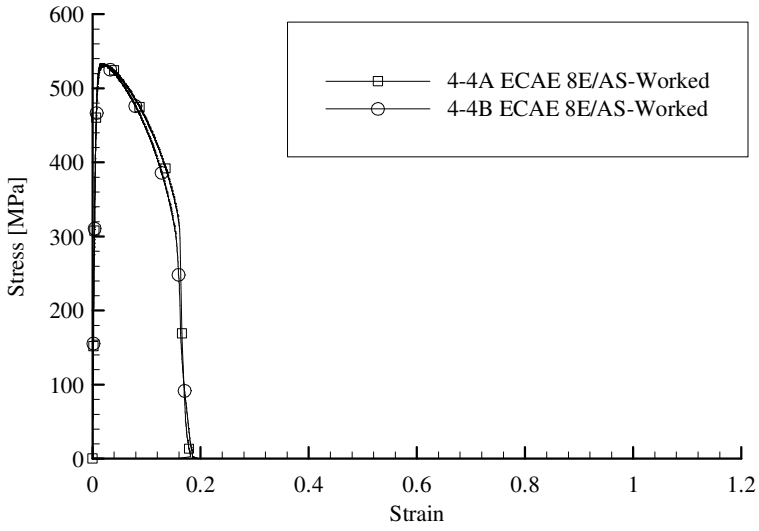

Figure 102. Stress/Strain Graphs of Reference Metals ECAE/8E As-Worked Processed Niobium (Samples 4-4A and 4-4B).

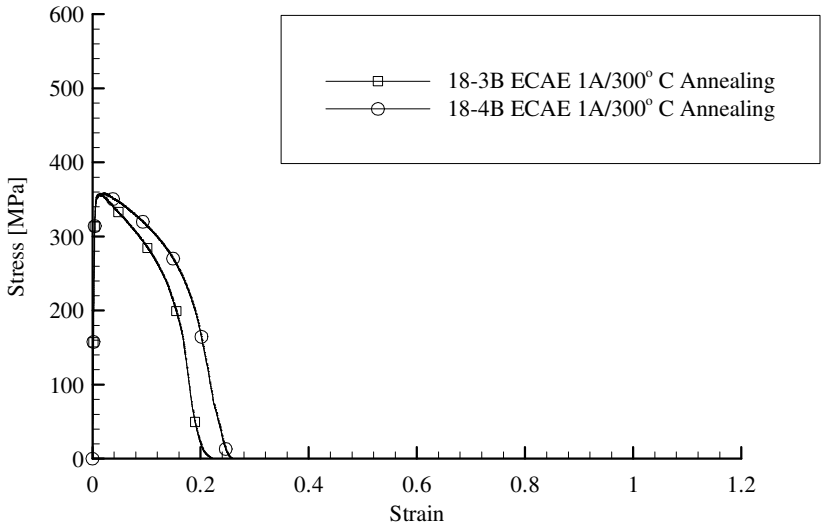

Figure 103. Stress/Strain Graphs of Reference Metals ECAE/1A Processed Niobium Annealed at 300° C (Samples 18-3B and 18-4B).

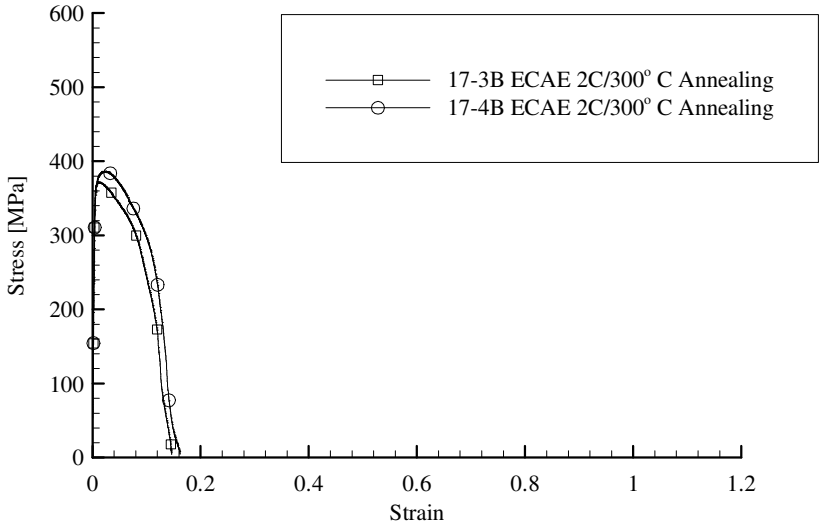

Figure 104. Stress/Strain Graphs of Reference Metals ECAE/2C Processed Niobium Annealed at 300° C (Samples 17-3B and 17-4B).

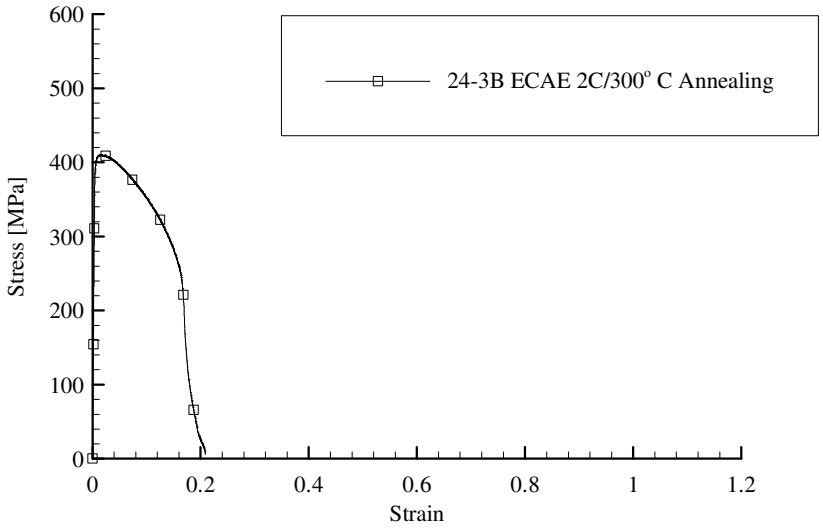

Figure 105. Stress/Strain Graphs of Reference Metals ECAE/2C Processed Niobium Annealed at 300° C (Sample 24-3B).

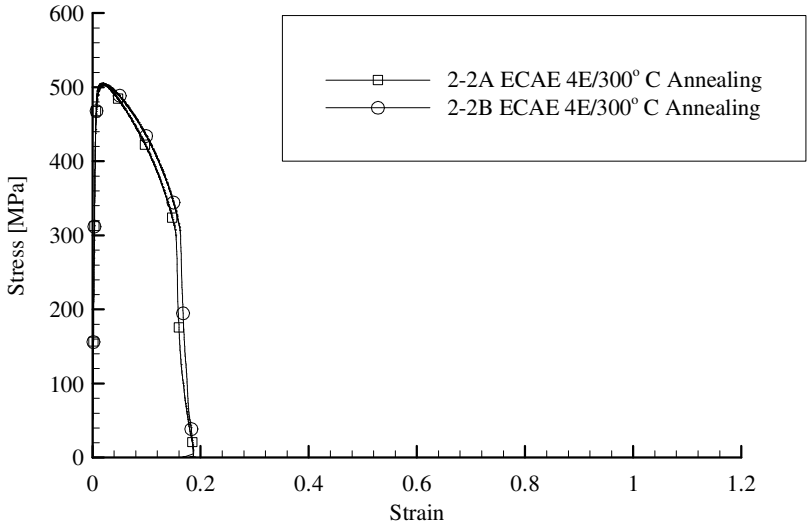

Figure 106. Stress/Strain Graphs of Reference Metals ECAE/4E Processed Niobium Annealed at 300° C (Samples 2-2A and 2-2B).

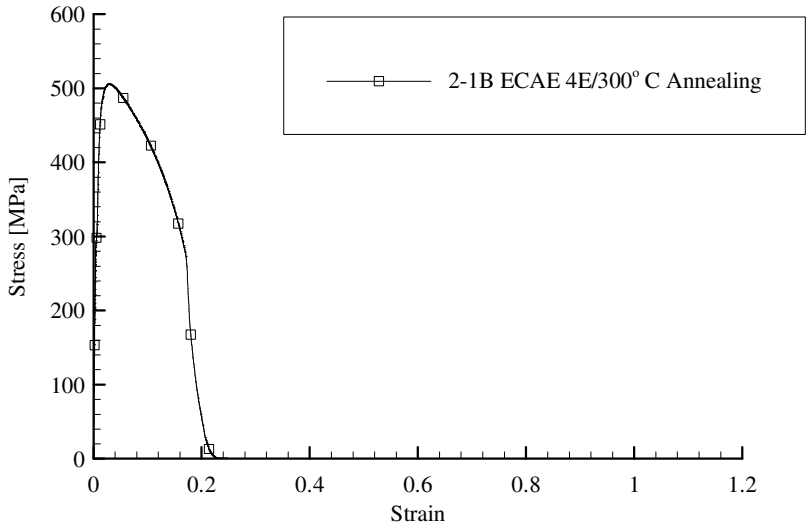

Figure 107. Stress/Strain Graph of Reference Metals ECAE/4E Processed Niobium Annealed at 300° C (Sample 2-1B).

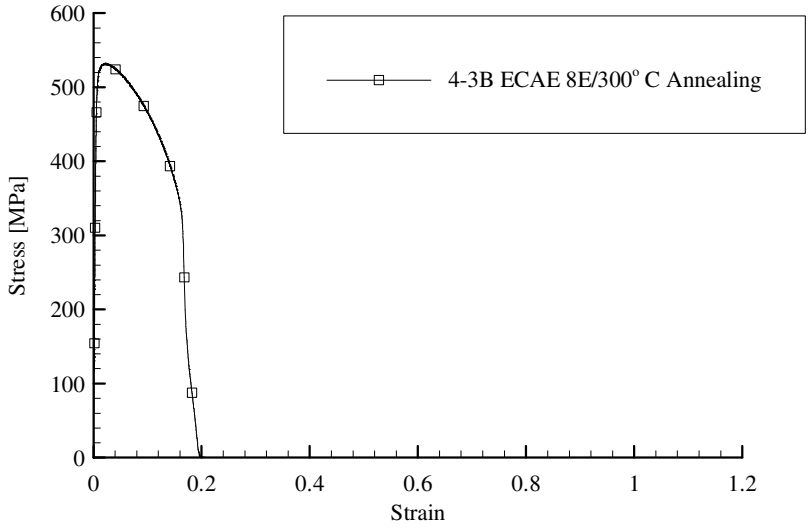

Figure 108. Stress/Strain Graph of Reference Metals ECAE/8E Processed Niobium Annealed at 300° C. (Sample 4-3B).

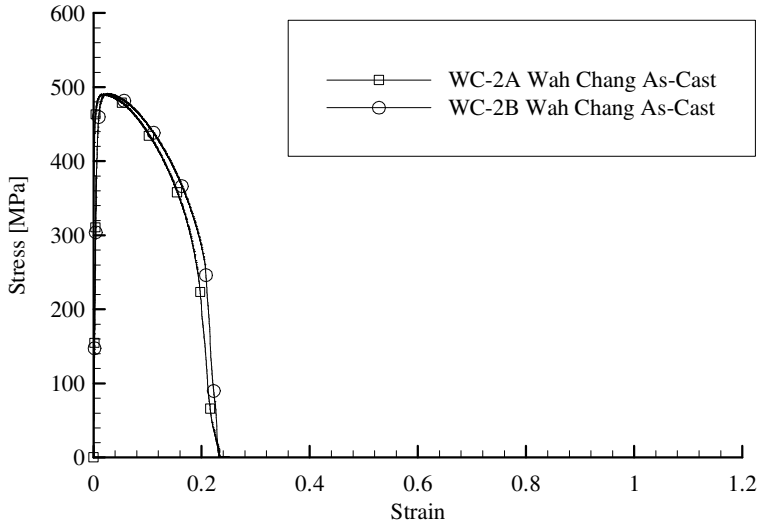

Figure 109. Stress/Strain Graphs of Wah Chang As-Cast Niobium.

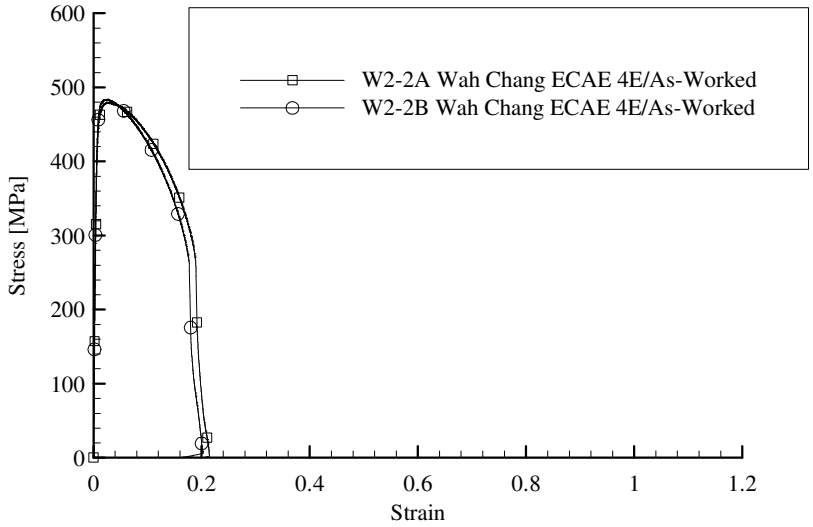

Figure 110. Stress/Strain Graphs of Wah Chang ECAE/4E As-Worked Processed Niobium.

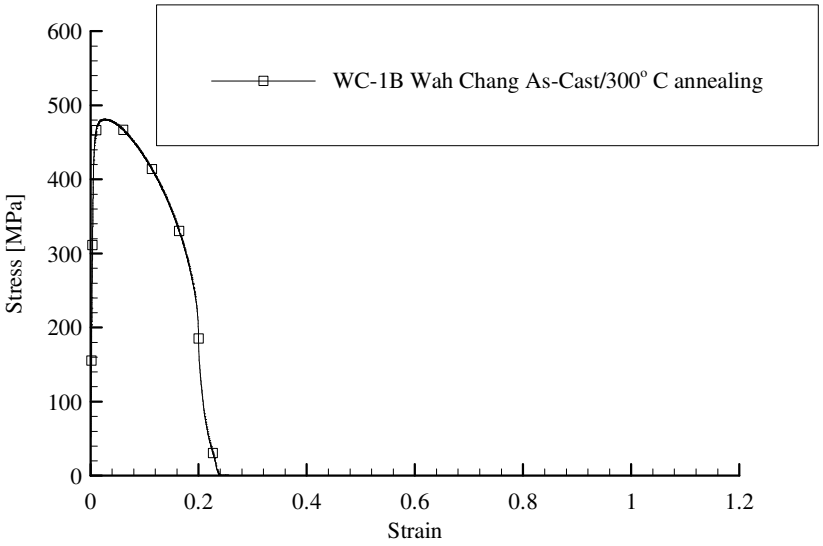

Figure 111. Stress/Strain Graph of Wah Chang As-Cast Niobium Annealed at 300° C.

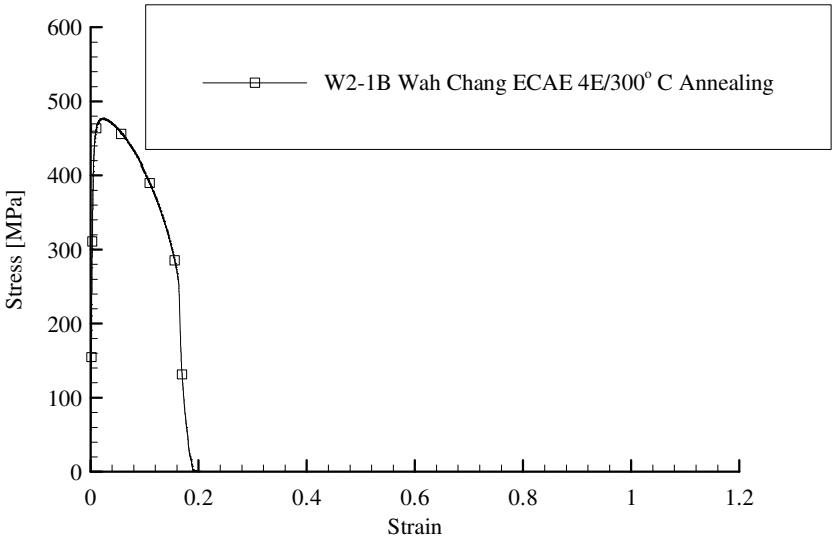

Figure 112. Stress/Strain Graph of Wah Chang ECAE/4E Processed Niobium Annealed at 300° C.

I. Transmission Electron Microscopy

TEM was utilized to study the effects of ECAE to break down the microstructure to grain fragments (sub-grains). Cell structure morphology was analyzed for sub-grain shapes, sizes and boundary angles. This section analyzed one sample from each of the 1A, 2C and 4E as-worked processed materials. Results show that cell structures developed after one pass. Materials that underwent routes 1A and 2C developed long and narrow sub-cells while the 4E material developed more fragmented sub-grains. Cell widths ranged from 50 μm to 400μm with route 4E producing smaller structures. Sub-grain boundary angles were small for 1 pass and increased for 2C and 4E passes indicating crystal rotation. Dislocation densities were calculated in the following manner. A representative dislocation count (N) was taken for five grains per photo and plugged into the following equation. The average dislocation density was then computed along with the standard deviation and plotted in Figure 113. Dislocation density increased dramatically after the first pass and continued to level off thereafter.

$$\rho = \frac{2N}{Lt} \qquad (34)$$

ρ = Dislocation density [number of dislocations/cm^2]

N = Number of dislocations counted

L = 1cm/40,000 (40,000 is magnification)

t = thickness (estimated at 0.1 μm)

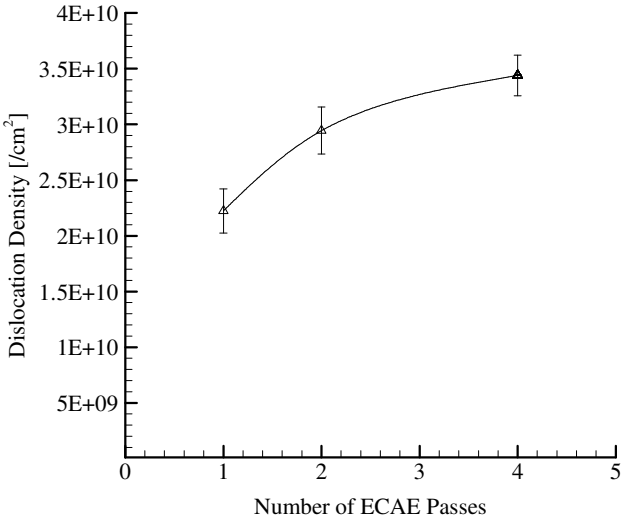

Figure 113. Dislocation Density of ECAE Processed RM Niobium.

Figure 114 shows bright-field and diffraction TEM photos of Reference Metals niobium after one pass of ECAE processing. Sub-grains are clearly produced and are long and narrow with width's approximately 200 ± 100 μm. Diffraction patterns for several side by side sub grains are shown in Figures c, d and e. Analysis of the crystal orientations indicates that boundaries have low angle. Figures 109 c and d are diffraction patterns in the [133] direction. There is a small angle of rotation between the two crystals of 2.4^{o} around the [133] axis. Figure e) shows the diffraction pattern in the [155] direction. The angle between the [133] crystal and the [155] crystal is 5.2^{o}.

Figure 115 shows bright-field and diffraction TEM photos of Reference Metals niobium after two passes of ECAE processing. Sub-grains are clearly produced and are long and narrow with width's approximately 200 ± 100 μm which is a similar pattern in the one pass material. Diffraction patterns for several side by side sub grains are shown in Figures c, d and e. All three of the crystals are in the [011] orientation and show rotation about the [011] direction. These rotations are larger than that of the one pass material as described in the figure captioned.

Figure 116 shows bright-field and diffraction TEM photos of Reference Metals niobium after four pass of ECAE processing. Sub-grains are clearly produced and are more broken up with a wider range of widths. Diffraction patterns for several side by side sub grains are shown in Figures c, d and e. Analysis of the crystal orientations indicates that boundaries have larger angles than that of the one and two pass material. Figures c and d are diffraction patterns in the [011] direction. There is a small angle of rotation between the two crystals of 20.8^{o} around the [011] axis. Figure e shows the diffraction pattern in the [133] direction. The angle between the [011] crystal and the [133] crystal is 25.3^{o}.

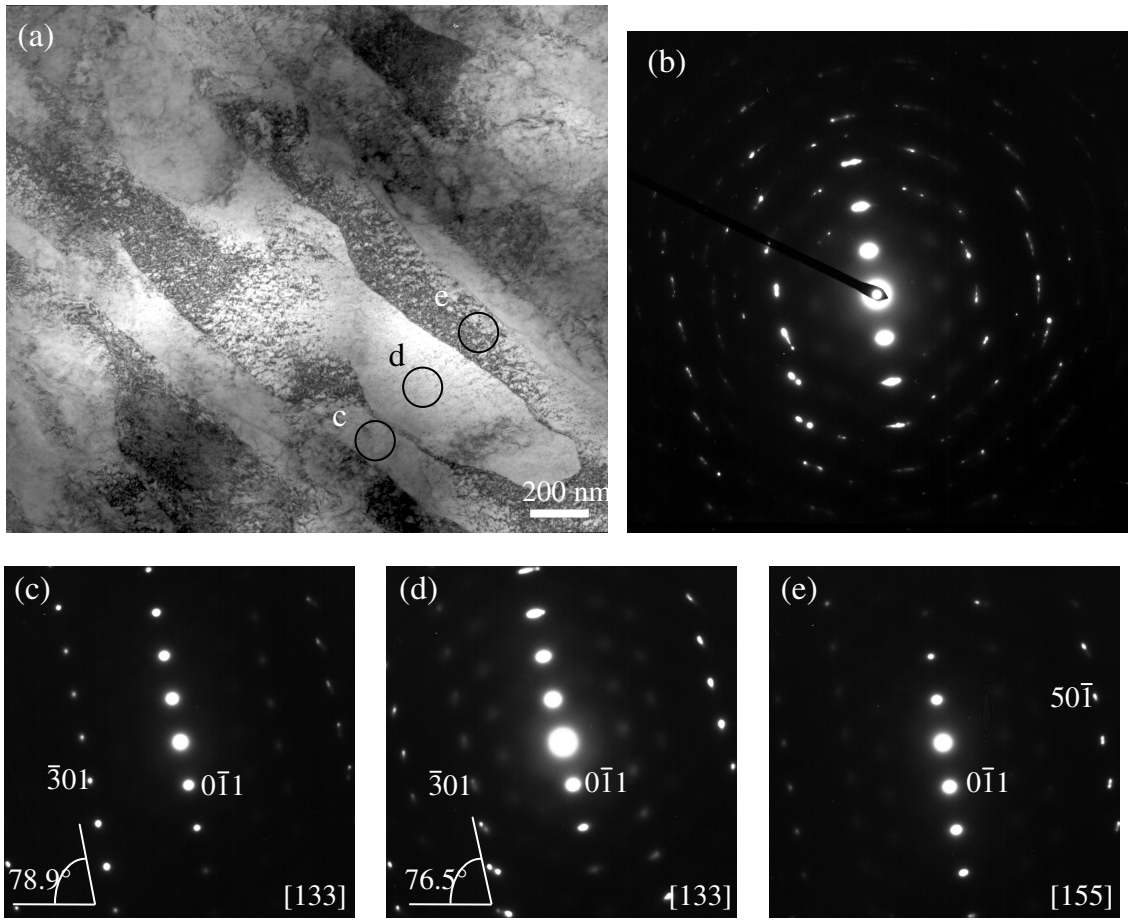

Figure 114. Bright -Field and Selected-Area Electron Diffraction Patterns (SAED) for 1A ECAE Processed Material.

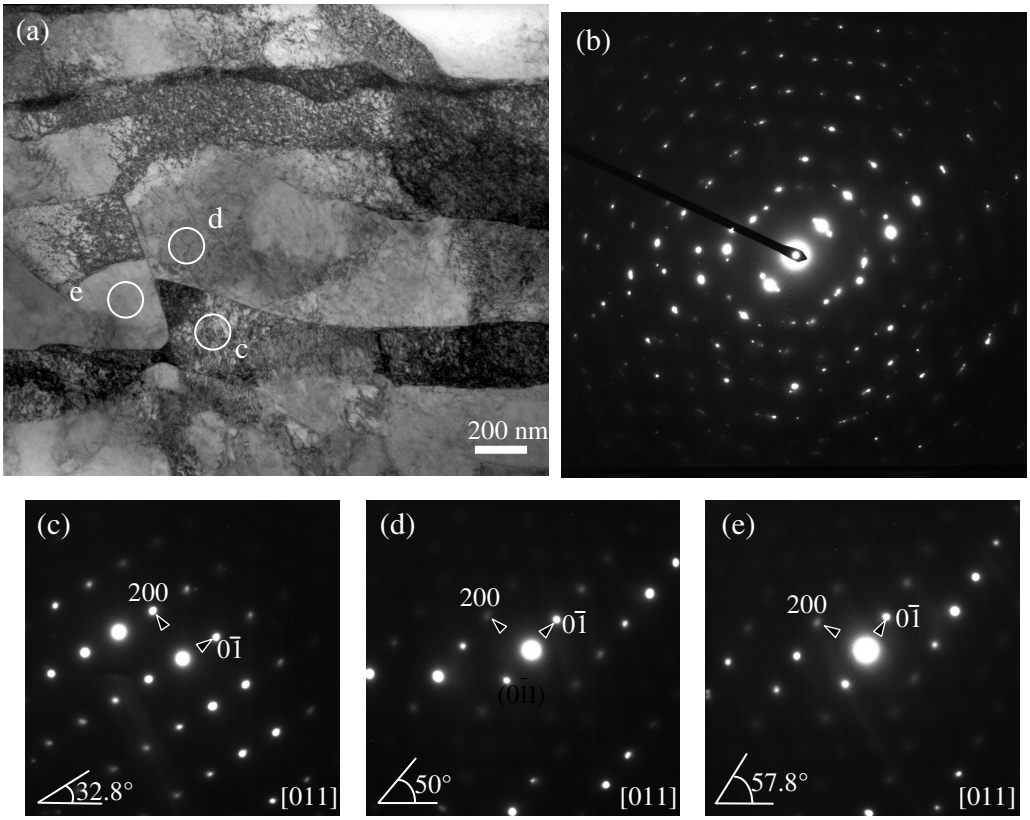

Figure 115. Bright -Field and Selected-Area Electron Diffraction Patterns (SAED) for 2C ECAE Processed Material.

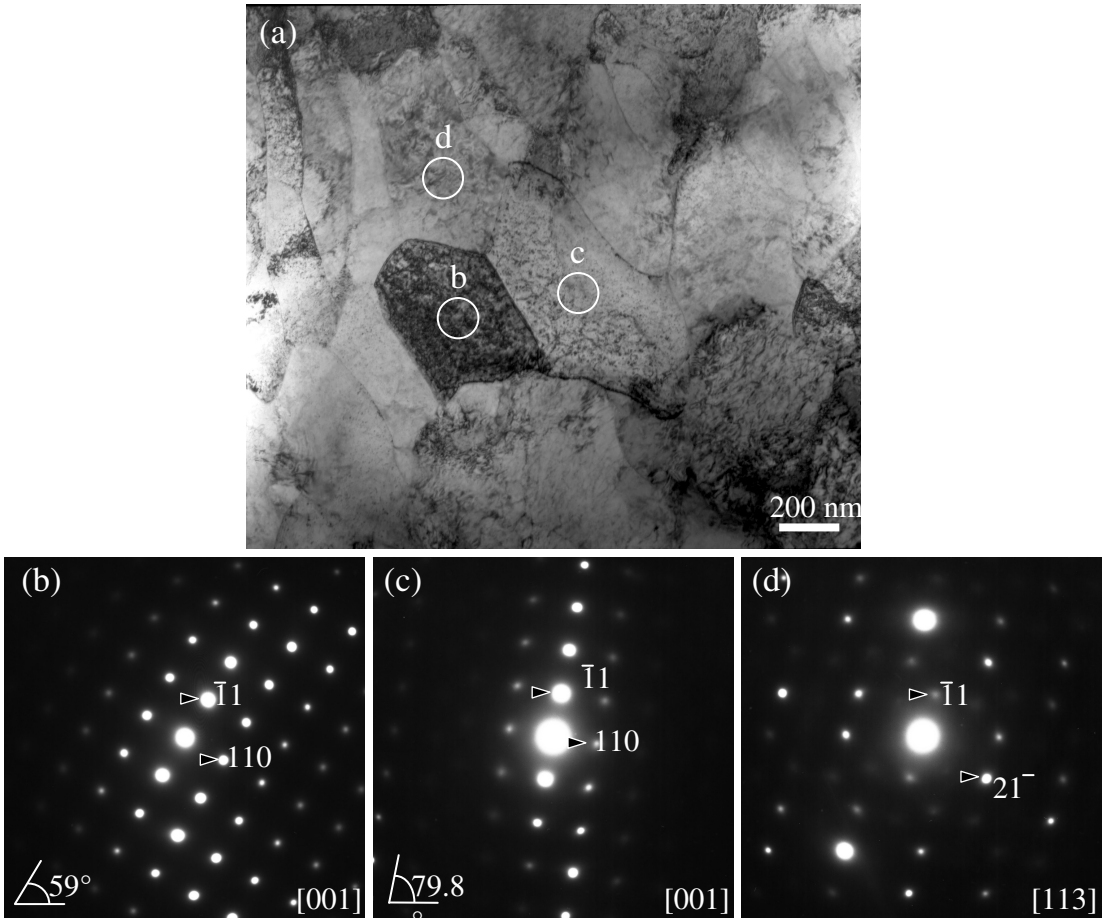

Figure 116. Bright -Field and Selected-Area Electron Diffraction Patterns (SAED) for 4E ECAE Processed Material.

CHAPTER V

DISCUSSION

A. Introduction

The goal of this research was to determine the effectiveness of ECAE/Annealing to produce a fine grained/homogenized microstructure in pure niobium from two sources, Reference Metals and Wah Chang. Tests included Brinell hardness (H_B), Rockwell b hardness (H_{Rb}), Vickers hardness (H_V), optical microscopy, transmission electron microscopy and tensile tests. Recrystallized grain size (GS_R) and homogeneity (HGS_R)are the primary dependent variables because isotropic plastic deformation is highly dependent on these characteristics. Secondary dependent variables are strain hardening measurements (H_B, H_{Rb} and H_V), annealing hardness measurements (H_{AV}), deformation banding (DB), strain failure ($\gamma_{failure}$), 0.2% yield strength (YS), maximum stress (σ_{max}) and toughness (T). Independent variables include annealing temperature (T_A), strain (γ), number of ECAE passes (N), route (R), initial grain size (GS_i) and Vickers hardness (H_V). More abstract dependent variables such as grain morphology and deformation banding will be discussed in terms of patterns and shapes with route, strain, trends, homogeneity and reproducibility kept in mind.

Primary Dependent Variables: GS_R, HGS_R

Secondary Dependent Variables: H_B, H_{Rb}, H_V, H_{AV}, DB, $\gamma_{failure}$, YS, σ_{max}, T

Independent Variables: T_A, γ, N, H_V, R, GS_i

Before explaining the results of this research, expected trends of dependent variables are noted in bullet form:

1. Hardness (H_B, H_{Rb}, H_V) is expected to increase with increasing strain (strain hardening).
2. Hardness (H_{AV}) is expected to decrease with increasing annealing temperature (recrystallization).
3. Recrystallization temperature is expected to decrease with increasing strain.
4. Deformation banding (DB) is expected to be more homogeneous with increasing strain.
5. Recrystallized grain size (GS_R) is expected to decrease with increasing strain.
6. Recrystalized grain size (GS_R) is expected to increase with increasing annealed temperature (grain growth).
7. Grain size homogeneity (HGS_R) is expected to become more homogeneous with increasing strain.
8. Yield strength (YS) is expected to decrease from as-worked to recrystallized state.

9. Ultimate tensile strength (σ_{max}) is expected to decrease from as-worked to recrystallized state.

10. Failure strains ($\gamma_{failure}$) is expected to increase from as-worked to recrystallized state.

B. Work Hardening Characteristics of ECAE Processed Niobium

For comparison reasons, results of previous work on Vickers (100gf) work hardening measurements in a cold-rolled bicrystal should be discussed. The individual crystals were labeled grain A and grain B. This research involved cold-rolling a bicrystal billet that was cut from a high-purity coarse-grained electron-beam niobium ingot with grains oriented in the longitudinal direction[27]. The size and shape of the crystals in the bicrystal were similar to those in the billets in this research. The initial orientation of grain A was (221) [434} and was (102) [101] for grain B. The bicrystal was cold-rolled to reductions of 33%, 50% and 70% with hardness measurements taken for each grain after each roll. Their results showed that hardness increases with increasing strain for both grains yet grain B had larger hardness values. Standard deviations increased with increasing strain for both grains with grain B had larger standard deviations. Grain A increased from the as-cast hardness of 51 ± 3 to a maximum hardness at 70% reduction of 92 ± 3. Grain B increased from the as-cast hardness of 53 ± 3 to a maximum hardness at 70% reduction of 100 ± 16. Work hardening also varied from the grain boundary indicating hardness heterogeneity. This was most noticeable with grain B when looking at the standard deviations. They concluded that the variance in hardness reflects the amount of stored energy in the worked material which influenced the recrystallization kinetics.

All Reference Metals billets subjected to ECAE were tested for work hardening characteristics after each extrusion by Rockwell B, Brinell (500 kg for 10 sec) and Vickers (300 gf for 13 sec) hardness methods. Because hardness can be associated with strain and nucleation sites can be associated with strain, hardness homogeneity can be associated with recrystallized grain size homogeneity (HGS_R). It should also be noted that strain hardening homogeneity is not the most accurate method of determining if a cold-worked piece will develop into an annealed homogenized recrystallized microstructure. Results of the hardness measurements were as expected.

Observations of hardness measurements show that similarities exist between all three tests. Hardness increases most dramatically after the first pass which corresponds to a strain of 1.16. The Brinell and Rockwell tests show a dramatic increase in hardness with the first pass, moderate softening after the third pass, maximum hardness after the sixth pass and modest softening after the seventh pass. The Vickers test shows moderate softening after the second pass and increasing hardness thereafter. This fluctuation of the Brinell and Rockwell tests is best explained by heterogeneity of hardness throughout the billet as opposed to instrument error. This heterogeneity can best be explained by the fact that each billet was comprised of several crystals and that tests were performed on various locations. Although the precise location of crystals was not known at the time of testing, it is reasonable to assume that different crystals were tested. The

heterogeneous behavior of hardness is further explained by the anisotropic behavior of this large grained material due to strain gradients during the ECAE process. The Brinell hardness tests show that the as-received material has a hardness of 59 and reaches a maximum of 136 after six passes. The Rockwell b measurements show that the as-received material has a hardness of 10 and reaches a maximum after six passes of 86. Vickers hardness measurements show that the as-received material has a hardness of 67 and reaches a maximum hardness after eight passes to approximately 158. The standard deviations of the Vickers hardness decreased to some extent with strain while the standard deviations of both the Rockwell and Brinell measurements being more erratic. This erratic behavior of the standard deviations indicates heterogeneity of strain throughout the billet due to the same reasons as mentioned before which are inherent anisotropy of crystals. The most important observation is that the standard deviations of the work hardening tests do not decrease with increasing strain. This indicates that strain hardening does not become more homogeneous throughout the billet with increasing strain for large grained niobium. Hardness values of previously mentioned cold-rolled research are considerably less than ECAE processed niobium. The reason for this is that the cold-rolled material was annealed at 800^{o} C and 900^{o} C prior to the 50% and 70% reduction. This pre-annealing will have softened the material.

C. Annealing Hardness Characteristics of ECAE Processed Reference Metals and Wah Chang Niobium

For comparison reasons, results of previous mentioned work on Vickers (100gf) recrystallization hardness measurements of a cold-rolled bicrystal should be discussed[27]. Both grains decreased in hardness with increasing annealing temperature from the 800^{o} C annealed state to the 900^{o} C annealed state after each reduction step. Recrystallization hardness values for grain A and grain B are shown in Figures 117 and 118. The maximum hardness for grain A occurred after 50% reduction annealed at 800^{o} C for 1 hr with a value of 78 ± 3. The maximum hardness for grain B occurred after 70% reduction annealed at 800^{o} C for 1 hr with a value of 85 ± 9. Annealing curves at the 800^{o} C annealed state to the 900^{o} C annealed state for the ECAE processed niobium presented in this thesis is shown in Figure 119.

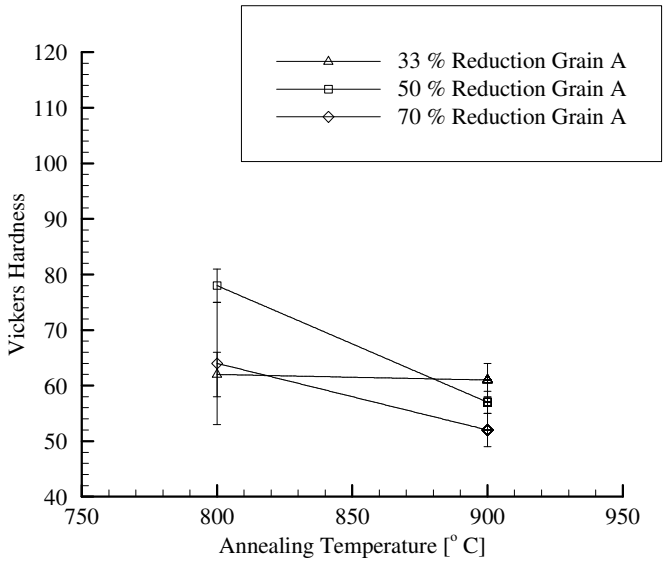

Figure 117. Vickers (100 gf) Annealing Curve for Cold-Rolled Niobium Grain A.

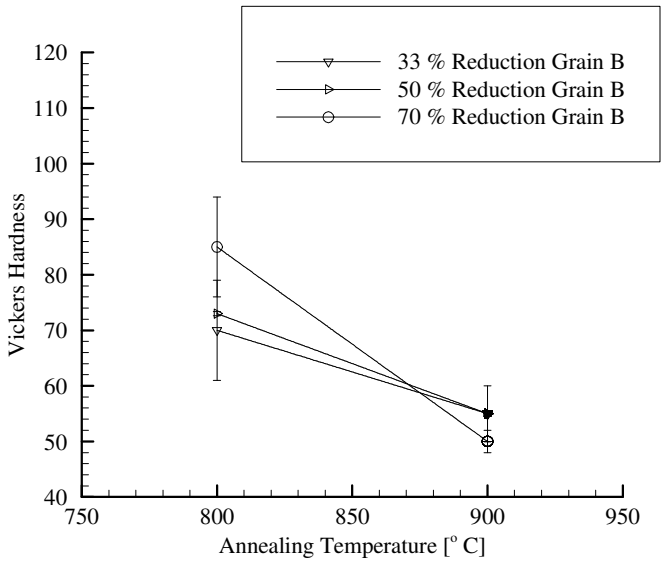

Figure 118. Vickers (100 gf) Annealing Curve for Cold-Rolled Niobium Grain B.

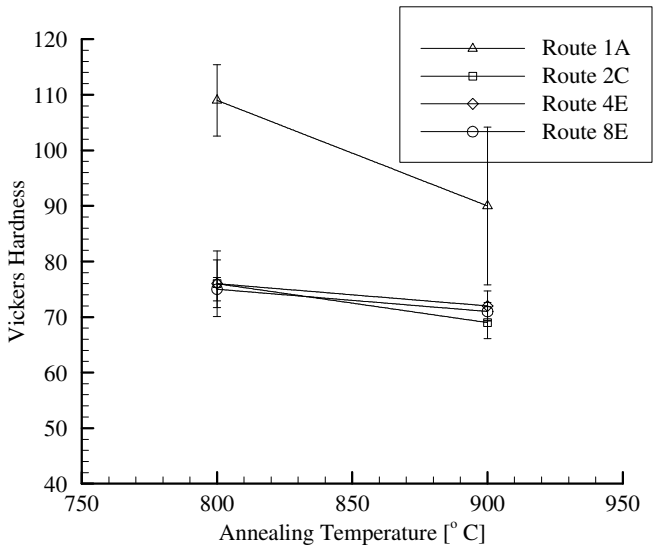

Figure 119. Vickers (300 gf) Annealing Curve for ECAE Processed Niobium.

Recrystallization curves for all billets show similar patterns. All of the ECAE processed billets (Reference Metals and Wah Chang) reached a maximum hardness at 300° C annealing temperature and softened thereafter. The as-received Wah Chang material reached a maximum hardness at 500° C annealing temperature and softened thereafter. The average hardness values at the recovery stage for the Reference Metals billets that underwent routes 1A, 2C, 4E and 8E are 152, 151, 163 and 162 respectively. This increase is due to an increase in dislocation density and dislocation entanglement. The hardness value for the Wah Chang as-received material at the 500° C recovery stage is 144 while the Wah Chang ECAE processed material at the 300° C recovery stage is 157. The recovery stage is associated with changes in the distribution and local density of dislocations. The dense concentration of dislocations in cold worked metals begins to move and interact with each other as the temperature increases. Typically, vacancies are annihilated and dislocations become reorganized to form sub-boundaries. Because the as-recieved Wah Chang material has a lower hardness at the recovery stage, it most likely underwent less strain than the ECAE processed material. Reproducibility of the recrystallization temperatures was consistent for duplicate billets that underwent routes 2C and 4E but was not consistent for the 1A processed billets. The average hardness for all billets annealed at 900° C is 76. Hardness begins to level off at 800° C for routes 2C, 4E and 8E and levels off at 950° C for route 1A. It should be noted that hardness values for duplicate billets were averaged. This inconsistency in the recrystallization temperature for route 1A is most likely due to grain orientation. Billet 3 (route 1A) levels off at 1000° C while billet 18 (1A) levels off at 900° C. Note the large differences in microstructure morphology between samples 3-8 and 18-8. Sample 18-8 has considerably larger grains yet levels off at a

lower temperature. Another anomaly was encountered while dissecting the billets. Some billets would bind the saw blade due to internal strain. In one instance, the blade was broken while removing the billet indicating a large internal stresses. The most important observation is the decrease in the Vickers hardness standard deviation with increasing annealing temperature up to the recrystallization temperature where it remains nearly constant. But it should also be noted that these tests were not performed at various locations on the billet that would represent the whole billet. Therefore, hardness tests for the recrystallized samples do not provide enough information to indicate homogenous strain.

D. Deformation Banding of As-Received and ECAE Processed Niobium

"Deformation banding is a process in which different regions of a deforming crystal gradually rotate to different orientations as deformation proceeds"[[32]. From the stand point of this research, deformation banding is a way of explaining temperature dependent dynamic behavior such as recrystallization. More specifically, it has been shown that a larger amount of highly-misoriented bands produces finer grains after annealing[27]. Furthermore, highly misoriented boundaries are favorable sites for early recrystallization[33]. Associated with deformation banding is the need for extra energy to accommodate the band interfaces and to accommodate the shear deformation at the band ends[32]. To complicate matters, deformation banding has also been linked to grain size[34]. More specifically, coarse-grained metals are more likely to produce deformation bands than are fine-grained metals[35]. This is important because this research extruded large grained billets from the Reference Metals material while the Wah Chang material was partially recrystallized at 900^{o} C annealing. Because the Reference Metals material contained large grains, the general rules for slip in bcc crystals should be recalled. The laws are: slip directions tend to be along the close pack planes, slip planes are the close packed planes and for a given set of slip planes and directions, the crystal operates in that system such that the resolved shear is the largest. In bcc crystals the close packed direction is the <111> direction, but the planes may be {112}, {110} or {122}. The {112} plane is the predominate plane for temperatures below $T_{melt}/4$. In conclusion, the dependence of deformation banding on grain orientation for fcc metals has also been previously published[36].

For comparison reasons, results of previous mentioned work on deformation banding of a cold-rolled bicrystal should be discussed[27]. Their research concluded that cold rolling produced a wide range of misorientation angles between deformation bands and was more orientation dependent than strain dependent. Misorientations ranged from 5^{o} to 55^{o} and varied from within grains and from one grain to another. The variations were explained by crystallographic constraints imposed by grain boundaries and friction effects caused by the rolling process. For comparison reasons, aluminum crystals, which have a fcc structure, also showed misorientations averaging 25^{o} for compression processed material[37].

Deformation banding was evident in all samples with reproducibility improving with increasing strain. Deformation banding morphology contrasted between duplicate routes, within samples and between different routes. In general, the complexity of deformation banding and the density increased with strain. This indicates banding to be a function of strain and grain orientation. The argument for grain orientation dependence is most noticeable in the Reference Metals duplicate billets that underwent route 1A (samples 3-1and 18-1). Billet 3 has more slip systems activated. This is because bcc crystals have numerous slip systems and the activation of slip systems is stress dependent. Also note the significant difference in banding within individual samples. Banding density for sample 18-1 is concentrated at the upper edge and decreases towards the interior of the billet. Because this is most likely one crystal, this heterogeniety is likely due to strain gradients within the billet. It has been shown that misorientations across deformation bands can be caused by friction during the cold rolling process of coarse-grained niobium[27]. The deformation banding for the Wah Chang as-received material is in the longitudinal direction which indicates swaging. After ECAE processing, the Wah Chang material took on similar banding to that of the 4E and 8E processed Reference Metals material. This similarity shows that an increase in strain improves deformation banding reproducibility. It has been shown that increasing strain produces new dislocation structures and new high-angle boundaries in cold-rolled course-grained niobium[27].

E. Grain Morphology of As-Received and ECAE Processed Niobium

For comparison reasons, results of previous mentioned work on recrystallization morphology in a cold-rolled bicrystal should be discussed[27]. The early stages of recrystallization were evident at 800^{o} C annealing and were preferential at banded regions and near grain boundaries. The microstructure was not homogeneous and the researchers attribute this to nucleation. The deformation bands of grain B were highly misoriented resulting in more nucleation sites. This resulted in finer grains after annealing.

Recrystallized microstructures varied among the ECAE processed Reference Metals and Wah Chang billets. Results from the Wah Chang material were as expected while those of the Reference Metals were not. The most significant find was the poor reproducibility of the Reference Metals billets that underwent the same route. This was most evident in the billets that underwent route 1A yet reproducibility improved with increasing strain. The second most significant find was banding in approximately half of the Reference Metals samples. The third significant find was the decrease in average grain size from the 1000^{o} C to the 1100^{o} annealed state in some of the Reference Metals samples.

Reference Metals billets that underwent route 1A (billets 3 and 18) show the most dramatic difference in recrystallized grain morphology. Grain sizes for sample 3-8 (annealed at 1100^{o} C) were significantly smaller than those for sample 18-8 (annealed at 1100^{o} C). This large difference is likely due to the difference in grain orientation. Billet 3 was orientated in such a way as to have more of slip systems activated, resulting in a

finer recrystallized grain structure. This reason is further strengthened by noticing the larger number of deformation bands in sample 3-1 (as-worked). Reproducibility of the recrystallized grain morphology for the Reference Metals material that under went routes 4E and 8E was significantly improved over the 1A processed material as shown in Table 24. The standard deviation of the average grain diameter between sample 2-7 (route 4E/1000^{o} C annealing) and sample 19-7 (route 4E/1000^{o} C annealing) is 2.1. The standard deviation of the average grain diameter between sample 2-8 (route 4E/1100^{o} C annealing) and sample 19-8 (route 4E/1100^{o} C annealing) is 8.2. Although there is a significant difference in standard deviation in the duplicate 4E/1100^{o} C samples, this is still an improvement of reproducibility over the 1A processed material. From this, one can conclude that grain orientation plays a major role in reproducibility of ECAE processed large grained niobium.

Banding of the recrystallized material was most significant in the Reference Metals material. This was evident regardless of route. Because routes 4E and 8E showed the most promising results, the 1000^{o}C and 1100^{o} C annealed states will be discussed. It should also be noted that these two samples were side by side with in the billet. Samples 2-7 (route 4E/1000^{o} C annealing) and 2-8 (route 4E/1100^{o} C annealing) both showed a banding structure. Samples 19-7 (route 4E/1000^{o} C annealing) and 19-8 (route 4E/1100^{o} C annealing) both showed little banding structure. Sample 4-7 (route 8E/1000^{o} C annealing) showed no banding while sample 4-8 (route 8E/1100^{o} C annealing) showed a banding structure. This inconsistency is most likely due to strain gradients during the ECAE processing because of grain orientation effects. The ECAE processed Wah Chang material showed no banding. This further strengthens the hypothesis that banding is more likely to occur in large grained niobium due to grain orientation effects.

Although grain size is expected to increase with an increase in annealing temperature, this was not always the case for the ECAE/annealed Reference Metals samples. There was a slight decrease in the average grain diameters for samples from billets 2 (route 4E) and 4 (route 8E) from the 1000^{o} C annealed state to the 1100^{o} C state as shown in Table 24. There was a significant increase in average grain diameter for samples from billet 19 (route 4E) from the 1000^{o} C annealed state to the 1100^{o} C state as shown in Table 24. Note that banding was not present in samples from billet 19 show no banding while banding was present in samples from billets 2 and 4. The largest decrease in grain size was between samples 4-7 (route 8E/1000^{o} C annealing) and 4-8 (route 8E/1100^{o} C annealing). Note that banding was present in sample 4-8 while there was no banding in sample 4-7. Also note that the banding in sample 4-8 can be divided into the small grained (24.6 ± 1.7 spatial diameter) and large grained regions (43.9 ± 1.6 spatial diameter). Had this experiment by chance chose only the large grained section of sample 4-8, then there would have been an increase in grain diameter from the 1000^{o} C state (35.8 ± 2.1 spatial diameter) to the 1100^{o} C state. Therefore, one cannot conclude the average grain diameter of the whole billet would have decreased from the 1000^{o} C state to the 1100^{o} C state. When considering billets 2 and 19 which both underwent route 4E, the average grain size for billet 2 is lower than that of billet 19. From this, one can conclude that banding results in a lower grain size

and that banding is a result of grain orientation. The ECAE processed Wah Chang material showed the smallest average grain diameter. This is most likely due to the smaller initial grain size for the Wah Chang material.

It has been shown that larger amount of highly misoriented bands produces finer grains after annealing[27][27]. Inhomogeneity in large grained niobium has also been reported in previous work[27][27].

Table 24. Average Grain Diameter and Standard Deviation of Panoramic Calculations.

Billet ID	1000° C Annealing		1100° C Annealing	
	Avg Grain Dia. [μm]	Standard Dev.	Avg Grain Dia. [μm]	Standard Dev.
2 (route 4E)	27.5	10.6	25.9	12.9
19 (route 4E)	31.7	12.9	42.2	19.8
4 (route 8E)	35.8	13.5	29.3	15.1
W2 (route 4E)	17.8	6.3	21	9.5

F. Tensile Tests Results of Reference Metals Material

Tensile tests results of as-cast, as-worked, recovered and recrystallized Reference Metals niobium were as expected. Failure strains, maximum stress, 0.2% yield stress and toughness were examined as functions of strain, route, grain size and hardness.

Failure strains were largest in the as-received material because the grains were larger and had fewer dislocations. In terms of grain size, large grains have more room for dislocations to move before interacting with each other. Furthermore, because grain boundaries serve as barriers to dislocation movement this too gives larger grained materials more ductility. The failure strains of the recrystallized material lie between the as-received and the as-worked/as-recovered material. The failure strains were below that of the as-received material because the grains for the recrystallized material were smaller. As mentioned before, this is because grain boundaries are barriers to dislocation movement. As-worked and recrystallized material had the lowest failure strains because dislocations densities are large with many dislocation-dislocations interactions. These interactions strengthen the materials thereby causing lower fracture strains. There was little correlation between failure strain and strain rate.

Ultimate tensile strengths are usually largest in harder materials as was the case in this research. The as-worked and as-recovered materials had larger ultimate tensile strength than the recrystallized and as-received materials because the as-worked and the as-recovered materials were harder. Hardness can be associated with an increase in dislocations and dislocation/dislocation interactions. This is why the maximum hardness increased with increasing strain.

0.2% yield stress curves were similar to those of the maximum hardness curves. The as-worked and as-recovered materials had larger yield stresses than the recrystallized and as-received materials because the as-worked and the as-recovered materials were harder. This hardness is associated with dislocation morphology as mentioned in the maximum stress section. As in the ultimate tensile strength section, yield stress is an increasing function of increasing strain.

Toughness curves were essentially increasing functions of annealing temperature. The toughness of the as-received material was similar to that of the recrystallized 1A, 4E and 8E routes. The toughness of the recrystallized material that underwent route 2C was slightly larger. There does not appear to be a trend in toughness at the recrystallized state with respect to strain. This is because toughness is a function of stress and strain. Materials with large tensile stresses tend to have smaller strain fractures and materials with small tensile stresses tend to have larger strain fractures. From the energy stand point, recrystallized materials consume more energy than worked materials because the rate of dislocation production is largest in recrystallized materials.

CHAPTER VI

SUMMARY AND CONCLUSIONS

The results of this research have shown that ECAE is an effective method of breaking down coarse-grained niobium. However, the processing routes used are not able to produce a homogeneous recrystallized microstructure for as-cast material. The ECAE processed Wah Chang material resulted in a finer and more homogeneous recrystallized microstructure than the Reference Metals material. The following summaries conclusions have been drawn from the various tests and observations. When referring to the microstructure, the Reference Metals material is called large grained niobium while the Wah Chang material is referred to as partially recrystallized.

A. Summary

1. Large grained (Reference Metals) and partially recrystallized (Wah Chang) pure niobium is very workable under ECAE processing with a 90^{o} angled die. This research shows that large grained niobium is capable of withstanding eight passes and that partially recrystallized niobium is capable of withstanding four passes. Work hardening results and visual observations of the billets post extrusion give reason to believe that pure niobium is capable of withstanding more than eight passes.

2. Hardness increases most dramatically after the first pass and levels off thereafter for large grained niobium. This is evident from all three hardness tests (Rockwell B, Brinell and Vickers). Although ECAE is a valid method for work hardening pure niobium, it is not certain that hardness homogeneity exists throughout the billet. Hardness is probably more homogeneous throughout the partially recrystallized material (Wah Chang) as opposed to the large grained Reference Metals material due to strain gradients inherent with the anisotropy of large crystals when subject to ECAE.

3. Recrystallization temperature is dependent on strain and does not appear dependent on the material source, ie. large grained (Reference Metals) or partially recrystallized Wah Chang niobium. From the Vickers annealing curves, hardness for the large grained material reaches a lower plateau at approximately 800^{o} C for the 2C, 4E and 8E processed material and hardness for the partially recrystallized material levels off at 800^{o} C for the 4E processed material. Hardness for the large grained 1A processed material levels off at 950^{o} C. This gives reason to believe that the recrystallization temperature for pure niobium is reached at 800^{o} C for a strain of 2.32 or more regardless of the initial grain size.

4. Deformation banding is most pronounced for the large grained material and becomes more homogeneous with increasing strain. Heterogeneity of the deformation banding morphology is most evident for 1A and 2C processed large grained material. The homogeneity of deformation banding morphologies of duplicate runs for the large grained material improves with strain. Deformation banding of large grained samples 19-2 (ECAE 4E) and 4-1 (ECAE 8E) were similar but are different for sample 2-1 (ECAE 4E). Deformation banding for the partially recrystallized sample w2-1 (ECAE 4E) is more homogeneous than that of the large grained 4E and 8E ECAE processed large grained samples.

5. Large grained duplicate billets that undergo route 1A show very different recrystallized grain structures. Recrystallized grains for billet 18 were significantly larger than those of billet 3. This indicates that initial grain orientation plays a significant role in deformation microstructures and reproducibility.

6. Large grained duplicate billets that undergo route 2C show an improvement in reproducibility of recrystallized grain morphology over route 1A yet, differences are present. Billet 17 showed banding while billet 24 did not.

7. Large grained duplicate billets that undergo route 4E show further improvement in reproducibility of recrystallized grain morphology and are not much different from material processed via route 8E. Average grain diameters in general increase with increasing annealing temperature and decrease with increasing strain but exceptions exist. The average grain size decreases from the 1000^{o} C state to the 1100^{o} C state for billets 2 (route 4E) and 4 (route 8E). The average grain size for billet 19 (route 4E) shows a significant increase from the 1000^{o} C state to the 1100^{o} C state. Route 4E samples annealed at 1000^{o} C results in an average grain diameter of 27.5 ± 10.6 μm for billet 2 (banding is present) and an average grain diameter of 31.7 ± 12.9 μm for billet 19 (slight banding). Route 8E (banding is not present) annealed at 1000^{o} C resulted in an average grain diameter of 35.8 ± 13.5 μm. Route 4E samples annealed at 1100^{o} C resulted in an average grain diameter of 25.9 ± 12.9 μm for billet 2 (banding was present) and an average grain diameter of 42.2 ± 19.8 μm for billet 19 (slight banding). Route 8E (banding was present) annealed at 1100^{o} C resulted in an average grain diameter of 29.3 ± 15.1 μm. This decrease in grain size with increasing annealing temperature can be attributed to banding. Grain size in samples from billets 2 and 4 decrease slightly from the 1000^{o} C to the 1100^{o} C annealed state and banding was present in both samples. In an attempt to quantitatively analyze banding, the averages for each of the representative samples were averaged along with the standard deviation as shown in Figure 24. Billets 19 (4E) and 2 (8E) show a relatively large change in the spatial standard deviation from the 1000^{o} state to the 1100^{o} state while billet 2 shows a smaller change. Larger changes in spatial standard deviations can be attributed to banding. The spatial standard deviations in the 1000^{o} C annealed state is 4.9 for billet 2 (4E/ Banding was present), 3.3 for billet 19 (4E/Banding was not present) and

is 2.1 for billet 4 (8E/Banding was not present). The spatial standard deviations in the 1100^{o} C annealed state is 7.1 for billet 2 (4E/Banding was present), 11.8 for billet 19 (4E/Slight banding was present) and is 11.0 for billet 4 (8E/Banding was present).

8. The partially recrystallized Wah Chang material that underwent route 4E shows the most promising grain morphology. The average grain diameters are 17.8 ± 6.3 μm and 21.0 ± 9.5 μm for the 1000^{o} state to the 1100^{o} state respectively. Although grain morphology is not homogeneous, there is significant improvement over the large grained material and banding is not present. This improvement is due to the finer partially resrystallized microstructure of the Wah Chang material prior to ECAE processing.

9. Failure strain increases from the as-worked state of 0.21 ± 0.04 to the recrystallized state for ECAE processed large grained niobium of 0.72 ± 0.13 and is grain size dependent.

10. Failure strain for the as-cast large grained niobium (0.9 ± 0.07) is 25 % larger than that of the ECAE processed recrystallized material (0.72 ± 0.13).

11. Failure strain for the as-cast RMC material is not strain rate sensitive over the range of 10^{-5} to 10^{-2}.

12. 0.2 % yield stress decreases from the as-worked state of 386.6 ± 59.9 MPa to the recrystallized state for ECAE processed large grained niobium of 147.5 ± 9.1 MPa.

13. 0.2 % yield stress for the as-cast large grained niobium (104 ± 11.5 MPa) is 30 % smaller than that of the ECAE processed recrystallized material (147.5 ± 9.1 MPa).

14. 0.2 % yield stress for as-cast RMC material is strain rate sensitive over the range of 10^{-5} to 10^{-2} 0.2 % yield stress for large grained niobium increases with strain rate.

15. Ultimate tensile strength decreases from the as-worked state of 444.2 ± 67.4 MPa to the recrystallized state of 231.2 ± 19.3 MPa for ECAE processed large grained niobium.

16. Ultimate tensile strength for the as-cast large grained niobium (154.0 ± 63.0 MPa) is 33 % smaller than that of the ECAE processed recrystallized material (231.2 ± 19.3 MPa).

17. Ultimate tensile strength for as-cast RMC material is strain rate sensitive over the range of 10^{-5} to 10^{-2}. Ultimate tensile strength for large grained niobium increases with strain rate.

18. Toughness increases from the as-worked state of 64.7 ± 10.6 MJoule/m^3 to the recrystallized state 109.8 ± 13.0 MJoule/m^3 for ECAE processed large grained niobium.

19. Toughness for the as-cast large grained niobium (107.6 ± 8.6 MJoule/m^3) is approximately equal to that of the ECAE processed recrystallized material (109.8 ± 13.0 MJoule/m^3).

20. Toughness for as-cast RMC material is not strain rate sensitive over the range of 10^{-5} to 10^{-2}.

21. Sub-grain boundary angles for the ECAE processed large grained material were small for 1 pass and increased for 2C and 4E routes indicating crystal rotation increases with increasing strain. This increase in grain boundary angles is most likely due to the introduction of different intersecting strain planes.

B. Conclusions

From the previously mentioned summaries, the following more general conclusions are drawn.

1. Pure Nb can be easily processed at room temperature to extremely high levels of severe plastic deformation without material fracture (strains well above 10).

2. Large grained pure refractory metals will exhibit significant shear banding during ECAE processing which leads to a banded recrystallized microstructure.

3. Severe deformation (strains > 2) recrystallize at 800^o C to 900^o C.

4. Regions with the smallest recrystallized grains possible in severe plastic deformation processed Nb can be found in as-cast material processed through two passes (strains ≈ 2).

5. It is difficult to eliminate banded recrystallized microstructures in as-cast pure niobium processed without intermediate annealing.

CHAPTER VII

SUGGESTIONS FOR FURTHER STUDIES

Because the results of this research show that ECAE produces a heterogeneous recrystallized microstructure in coarse grained niobium, further topics should be addressed. The first topic to address should be improvement of the ECAE/Annealing process. The large initial grains and strain gradients during the ECAE process are the two of the primary reasons for ECAE to produce a heterogeneous recrystallized grain structure. The second topic should be more grain size measurements. Because this research investigated a small percentage of each billet, the total billet should be analyzed for grain size and homogeneity before and after each extrusion. Furthermore, grain orientations and grain boundaries should be determined before and after each extrusion. This should also be done for tensile testing. Measurements should be taken for numerous grains in the case of recrystallized tensile test specimens in order to get an overall representative structure

Addressing the need to improve the grain morphology of ECAE/Annealing processed niobium, initial grains sizes should be varied as should various methods of decreasing friction during the ECAE process. For this research, a reduction in the initial grain size resulted in a finer grained and more homogeneous microstructure. This was shown in the Wah Chang material that was partially recrystallized prior to ECAE. Fully recrystallized microstructure at various sizes should be tried. Experiments (E) should be functions of various routes (R) and annealing temperatures (T_A). Routes could be functions of passes (P) and rotations (Ω).

$$E = E(R(P, \Omega), T_A)$$

Decreasing friction effects during the ECAE process could involve using various shims, lubricants, decreasing the die angle and by varying the pressing rates.

Optical microscopy should involve more widespread grain size calculations. For example, billets could be annealed at one temperature and analyzed in the three principle axes for grain morphology. Then the same billet could be annealed at a higher temperature and again analyzed for grain morphology. This could determine how banding is affected by the annealing temperature.

Tensile testing should involve optical microscopy and TEM both before and after tensile testing. Optical microscopy prior to testing should involve looking for defects such as grain boundaries and cracks. Grain size calculation should also be employed because mechanical properties are a function of grain size. Other factors can be grain elongation, grain boundary slip and crack propagation. SEM should also be employed since it can give better resolution. TEM can be useful in determining grain orientation before and after tensile testing. Hardness testing at various sections of specimens can also give an idea of strain hardening.

REFERENCES

[1] L. Perron, Niobium, Canadian Minerals Yearbook, www.ncrcan.gc.ca/mms/cmy/com_e.html, 1994.

[2] R.W. Heussner, P.J. Lee, P.D. Jablonski, D.C. Larbalestier, Advances in Cryogenic Engineering, 40 (1994) 755-762.

[3] S. Ochiai, K. Osamura, M. Ryoji, Transactions ISIJ, 28 (1988) 973-977.

[4] Y. Takahashi, N. Koizumi, Y. Nunoya, Y. Takaya, H. Tsuji, IEEE Transactons on Applied Superconductivity, 12 (2002) 1799-1802.

[5] J. G. Lee, C. W. Seo, S. Y. Chang, K. T. Park, D. H. Shin, Journal of the Korean Institute of Metals and Materials, 39 (2) (2001) 158-164.

[6] S.M.L. Sastry, R.N. Mahapatra, Materials Science and Engineering A, 329-331 (2002) 872-877.

[7] M. Kawazoe, T. Shibata, K. Higashi, Materials Science Forum, 233-234 (1997) 207-214.

[8] D. H. Shin, W. J. Kim, W. Y. Choo, Scripta Materialia, 41 (3) (1999) 259-262.

[9] C. S. Pande, Material Physics Mechanics, 2 (2000) 1-9.

[10] T. Bramfeld, J. C. Amato, Pinning Forces in Superconducting Thin Films, http://departments.colgate.edu/physics/students/sresearch99/bramfeld.htm.

[11] R. Kimmich, F. Hornung, A. Rimikis, T. Schneider, P.J. Lee, IEE Transactions on Applied Superconductivity, 11 (1) (2001) 3675-3678.

[12] G. L. Sabbi, IEEE Transactions on Applied Superconductivity, 12 (1) (2002) 236-241.

[13] L. Chengren, D. C. Larbalestier, Cryogenics, 27 (1987) 171-177.

[14] T. Takeuchi, IEEE Transactions on Applied Supercondictivity, 12 (1) (2002) 1088-1093.

[15] L. Thilly, F. Lecouturier, G. Coffe, S. Askenazy, IEEE Transactions on Applied Supercondictivity, 12 (1) (2002) 1181-1184.

[16] F. Hosono, G. Iwaki, K. Kikuchi, S. Ishida, T. Ando, K. Kizu, Y. Miura, A. Sakasai, IEEE Transactions on Applied Supercondictivity, 12 (1) (2002) 1037-1040.

[17] J. W. Ekin, Advanced Cryogenic Engineering, 30 (1984) 823.

[18] K. Watanabe, S. Awaji, K. Takahashi, G. Nishijima, M. Motokawa, Y. Sasaki, Y. Ishikawa, K. Jikihara, J. Sakuraba, IEEE Transactions on Applied Supercondictivity, 12 (1) (2002) 678-681.

[19] M. Schicke, K. F. Schuster, IEEE Transactions on Applied Supercondictivity, 13 (2) (2003)135.

[20] V. Fischer, H. Stormer, D. Gerthsen, M. Stenzel, H. Zillgen, E. Ivers-Tiffee, In Proceedings of the 7th International Conference on Properties and Applications of Dielectric Materials, 1134-1137, Nagoya, Japan, 2003.

[21] S. Mathaudha, Grain Refinement in Bulk Tantalum Using Equal Angular Extrusion, M.S. Thesis, Texas A&M University, College Station, TX. 2001.

[22] K. S. Akhtar, H. Sujian, Continuum Theory of Plasticity, John Wiley & Sons, Inc, New York, 1995.

[23] V.M. Segal, Materials Science and Engineering, A197 (1995) 157.

[24] Y. Iwahashi, J. Wang, Z. Horita, M. Landgin, T.G. Langdon, Scripta Material, 35 (1996) 143.

[25] H. Cui, Computational Modeling of Equal Channel Angular Extrusion, Ph.d. Dissertation, Texas A&M University, College Station, TX, 1996.

[26] The REMBAR Company, Inc. Technical Information, http://www.rembar.com/niobium.htm and http://www/rembar.com/tantalum.htm (2002).

[27] H. R. Z. Sandim, J. F. C. Lins, A. L. Pinto, A. F. Padilha, Mat. Science and Engineering A, 354 (2002) 217-228.

[28] H. Conrad, S. Feuerstein, L. Rice, Materials Science and Engineering, 2 (1967) 157-168.

[29] D. Tabor, The Hardness of Metals, Oxford University Press, London, 1951.

[30] R.E. Smallman, Modern Physical Metallurgy, Butterworths, London, 1985.

[31] T. H. Courtney, Mechanical Behavior of Materials, McGraw Hill, Boston, 2000.

[32] C. S. Lee, B. J. Duggan, R. E. Smallman, Acta Metallergical Materials, 41 (8) (1993) 2265-2270.

[33] D. Kuhlmann-Wilsdorf, Acta Material, 47 (6) (1998) 1697-1712.

[34] B. Bent, N. Hansen, Metallurgical Transactions A, 154 (1984) 287-297.

[35] B.J. Duggan, C.S. Lee, Scripta Metallurgica et Materalia, 27 (1992) 1503-1507.

[36] C. S. Lee, B. J. Duggan, Acta Metallergical Materials, 41 (9) (1993) 2691-2699.

[37] D. A. Hufhs, In Proceedings of the 21st Riso International Symposium on Materials Science, Riso National Laboratory, Roskilde, 2000.

APPENDIX A

Vickers Hardness [300gf for 13 seconds]

Billet 3 ECAE/1A

Annealing Temp. °C	1'st Reading	2'nd Reading	3'rd Reading	4'th Reading	5'th Reading	Average	Std. Dev.
23	141.3	142.4	148.8	150.7	150.2	146.7	4.0
300	157.7	167.7	157.4	162.8	165.7	162.3	4.2
500	147.1	145.9	141.5	143.6	144.0	144.4	1.9
700	125.2	124.3	125.2	128.3	127.5	126.1	1.5
800	115.2	116.8	114.8	114.0	113.7	114.9	1.1
900	93.6	103.5	101.0	113.2	102.3	102.7	6.3
1000	72.2	69.9	72.9	71.3	73.7	72.0	1.3
1100	70.8	68.1	70.4	64.7	67.8	68.4	2.2
1200	72.2	70.0	67.8	64.9	64.6	67.9	2.9

Billet 18 ECAE/1A

Annealing Temp. °C	1'st Reading	2'nd Reading	3'rd Reading	4'th Reading	5'th Reading	Average	Std. Dev.
23	135.0	134.8	134.8	126.0	127.3	131.6	4.0
300	141.1	144.3	141.1	141.5	139.9	141.6	1.5
500	130.3	137.1	126.4	131.7	130.5	131.2	3.4
700	125.0	127.9	121.2	121.4	119.3	123.0	3.1
800	105.1	97.1	102.1	104.8	106.6	103.1	3.4
900	77.6	77.9	79.8	81.8	66.3	76.7	5.4
1000	64.3	65.8	70.2	66.1	69.3	67.1	2.2
1100	66.3	70.2	66.5	65.6	63.5	66.4	2.2
1200	67.2	69.2	71.8	62.1	62.2	66.5	3.8

Billet 17 ECAE/2C

Annealing Temp. °C	1'st Reading	2'nd Reading	3'rd Reading	4'th Reading	5'th Reading	Average	Std. Dev.
23	135.0	138.6	140.4	139.3	132.3	137.1	3.0
300	147.1	154.0	151.0	157.1	145.4	150.9	4.3
500	137.1	143.8	139.3	139.7	139.7	139.9	2.2
700	125.8	134.3	125.4	128.9	132.5	129.4	3.5
800	77.6	78.5	88.2	76.1	84.4	81.0	4.6
900	69.1	67.4	71.4	65.6	65.5	67.8	2.2
1000	69.1	68.8	66.5	67.8	67.8	68.0	0.9
1100	65.9	68.5	71.7	65.6	67.0	67.7	2.2
1200	70.2	70.2	68.7	67.4	66.2	68.5	1.6

Billet 24 ECAE/2C

Annealing Temp. °C	1'st Reading	2'nd Reading	3'rd Reading	4'th Reading	5'th Reading	Average	Std. Dev.
23	138.6	146.8	142.9	140.2	143.6	142.4	2.8
300	152.2	147.6	152.2	150.7	149.5	150.4	1.7
500	143.1	148.5	144.3	145.0	148.5	145.9	2.2
700	132.3	125.4	126.6	130.1	129.7	128.8	2.5
800	72.2	74.2	73.5	69.1	68.9	71.6	2.2
900	70.1	71.3	69.5	72.3	70.9	70.8	1.0
1000	69.4	67.3	66.3	70.5	65.4	67.8	1.9
1100	70.2	63.6	65.1	68.6	65.3	66.6	2.4
1200	68.9	61.6	66.4	66.3	64.9	65.6	2.4

Billet 2 ECAE/4E

Annealing Temp. °C	1'st Reading	2'nd Reading	3'rd Reading	4'th Reading	5'th Reading	Average	Std. Dev.
23	154.0	151.0	148.5	150.2	154.8	151.7	2.4
300	165.9	160.4	174.9	167.4	167.7	167.3	4.6
500	157.1	154.0	151.5	155.0	151.5	153.8	2.1
700	112.7	109.3	114.8	117.2	122.8	115.4	4.5
800	80.1	78.7	85.2	73.9	76.4	78.9	3.8
900	74.3	74.7	72.9	71.3	76.2	73.9	1.7
1000	74.3	73.0	67.1	72.1	70.3	71.4	2.5
1100	68.4	71.8	66.8	70.4	73.0	70.1	2.2
1200	72.4	66.2	66.1	70.7	71.8	69.4	2.7

Billet 19 ECAE/4E

Annealing Temp. °C	1'st Reading	2'nd Reading	3'rd Reading	4'th Reading	5'th Reading	Average	Std. Dev.
23	147.1	147.8	155.3	151.0	149.7	150.2	2.9
300	156.1	157.1	159.0	163.4	160.6	159.2	2.6
500	149.0	151.2	149.5	152.2	150.7	150.5	1.2
700	130.5	126.2	125.0	129.6	123.6	127.0	2.7
800	74.9	71.8	70.2	72.2	73.9	72.6	1.6
900	69.8	67.4	70.2	68.8	71.1	69.5	1.3
1000	69.2	65.9	66.1	70.0	65.6	67.4	1.9
1100	67.3	68.7	71.0	67.0	65.7	68.0	1.8
1200	68.5	77.3	70.1	69.2	68.4	70.7	3.4

Billet 4 ECAE/8E

Annealing Temp. °C	1'st Reading	2'nd Reading	3'rd Reading	4'th Reading	5'th Reading	Average	Std. Dev.
23	152.7	153.0	159.8	160.4	158.7	156.9	3.4
300	157.7	161.4	168.8	159.5	162.0	161.9	3.8
500	150.2	155.0	156.1	156.3	159.3	155.4	3.0
700	105.5	93.5	103.7	116.2	91.6	102.1	8.9
800	72.7	75.9	74.6	79.0	75.0	75.4	2.1
900	68.9	71.8	68.9	71.3	73.0	70.8	1.6
1000	66.9	69.4	68.9	67.0	67.5	67.9	1.0
1100	69.1	66.9	67.8	68.4	70.2	68.5	1.1
1200	67.6	68.0	65.1	65.2	69.1	67.0	1.6

Wah Chang As-Recieved

Annealing Temp. °C	1'st Reading	2'nd Reading	3'rd Reading	4'th Reading	5'th Reading	Average	Std. Dev.
23	145.9	145.7	140.8	139.5	136.5	141.7	3.6
300	137.5	144.5	140.2	141.7	147.1	142.2	3.3
500	149.7	145.9	139.3	143.1	139.5	143.5	3.9
700	118.7	117.7	109.6	112.9	114.3	114.6	3.3
800	92.4	93.3	97.2	98.4	99.6	96.2	2.8
900	65.3	64.7	72.5	69.4	70.4	68.5	3.0
1000	65.2	64.1	67.0	65.7	67.5	65.9	1.2
1100	70.2	67.3	66.2	63.6	65.5	66.6	2.2
1200	68.0	64.5	66.4	65.7	66.9	66.3	1.2

Wah Chang ECAE/4E

Annealing Temp. °C	1'st Reading	2'nd Reading	3'rd Reading	4'th Reading	5'th Reading	Average	Std. Dev.
23	155.0	154.5	153.2	152.7	153.0	153.7	0.9
300	161.7	156.1	157.1	155.8	155.8	157.3	2.3
500	151.2	149.7	151.5	150.5	150.0	150.6	0.7
700	122.5	129.3	125.2	123.9	123.0	124.8	2.4
800	78.3	75.6	74.9	73.1	74.2	75.2	1.7
900	73.0	72.1	73.7	73.4	73.7	73.2	0.6
1000	67.0	67.6	69.0	67.3	67.0	67.6	0.7
1100	65.9	64.9	66.5	64.2	66.2	65.5	0.9
1200	67.8	67.2	63.4	66.7	68.1	66.6	1.7

APPENDIX B

Brinell Hardness [500kg for 10 seconds]

No. of Passes	Billet ID/Route	1'st Reading	2'nd Reading	3'rd Reading	Avg.	Range	Std. Dev.	Avg.
0	9	56.8	55.1	56.8	56.2	1.7	0.98	59.24
		55.1	55.1	56.8	55.7	1.7	0.98	
0	10	56.8	55.1	53.4	55.1	3.4	1.70	
		58.6	56.8	55.1	56.8	3.5	1.75	
0	11	69.1	64.6	60.5	64.7	8.6	4.30	
		64.6	64.6	64.6	64.6	0.0	0.00	
0	12	55.1	53.4	55.1	54.5	1.7	0.98	
		58.6	56.8	58.6	58	1.8	1.04	
0	3/1A	56.8	58.6	62.5	59.3	5.7	2.91	
		58.6	62.5	62.5	61.2	3.9	2.25	
0	18/1A	60.5	56.8	58.6	58.6	3.7	1.85	
		56.8	56.8	60.5	58.0	3.7	2.14	
0	24/2C	62.5	62.5	62.5	62.5	0.0	0.00	
		62.5	62.5	62.5	62.5	0.0	0.00	
0	17/2C	60.5	56.8	58.6	58.6	3.7	1.85	
		60.5	56.8	56.8	58.0	3.7	2.14	
0	2/4E	60.5	62.5	62.5	61.8	2.0	1.15	
		58.6	62.5	58.6	59.9	3.9	2.25	
0	19/4E	60.5	60.5	60.5	60.5	0.0	0.00	
		60.5	60.5	60.5	60.5	0.0	0.00	
0	4/8E	58.6	58.6	56.8	58.0	1.8	1.04	
		56.8	58.6	58.6	58.0	1.8	1.04	

No. of Passes	Billet ID/Route	1'st Reading	2'nd Reading	3'rd Reading	Avg.	Range	Std. Dev.	Avg.
1	3/1A	114.0	124.0	124.0	120.7	10.0	5.77	121.52
1	18/1A	119.0	119.0	119.0	119.0	0.0	0.00	
1	24/2C	124.0	130.0	124.0	126.0	6.0	3.46	
1	17/2C	136.0	136.0	130.0	134.0	6.0	3.46	
1	2/4E	130.0	130.0	109.0	123.0	21.0	12.12	
1	19/4E	109.0	114.0	109.0	110.7	5.0	2.89	
1	4/8E	119.0	119.0	114.0	117.3	5.0	2.89	

No. of Passes	Billet ID/Route	1'st Reading	2'nd Reading	3'rd Reading	Avg.	Range	Std. Dev.	Avg.
2	24/2C	130.0	130.0	130.0	130.0	0.0	0.00	127.0
2	17/2C	130.0	119.0	124.0	124.3	11.0	5.51	
2	2/4E	119.0	130.0	130.0	126.3	11.0	6.35	
2	19/4E	130.0	130.0	124.0	128.0	6.0	3.46	
2	4/8E	130.0	119.0	130.0	126.3	11.0	6.35	

No. of Passes	Billet ID/Route	1'st Reading	2'nd Reading	3'rd Reading	Avg.	Range	Std. Dev.	Avg.
3	2/4E	130.0	119.0	130.0	126.3	11.0	6.35	129.0
3	19/4E	124.0	136.0	143.0	134.3	19.0	9.61	
3	4/8E	119.0	130.0	130.0	126.3	11.0	6.35	

No. of Passes	Billet ID/Route	1'st Reading	2'nd Reading	3'rd Reading	Avg.	Range	Std. Dev.	Avg.
4	2/4E	143.0	136.0	136.0	138.3	7.0	4.04	133.4
4	19/4E	124.0	136.0	136.0	132.0	12.0	6.93	
4	4/8E	130.0	130.0	130.0	130.0	0.0	0.0	

No. of Passes	Billet ID/Route	1'st Reading	2'nd Reading	3'rd Reading	Avg.	Range	Std. Dev.	Avg.
5	4/8E	143.0	125.0	125.0	131.0	18.0	10.39	131.0

No. of Passes	Billet ID/Route	1'st Reading	2'nd Reading	3'rd Reading	Avg.	Range	Std. Dev.	Avg.
6	4/8E	143.0	130.0	136.0	136.3	13.0	6.51	136.3

No. of Passes	Billet ID/Route	1'st Reading	2'nd Reading	3'rd Reading	Avg.	Range	Std. Dev.	Avg.
7	4/8E	141.0	130.0	130.0	133.7	11.0	6.35	133.7

No. of Passes	Billet ID/Route	1'st Reading	2'nd Reading	3'rd Reading	Avg.	Range	Std. Dev.	Avg.
8	4/8E	136.0	119.0	124.0	126.3	17.0	8.74	126.3

APPENDIX C

Rockwell Hardness

No. of Passes	Scale	Billet ID/Route	1'st	2'nd	3'rd	4'th	5'th	Avg.	Range	Std. Dev.	Avg.
0	F	9	64.3	65.0	66.0	60.5	63.8	63.9	5.5	2.08	62.82 10 [B scale] 59.24 [HBR500]
			65.0	63.0	56.5	61.8	61.5	61.6	8.5	3.15	
0		10	62.0	60.5	62.7	60.0	59.9	61.0	2.8	1.26	
			62.0	65.5	60.0	65.0	64.0	63.3	5.5	2.28	
0		11	53.5	60.5	66.0	65.8	64.6	62.1	12.5	5.28	
			61.5	65.5	67.8	63.5	49.4	61.5	18.4	7.18	
0		12	65.5	60.8	63.5	64.0	60.5	62.9	5.0	2.15	
			71.6	70.5	73.0	72.0	73.5	72.1	3.0	1.18	
0		3/1A	57.2	60.1	61.6	54.8	58.6	58.5	6.8	2.62	
			60.0	61.2	60.0	60.1	58.0	59.9	3.2	1.16	
0		18/1A	61.8	65.8	68.0	61.5	60.0	63.4	8.0	3.34	
			63.0	64.2	64.0	65.0	67.5	64.7	4.5	1.70	
0		24/2C	60.0	64.3	68.6	63.5	65.5	64.4	8.6	3.12	
			69.4	66.8	66.8	66.0	64.7	66.7	4.7	1.72	
0		17/2C	65.0	67.5	65.5	69.0	69.0	67.2	4.0	1.89	
			64.3	64.5	66.0	61.8	67.2	64.8	5.4	2.03	
0		2/4E	59.5	58.4	61.4	59.7	62.5	60.3	4.1	1.63	
			63.5	67.0	63.1	63.0	63.0	63.9	4.0	1.73	
0		19/4E	59.7	56.7	59.0	58.5	58.5	58.5	3.0	1.11	
			60.7	60.5	64.5	64.5	62.0	62.4	4.0	1.97	
0		4/8E	46.4	56.5	60.6	57.8	60.0	56.3	14.2	5.75	
			64.8	69.0	63.2	60.0	56.8	62.8	12.2	4.65	

No. of Passes	Scale	Billet ID/Route	1'st	2'nd	3'rd	4'th	5'th	Avg.	Range	Std. Dev.	Avg.
1	B	3/1A	60.8	66.5	71.8	64.8	71.0	67.0	11.0	4.54	67.86 122.00 [HBR500]
1		18/1A	74.8	62.5	66.2	71.5	68.0	68.6	12.3	4.75	
1		24/2C	79.4	68.5	73.2	73.4	69.0	72.7	10.9	4.39	
1		17/2C	73.2	62.8	72.0	69.9	67.5	69.1	10.4	4.13	
1		2/4E	74.2	66.5	68.0	74.4	75.0	71.6	8.5	4.04	
1		19/4E	54.5	60.8	65.2	64.2	58.0	60.5	10.7	4.42	
1		4/8E	61.5	70.2	67.3	62.5	66.0	65.5	8.7	3.56	

No. of Passes	Scale	Billet ID/Route	1'st	2'nd	3'rd	4'th	5'th	Avg.	Range	Std. Dev.	Avg.
2	B	24/2C	83.0	80.3	83.0	82.5	77.0	81.2	6.0	2.58	79.62 129.00 [HBR500]
2		17/2C	80.5	79.8	78.5	81.5	78.8	79.8	3.0	1.23	
2		2/4E	73.5	79.5	78.0	78.5	83.3	78.6	9.8	3.51	
2		19/4E	75.8	79.8	80.5	75.0	83.7	79.0	8.7	3.58	
2		4/8E	80.8	77.0	81.0	77.5	81.8	79.6	4.8	2.20	

No. of Passes	Scale	Billet ID/Route	1'st	2'nd	3'rd	4'th	5'th	Avg.	Range	Std. Dev.	Avg.
3	B	2/4E	79.5	86.0	82.0	84.0	83.0	82.9	6.5	2.41	79.85 130.00 [HBR500]
3		19/4E	79.0	84.5	76.8	87.0	81.0	81.7	10.2	4.11	
3		4/8E	72.5	72.0	78.0	73.5	79.0	75.0	7.0	3.26	

No. of Passes	Scale	Billet ID/Route	1'st	2'nd	3'rd	4'th	5'th	Avg.	Range	Std. Dev.	Avg.
4	B	2/4E	87.5	84.2	88.5	85.5	81.3	85.4	7.2	2.84	84.59 142.00 [HBR500]
4		19/4E	84.2	85.5	87.0	86.5	84.8	85.6	2.8	1.16	
4		4/8E	84.5	81.5	84.0	84.0	79.9	82.8	4.6	1.99	

No. of Passes	Scale	Billet ID/Route	1'st	2'nd	3'rd	4'th	5'th	Avg.	Range	Std. Dev.	Avg.
5	B	4/8E	84.0	82.0	83.5	85.2	83.5	83.6	3.2	1.15	83.64 139.00 [HBR500]

No. of Passes	Scale	Billet ID/Route	1'st	2'nd	3'rd	4'th	5'th	Avg.	Range	Std. Dev.	Avg.
6	B	4/8E	88.2	88.8	84.0	83.2	86.0	86.0	5.6	2.48	86.04 145.00 [HBR500]

No. of Passes	Scale	Billet ID/Route	1'st	2'nd	3'rd	4'th	5'th	Avg.	Range	Std. Dev.	Avg.
7	B	4/8E	80.3	87.0	86.7	86.5	81.0	84.3	6.7	3.36	84.30 140.00 [HBR500]

No. of Passes	Scale	Billet ID/Route	1'st	2'nd	3'rd	4'th	5'th	Avg.	Range	Std. Dev.	Avg.
8	B	4/8E	80.0	85.0	86.2	83.6	84.8	83.9	6.2	2.38	83.92 136.00 [HBR500]

VITA

Name:	Don O. Bryant
Address:	Department of Mechanical Engineering, Texas A&M University, College Station, Texas 77845. Mail stop: 3123.
Email Address:	bryantdon6@aol.com
Education:	B.S., Applied Physics, The University of Texas at San Antonio, 1985 M.S., Mechanical Engineering, Texas A&M University, 2005